

FINAL PROJECT REPORT # 00046726

GRANT: DTRT13-G-UTC45
Project Period: 5/15/2014 – 6/30/18

Economical and Crack-Free High Performance Concrete with Adapted Rheology

Participating Consortium Member:
Missouri University of Science and Technology
Rutgers, The State University of New Jersey
Polytechnic Institute of New York University
University of Oklahoma

Authors:
Kamal H. Khayat
Iman Mehdipour
Hani Nassif
Zeeshan Ghanchi
Chaekuk Na
Kaan Ozbay
Jeffery S. Volz



RE-CAST:
REsearch on Concrete Applications for
Sustainable Transportation
Tier 1 University Transportation Center



DISCLAIMER

The contents of this report reflect the views of the authors, who are responsible for the facts and the accuracy of the information presented herein. This document is disseminated under the sponsorship of the U.S. Department of Transportation's University Transportation Centers Program, in the interest of information exchange. The U.S. Government assumes no liability for the contents or use thereof.

TECHNICAL REPORT DOCUMENTATION PAGE

1. Report No. RECAST UTC # 00046726	2. Government Accession No.	3. Recipient's Catalog No.	
4. Title and Subtitle Economical and Crack-Free High Performance Concrete with Adapted Rheology		5. Report Date March 2019	
		6. Performing Organization Code:	
7. Author(s) Kamal H. Khayat, Iman Mehdipour, Hani Nassif, Zeeshan Ghanchi, Chaekuk Na, Kaan Ozbay, Jeffery S. Volz		8. Performing Organization Report No. Project #00046726	
9. Performing Organization Name and Address RE-CAST – Missouri S&T 500 West 16 th Street Rolla, MO 65409-0710		10. Work Unit No.	
		11. Contract or Grant No. USDOT: DTRT13-G-UTC45	
12. Sponsoring Agency Name and Address Office of the Assistant Secretary for Research and Technology U.S. Department of Transportation 1200 New Jersey Avenue, SE Washington, DC 20590		13. Type of Report and Period Covered: Final Report Period: 5/15/14 – 9/30/19	
		14. Sponsoring Agency Code:	
15. Supplementary Notes The investigation was conducted in cooperation with the U. S. Department of Transportation.			
16. Abstract The main objective of this study is to develop, characterize, and validate the performance of a new class of environmentally friendly, economical, and crack-free high-performance concrete referred to as Eco and crack-free HPC that is proportioned with high content of recycle materials. Two classes of Eco-HPC are designed for: (I) pavement (Eco-Pave-Crete); and (II) bridge infrastructure (Eco-Bridge-Crete). Eco-HPC mixtures were designed to have relatively low binder content up to 350 kg/m ³ and develop high resistance to shrinkage and superior durability. A stepwise mixture design methodology was proposed to: (i) optimize binder system and aggregate skeleton to optimize packing density and flow characteristics; (ii) evaluate synergy between shrinkage mitigating materials, fibers, and moist curing duration to reduce shrinkage and enhance cracking resistance; and (iii) validate structural performance of Eco-HPCs. The optimized concrete mixtures exhibited low autogenous and drying shrinkage given the low paste content and use of various shrinkage mitigating strategies. Such strategies included the use of CaO-based expansive agent (EX), saturated lightweight sand (LWS), as well as synthetic or recycled steel fibers. Proper substitution of cement by supplementary cementitious materials (SCMs) resulted in greater packing density of solid particles, lower water/superplasticizer demand, and improved rheological and hardened properties of cement-based materials. The synergistic effect between EX with LWS resulted in lower autogenous and drying shrinkage. For a given fiber content, the use of steel fibers recovered from waste tires had twice the flexural toughness of similar mixture with synthetic fibers. The optimized Eco-HPC mixtures had lower drying shrinkage of 300 μ strain after 250 days. The risk of restrained shrinkage cracking was found to be low for the optimized concrete mixtures (no cracking even after 55 days of testing). The results of structural performance of large-scale reinforced concrete beams indicated that the optimized Eco-Bridge-Crete containing ternary combination of 35% fly ash and 20% slag replacements and recycled steel fibers developed significantly higher flexural toughness compared to the MoDOT reference mixture used for bridge infrastructure applications. Furthermore, this study presents a comprehensive probabilistic Life Cycle Cost Analysis (LCCA) methodology to quantify the life cycle costs of new material and technologies that link laboratory-measured parameters to actual field performance. Two approaches are proposed: 1) Application of a hypothesized improvement rate to the deterioration functions of existing and well tested conventional materials to represent the expected improved performance of new materials; 2) Utilize the correlation between laboratory tests and field performance of known materials to predict the expected performance of a new material based only on the data from its laboratory tests. Both methods are treated probabilistically to determine how the perceived stochasticity affect the sensitivity or prediction reliability of the total life cycle cost of each alternative due to the lack of real-world performance data especially in the case of novel materials/construction technologies.			
17. Key Words Crack-free; Early-age cracking; Eco-Crete; Packing density; Shrinkage mitigating strategies, Supplementary cementitious materials; Structural performance; Life cycle assessment.		18. Distribution Statement No restrictions. This document is available to the public.	
19. Security Classification (of this report) Unclassified	20. Security Classification (of this page) Unclassified	21. No of Pages 160	

Economical and Crack-Free High Performance Concrete with Adapted Rheology

PREPARED FOR THE
RE-CAST UNIVERSITY TRANSPORTATION CENTER

IN COOPERATION WITH THE

Missouri University of Science and Technology
Rutgers, The State University of New Jersey
New York University Polytechnic
University of Oklahoma

Prepared By:

Kamal H. Khayat¹, Iman Mehdipour², Hani Nassif³, Zeeshan Ghanchi⁴, Chaekuk Na⁵,
Kaan Ozbay⁶, Jeffery S. Volz⁷

¹ Professor of Department of Civil, Architectural and Environmental Engineering, and Director of Center for Infrastructure Engineering Studies, Missouri University of Science and Technology, Rolla, MO, USA (PI)

² Ph.D., Center for Infrastructure Engineering Studies, Department of Civil, Architectural and Environmental Engineering, Missouri University of Science and Technology, Rolla, MO, USA

³ Professor and Associate Director, Dept. of Civil & Environ. Engineering, Rutgers, The State University of New Jersey, Piscataway, NJ, USA

⁴ Former Graduate Research Assistant, Dept. of Civil & Environ. Engineering, Rutgers, The State University of New Jersey, Piscataway, NJ, USA

⁵ Research Associate, Dept. of Civil & Environ. Engineering, Rutgers, The State University of New Jersey, Piscataway, NJ, USA

⁶ Professor of Civil and Urban Engineering, Center for Urban Science and Progress, New York University Polytechnic Institute, Brooklyn, NY

⁷ Associate Professor of Civil Engineering, the University of Oklahoma, Norman, OK

RE-CAST
Submitted
March 2019

EXECUTIVE SUMMARY

The main objective of this study is to develop, characterize, and validate the performance of a new class of environmentally friendly, economical, and crack-free high-performance concrete referred to as Eco- and crack-free HPC that is proportioned with a high content of recycled materials. Two classes of Eco-HPC are designed for: (I) pavement (Eco-Pave-Crete); and (II) bridge infrastructure (Eco-Bridge-Crete). Eco-HPC mixtures were designed to have relatively low binder content up to 350 kg/m³ and develop high resistance to shrinkage and superior durability. A stepwise mixture design methodology was proposed to: (i) optimize binder system and aggregate skeleton to optimize packing density and flow characteristics; (ii) evaluate synergy between shrinkage mitigating materials, fibers, and moist curing duration to reduce shrinkage and enhance cracking resistance; and (iii) validate structural performance of Eco-HPCs. The composition-reaction-property correlations were developed to link the hydration kinetics of various binder systems to material performance in fresh state (rheological properties) and hardened state (strength gain and shrinkage cracking tendency). Results indicate that it is possible to design Eco-HPC with drying shrinkage lower than 300 μ strain after 250 days and no restrained shrinkage cracking even after 55 days. Reinforced concrete beams made with Eco-Bridge-Crete containing up to 60% replacement of cement with supplementary cementitious materials and recycled steel fibers developed significantly higher flexural toughness compared to the reference concrete used for bridge applications. Furthermore, this study presents a comprehensive probabilistic Life Cycle Cost Analysis (LCCA) methodology to quantify the life cycle costs of new material and technologies that link laboratory-measured parameters to actual field performance. Two approaches are proposed: 1) Application of a hypothesized improvement rate to the deterioration functions of existing and well tested conventional materials to represent the expected improved performance of new materials; 2) Utilize the correlation between laboratory tests and field performance of known materials to predict the expected performance of a new material based only on the data from its laboratory tests. Both methods are treated probabilistically to determine how the perceived stochasticity affect the sensitivity or prediction reliability of the total life cycle cost of each alternative due to the lack of real-world performance data, especially in the case of novel materials/construction technologies.

Keywords:

Bridge; Crack-free concrete; Early-age cracking; Eco-Crete; Expansive admixture; Packing density; Pavement; Shrinkage, Supplementary cementitious materials; Structural performance; Life cycle cost assessment.

ACKNOWLEDGEMENT

The authors would like to acknowledge the many individuals and organizations that made this research project possible. First and foremost, the authors would like to acknowledge the financial support of Missouri Department of Transportation (MoDOT) as well as the RE-CAST (REsearch on Concrete Applications for Sustainable Transportation) Tier-1 University Transportation Center (UTC) at Missouri University of Science and Technology (Missouri S&T).

The authors would also like to thank the companies that provided materials required for the successful completion of this project, including LafargeHolcim, BASF, Euclid Chemical, Buildex, and Capital Sand Company, as well as Granuband Macon.

The cooperation and support from Abigayle Sherman and Gayle Spitzmiller of the Center for Infrastructure Engineering Studies (CIES) are greatly acknowledged, in particular the assistance of Dr. Soo-Duck Hwang, Lead Scientist, and Jason Cox, Senior Research Specialist is highly appreciated. Valuable technical support provided by technical staff of the Department of Civil, architectural, and Environmental Engineering at Missouri S&T is deeply appreciated, in particular Brian Smith, John Bullock, and Gary Abbott.

CONTENTS

1. INTRODUCTION	1
1.1. Problem statement.....	1
1.2. Research objectives.....	2
1.3. Research methodology.....	3
1.3.1. Task 1 - Laboratory investigation.....	3
1.3.2. Task 2 - Deformation measurement and structural performance evaluation.....	3
1.3.3. Task 3 - Life cycle assessment.....	4
2. EXPERIMENTAL PROGRAM	5
2.1. Materials.....	5
2.2. Testing program.....	13
2.3. Mixing procedure.....	19
2.4. Test methods.....	19
2.4.1. Test methods for mortar mixtures.....	19
2.4.2. Test methods for concrete mixtures.....	20
3. TEST RESULTS AND DISCUSSION	28
3.1. Optimization of binder composition.....	28
3.1.1. Time dependent rheological properties.....	28
3.1.2. Heat of hydration.....	30
3.1.3. Hardened characteristics.....	30
3.1.4. Selection of optimum binder composition.....	32
3.2. Optimization of aggregate characteristics.....	34
3.2.1. Aggregate optimization using packing density approach.....	36
3.2.2. Optimization of aggregate proportioning using SMD method.....	39
3.2.3. Comparison of shrinkage mitigating strategies.....	41
3.2.4. Autogenous shrinkage.....	43
3.2.5. Drying shrinkage.....	45
3.3. Development of Eco and crack-free HPC.....	47
3.3.1. Mechanical properties.....	50
3.3.2. Shrinkage.....	51
3.3.3. Durability.....	53
3.4. Final mixture design.....	55
3.4.1. Fresh properties.....	56
3.4.2. Mechanical properties.....	57
3.5. Concrete performance evaluation.....	58
3.5.1. Fresh properties.....	58
3.5.2. Air content.....	60
3.5.3. Mechanical properties.....	60
3.5.4. Shrinkage properties.....	61
4. VALIDATION OF ECO-HPC PERFORMANCE IN LARGE-SCALE ELEMENTS	68
4.1. Shrinkage of concrete slab section.....	68
4.1.1. Shrinkage and relative humidity measurement.....	71
4.1.2. Temperature measurement.....	72

4.1.3. Pavement test sections	72
4.2. Structural performance of reinforced concrete beams	74
4.2.1. Flexural load-deflection response.....	75
4.2.2. Beam shear test specimens	76
4.2.3. Beam bond test specimens.....	79
5. LIFE CYCLE COST ANALYSIS.....	81
5.1. Introduction.....	81
5.2. Literature review	82
5.3. LCCA general cost function and implementation procedure	84
5.4. Deterioration models.....	85
5.5. Proposed methodology.....	86
5.5.1. Approach I – Improvement rate	87
5.5.2. Approach II – Correlation method.....	90
5.6. LCCA example: economical and crack-free high performance concrete (Eco-HPC)...	91
5.6.1. User & societal costs	91
5.6.2. Energy consumption and global warming potentials (GWPs)	91
5.6.3. Agency costs.....	92
6. SUMMARY AND CONCLUSIONS.....	98
6.1. Optimization of binder composition	98
6.2. Optimization of aggregate skeleton	99
6.3. Comparison of shrinkage mitigating strategies.....	100
6.4. Development of Eco and crack-free HPC.....	100
6.5. Performance validation of Eco and crack-free HPC.....	101
REFERENCES.....	103
APPENDIX A MATERIAL PROPERTIES	108
APPENDIX B TEST RESULTS AND DISSCUSSION	123
APPENDIX C VALIDATION OF ECO-HPC PERFORMANCE IN LARGE-SCALE ELEMENTS	131

LIST OF FIGURES

Figure 2.1. PSD of cementitious materials	5
Figure 2.2. Variation in geometries of recovered steel fibers.....	7
Figure 2.3. Bulk electrical conductivity (left) and surface resistivity (right)	23
Figure 3.1. Effect of SCM substitutions on rheological properties of mortars.....	29
Figure 3.2. Effect of SCM substitutions on hydration heat evolution	30
Figure 3.3. Effect of SCM substitutions on compressive strength development of mortars	31
Figure 3.4. Drying shrinkage of mortars made with different SCM substitutions	32
Figure 3.5. Overall performance of mortars made with 320 kg/m ³ (20 lb/ft ³) binder content	33
Figure 3.6. Overall performance of mortars made with 350 kg/m ³ (22 lb/ft ³) binder content	34
Figure 3.7. Variations in packing density of mono aggregates using ICT	36
Figure 3.8. Variations in packing density for binary aggregate blends	37
Figure 3.9. Ternary Packing diagram of various aggregate blends measured by ICT.....	39
Figure 3.10. PSD of selected aggregate blend.....	41
Figure 3.11. Autogenous shrinkage of mortars made with various binder compositions and shrinkage mitigating materials.....	44
Figure 3.12. Effect of using LWS on RH of mortars over time.....	45
Figure 3.13. Drying shrinkage of mortars made with various binder compositions and shrinkage mitigating materials as a function of IMCP	46
Figure 3.14. Mechanical properties of selected HPC mixtures	51
Figure 3.15. Shrinkage of selected HPC mixtures.....	52
Figure 3.16. Durability performance of selected HPC mixtures	54
Figure 3.17. Durability performance of selected HPC mixtures	55
Figure 3.18. Free shrinkage strain.....	62
Figure 3.19. Concrete strain (VWSG) of PPE 0.00 mixture ring 1	63
Figure 3.20. Steel strain (FSG) of PPE 0.00 mixture.....	63
Figure 4.1. Typical beam shear test specimen load-deflection response.....	78
Figure 4.2. Typical beam shear test specimen failures	78
Figure 5.1. General LCCA inputs and outputs (Ozbay and Gao, 2016).....	84
Figure 5.2. Life-cycle of two alternatives and corresponding expenditure stream diagram (Jawad 2003)	85
Figure 5.3. Deterioration model and life cycle cost expenditures	86
Figure 5.4. Two proposed approaches for estimating predicted deterioration functions of a new material or a novel construction technology.....	88
Figure 5.5. Using laboratory results to update a deterministic deterioration function	89
Figure 5.6. Illustration of the proposed correlation method to quantify time-dependent deterioration behavior of new and known materials.....	90
Figure 5.7. Variation in embodied energy and GWP with different mixtures (Mehdipour 2016)	96
Figure 5.8. Sensitivity analysis example (Estimated weight of user cost).....	96
Figure 5.9. Bridge LCCA example – probabilistic approach	97

LIST OF TABLES

Table 1.1. Target properties of Eco-Pave-Crete and Eco-Bridge-Crete	2
Table 2.1. Characteristics of chemical admixtures	6
Table 2.2. Selected aggregates from different quarries for preliminary evaluation	8
Table 2.3. Testing parameters selected for ICT	9
Table 2.4. Chemical and physical properties of cementitious materials.....	10
Table 2.5. Fine aggregate gradation and percent passing limits	10
Table 2.6. No. 57 coarse aggregate gradation and percent passing limits.....	11
Table 2.7. No. 8 coarse aggregate gradation and percent passing limits	11
Table 2.8. Aggregate properties.....	11
Table 2.9. Synthetic fiber properties and recommended contents	12
Table 2.10. Materials and suppliers.....	13
Table 2.11. Coarse and fine aggregate properties.....	13
Table 2.12. Polypropylene fiber properties.....	13
Table 2.13. Testing program for binder optimization.....	14
Table 2.14. Baseline ODOT mixture design requirements.....	16
Table 2.15. Mixture proportions	18
Table 2.16. Experimental matrix for concrete phase	21
Table 3.1. Mixture proportions of investigated CEM mixtures (volume-basis).....	28
Table 3.2. Selected test properties to optimize binder composition for Eco-Pave-Crete	32
Table 3.3. Selected test properties to optimize binder composition for Eco-Bridge-Crete	32
Table 3.4. Selected optimal binder compositions	34
Table 3.5. Packing densities of investigated aggregates.....	35
Table 3.6. Packing density of binary aggregate blends	37
Table 3.7. Packing density of ternary aggregate blends	38
Table 3.8. Optimum aggregate proportions using SMD method.....	41
Table 3.9. Selected optimum binders targeted for Eco-Pave-Crete and Eco-Bridge-Crete.....	42
Table 3.10. Mixture design parameters investigated for shrinkage mitigating strategies	43
Table 3.11. Investigated mixture design parameters in Subtask 2-4	48
Table 3.12. Mixture proportions of Eco and crack-free HPC mixtures.....	49
Table 3.13. Cracking potential classification of HPC mixtures.....	52
Table 3.14. Deicing salt scaling rating of HPC mixtures	54
Table 3.15. Final mixture designs.....	56
Table 3.16. Fresh concrete properties	57
Table 3.17. Mechanical properties.....	57
Table 3.18. Normalized mechanical properties	58
Table 3.19. Initial and adjusted slump values and J-Ring test results	59
Table 3.20. T20 and VSI test results.....	59
Table 3.21. L-Box test results	60
Table 3.22. Air content test results	60
Table 3.23. Mechanical properties (% difference compared to the control mix, PPE 0.00)	61
Table 3.24. First cracking age for restrained shrinkage rings.....	66
Table 3.25. Max crack widths and cracking area for restrained shrinkage rings.....	67

Table 4.1. Selected concrete mixtures for slab sections 69
Table 4.2. Summary of instrumentation plan used for each slab 70
Table 4.3. Codifications of sensors used for slab instrumentation 70
Table 5.1. Summary of seven state DOTs LCCA practices 82
Table 5.2. Literature review on new construction materials and technologies..... 83
Table 5.3. LCCA example work flow – inputs 94
Table 5.4. LCCA example work flow – deterministic outputs 95

1. INTRODUCTION

1.1. Problem statement

As global demand for the use of concrete in construction applications increases progressively, the concrete industry faces the crucial challenge of finding strategies to reduce the CO₂ emissions and embodied energy associated with ordinary portland cement (OPC) production. Portland cement production results in approximately 0.87 ton of carbon dioxide for every ton of cement produced; this accounts for 5%-7% of global CO₂ emissions (Tuner and Collins). The growing demands for new infrastructure, and the need for modernizing existing infrastructure and the associated cement-use has brought into question the viability and sustainability of cement-based materials for the coming decades. This is significant as legislation and climate policy are expected to substantially impact the construction sector as national governments try to meet climate change agreements. In the United States (U.S.), over 150 million tons of cement per year are used (Imbabi et al. 2012). It is estimated that 1.53 m³ (2 yd³) of concrete per person is placed each year to support the U.S. infrastructure. Most of our concrete infrastructure is older than 20 years, and the national grand challenge of maintenance and repair is well-known. Approximately 68.5% of all the U.S. bridges are older than 25 years old and 30.8% are over 50 years old (ASCE, 2017). In the area of bridges alone, according to the U.S. National Bridge Inventory (2013), there are over 605,000 bridges of which 11.7% are functionally obsolete and 14.7% are structurally deficient.

Concrete bridge decks usually require the use of HPC due to its low permeability, high abrasion resistance, superior durability, thus extending service life. To meet such requirements, HPC implemented for bridge decks is usually characterized with relatively low water-to-cementitious material ratio (w/cm) [typically less than 0.40] and high binder content. Such features in the mixture design of HPC can inherently elevate the risk of early-age and later age (drying) shrinkage cracking. Autogenous shrinkage at early age is one of the major causes of cracking of HPC. Cracking will occur if the strain from autogenous shrinkage exceeds the tensile strength of the concrete, especially at early-age when concrete has a low tensile strength. The shrinkage cracking in bridge decks increases the risk of freeze-thaw damage, corrosion of reinforcing steel, and ingress of various deleterious substances. This can lead to premature deterioration and potential structural deficiencies of concrete infrastructure, thus shortening design life of the structure. In 2003, a nationwide state DOTs survey conducted by the Michigan DOT on early-age bridge deck cracking issues indicated that 78% of the 31 responding states identified transverse cracking due to drying shrinkage. Cracking in HPC can result in a significant decrease in durability and service life of the concrete structures.

Therefore, the aim of this project is to develop and validate the behavior of a new class of environmentally friendly and cost-effective high-performance concrete (HPC), which is referred to herein as Eco-HPC. The proposed project will develop two classes of Eco-HPC for the following applications: HPC for pavement construction (Eco-Pave-Crete) and HPC for bridge desk and transportation infrastructure construction (Eco-Bridge-Crete). Eco-Bridge-Crete can be used in cast-in-place girders, cast-in-place piers and piles, and other bridge elements. Both Eco-HPC types will also be designed to ensure high durability. The concrete should develop high

resistance to cracking to limit the crack width of hairline cracks to 0.1 mm (0.004.in). The rheological properties of these advanced materials were designed to facilitate construction operations and reduce labor and cost. Both Eco-HPC types will also be designed to ensure high durability. Table 1.1 summarizes some of the performance-based specifications that are required for these concrete types.

Table 1.1. Target properties of Eco-Pave-Crete and Eco-Bridge-Crete

Eco-Pave-Crete (with different workability levels)	
Binder content	320 kg/m ³ (20 lb/ft ³)
Slump (without fibers)	50 ± 25 mm (26 ± 1 in.)
Slump (with fibers)	100 ± 25 mm (4 ± 1 in.)
Compressive strength at 56 days	≥ 35 MPa (5076 psi)
Drying shrinkage after 120 days (7-d moist curing)	≤ 300 μstrain
Restrained shrinkage cracking potential	Low (time-to-cracking > 28days according to ASTM C1581)
Durability (frost and abrasion resistance)	High (durability factor higher than 70% after 300 freeze-thaw cycles according to ASTM C666, Proc. A)
Eco-Bridge-Crete (with different workability levels)	
Binder content	350 kg/m ³ (22 lb/ft ³)
Slump (without fibers)	100 ± 25 mm (3.9 ± 1 in.)
Slump (with fibers)	200 ± 25 mm (7.9 ± 1 in.)
Compressive strength at 56 days	40 to 50 MPa (5801.5 to 7251 psi)
Drying shrinkage after 120 days (7-d moist curing)	≤ 300 μstrain
Restrained shrinkage cracking potential	Low (time-to-cracking > 28days according to ASTM C1581)
Durability (frost, corrosion, and abrasion resistance)	High (durability factor higher than 70% after 300 freeze-thaw cycles according to ASTM C666, Proc. A)

1.2. Research objectives

The project will establish new mixture design methodology based on the maximum packing density with the aim of reducing cement content and high resistance to shrinkage cracking to enable the development of advanced materials for sustainable pavement and bridge infrastructure construction. It is expected that the results obtained in this work will provide a basis for the development and implementation of:

- New mixture design methodology and guidelines for using Eco- and crack-free HPC for various types of transportation infrastructure and pavement applications.
- Performance-based design with substantial information regarding material characteristics and key engineering properties, structural behavior, and durability of concrete targeted for pavement and infrastructure applications.

The specific objectives of this project are described as follows:

- Optimization of binder composition (in binary and ternary systems) to reduce carbon foot print and cost, as well as shrinkage of concrete by replacing cement with a high volume of supplementary cementitious materials (SCMs).
- Optimization of aggregate skeleton and proportioning based on packing density approach to reduce paste volume.
- Comparing the effectiveness of different shrinkage mitigating materials, including shrinkage reducing admixture (SRA), Type G and Type K expansive agents (EXs), lightweight sand (LWS) for internal curing, and synthetic and recycled steel fibers to improve resistance to cracking of concrete.
- Developing new classes of cost-effective and crack-free environmentally friendly concrete materials with low binder content, high cracking resistance, and various slump consistencies targeted for pavement and transportation infrastructure applications. Furthermore, focus was given to analyze and compare the restrained shrinkage properties of fiber-reinforced self-consolidating concrete (FR-SCC) with polypropylene (PPE) fibers. Enormous efforts have been made to control the volume changes in the concrete matrix by optimizing the mixture design or adding various types of fibers, but few studies address the effect of FR-SCC on the restrained shrinkage performance. Therefore, it is important to understand and analyze the shrinkage behavior of FR-SCC under restrained condition to promote the FR-SCC mixtures for field implementation.
- As a part of the RE-CAST research, an attempt was also made to develop a systematic workflow and guidelines for comparing the life cycle cost of conventional and new construction materials or technologies to assist decision-makers in finding optimum strategies with the ultimate goal of maintaining components of our transportation infrastructure such as pavements and bridges, in safe and efficient condition over time.

1.3. Research methodology

The research project includes three tasks as presented below:

- (1) Laboratory investigation
- (2) Deformation measurement and structural evaluation
- (3) Life cycle assessment

Further details of the work tasks are described below.

1.3.1. Task 1 - Laboratory investigation

A comprehensive investigation was undertaken to evaluate the influence of mixture proportioning and material characteristics on various properties, including workability, rheology, mechanical properties, shrinkage, and durability.

1.3.2. Task 2 - Deformation measurement and structural performance evaluation

Large-scale specimens, including slab and reinforced beam elements were constructed to evaluate the shrinkage deformation and flexural performance of Eco-Pave-Crete and Eco-Bridge-Crete. Concrete mixtures were made in local concrete batching plants to confirm the ability of the proposed concrete to apply in the field.

1.3.3. Task 3 - Life cycle assessment

The proposed methods aim to overcome the challenge of limited data and provide a feasible approach to fast-track the acceptance of the new construction materials or technologies. The main focus of the study is the probabilistic treatment of the inherent uncertainties, quantification of direct and indirect benefits from new construction materials or technologies, including out-of-pocket costs and other externalities affecting environmental sustainability, and finally the development of a web-based tool which operationalizes the proposed methods. Two approaches are proposed: 1) Application of a hypothesized improvement rate to the deterioration functions of existing and well tested conventional materials to represent the expected improved performance of new materials; 2) Utilize the correlation between laboratory tests and field performance of known materials to predict the expected performance of a new material based only on the data from its laboratory tests. Both methods are treated probabilistically to determine how the perceived stochasticity affect the sensitivity or prediction reliability of the total life cycle cost of each alternative due to the lack of real-world performance data especially in the case of novel materials/construction technologies.

2. EXPERIMENTAL PROGRAM

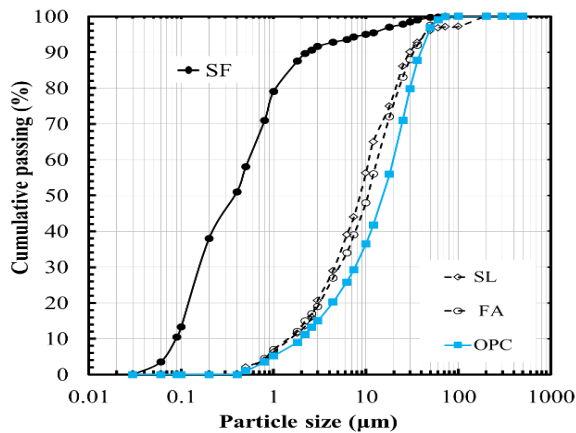
2.1. Materials

This chapter describes constituent materials, testing program, mixing procedure, and method employed for this research program. The investigation that was conducted at Missouri University of Science and Technology, University of Oklahoma, and Rutgers, The State University of New Jersey, are presented in the following sections.

Missouri University of Science and Technology

Cementitious materials

Commercially available Type I/II ordinary portland cement (OPC) was used in this study. Class C fly ash (FA), slag cement (SL), and silica fume (SF) were employed in the binary and ternary cementitious systems. The particle size distribution (PSD) of cementitious materials is summarized in Figure 2.1. The scanning electron microscopy (SEM) images of the investigated cementitious materials are presented in Figure A.1 in Appendix A. Two types of commercially available expansive agents (EX), including Type G EX and Type K EX, and MgO-based EX were used. Type G EX is CaO-based system in which the formation of calcium hydroxide ($\text{Ca}(\text{OH})_2$) crystals causes expansion. The Type K EX contains Portland cement and calcium sulfoaluminate (CSA-based system) cement, in which the expansion is achieved through formation of ettringite crystals. The physical and chemical characteristics of the cementitious materials used in this investigation are presented in in Table A.1 in Appendix A.



agent (AEA). A commercially available crack-reducing admixture (CRA) was also incorporated to reduce shrinkage. The CRA is a liquid chemical admixture based on a specialty alcohol alkoxyate, which is formulated to reduce drying shrinkage and minimize the potential for early-age shrinkage cracking. Similar to conventional SRAs, the CRA reduces the surface tension of water, and it provides similar reduction in drying shrinkage at equal dosages. However, typical results for restrained shrinkage testing of untreated concrete, conventional SRA-treated concrete, and concrete treated with the CRA show that the CRA changes the mode of failure from a sudden release of all the compressive strain to a gradual reduction in strain in the inner steel ring, thereby providing a greater increase in time-to-cracking (Nmai et al., 2014). This phenomenon may be attributed to the relaxation of tensile stress within the CRA-treated concrete specimens (Nmai et al., 2014). The AEA dosage was adjusted to secure fresh air volume of $5\% \pm 2\%$. The HRWR dosages varied to obtain various slump consistencies targeted for pavement (50-100 mm) [1.97 – 3.94 in.] and bridge deck (100-200 mm) [3.94 – 7.87 in.] applications. Table 2.1 presents the characteristics of the chemical admixtures in use.

Table 2.1. Characteristics of chemical admixtures

	Solid content (%)	Specific gravity
HRWRA	23	1.05
VEA	1.5	1
AEA	12.5	1.01
CRA	-	0.98

Fibers

Two types of fibers, including synthetic polypropylene fibers and steel fibers recycled from waste tires were used, as shown in Figure A.2 in Appendix A. The synthetic fiber (structural fiber) is multi-filament with a length and diameter of 50 mm (2 in.) and 0.67 mm (0.027 in.), respectively. It has a specific gravity of 0.92 and tensile strength of 625 MPa (90 ksi). Recycled steel fibers are generally recovered by a shredding process of tires, followed by an electromagnetic procedure aiming at separating steel fibers from the rubber. The fibers obtained are typically characterized by an irregular shape (wavy shape) and variable lengths and thicknesses, as shown in Figure A.2 in Appendix A. The geometry of recovered steel fibers was characterized using statistical distribution of around 100 steel fibers that were randomly selected. The statistical distributions of variation in lengths and thicknesses of recycled steel fibers are presented in Figure 2.2. The fiber thickness and length varied between 0.2 - 1.6 mm (0.008 - 0.063 in.) and 5 - 55 mm (0.2 - 2.15 in.), respectively. Based on the results, the majority of steel fibers had lengths varying between 10 - 30 mm (0.4 - 1.18 in.) and thicknesses of 0.2 - 0.4 mm (0.008 - 0.16 in.). Recently, in the context of a growing interest towards innovative materials recycling and sustainable buildings, some studies proposed the use of steel fibers recovered from waste tires, in concrete. However, more research is required to assess the performance of such fibers for use in pavement and structural applications. In this research, the reinforcing efficiency of such fibers was compared with that of the synthetic structural fibers in terms of flexural strength, toughness, post-cracking behavior, and load-deflection of large-scale beam elements.

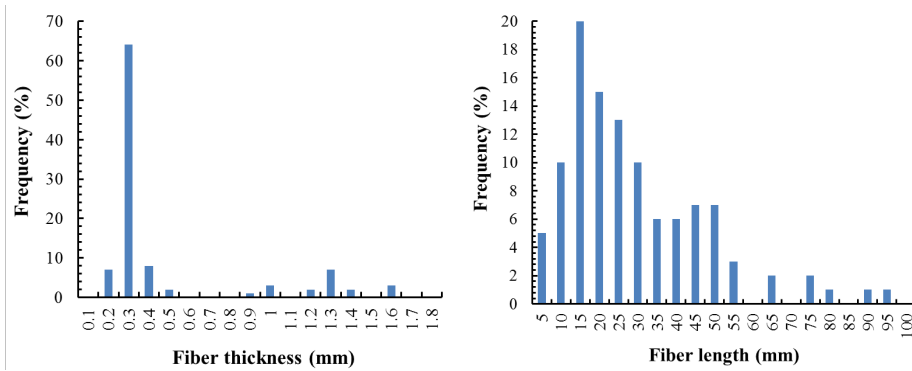


Figure 2.2. Variation in geometries of recovered steel fibers

Aggregates

The research team visited different aggregate quarries in Missouri to evaluate the performance of locally available aggregates. The locations of various aggregate quarries visited in this investigation to study the aggregate characteristics (shown in Figure A.3 in Appendix A).

In total, 17 different aggregate samples with different shapes, textures, and PSDs were taken from various aggregate quarries for preliminary evaluation, as listed in Table 2.2. The physical characteristics of aggregates, including specific gravity and water absorption, were collected from aggregate producers. A photograph of selected aggregates employed for preliminary evaluation is shown in Figure A.4 in Appendix A.

Table 2.2. Selected aggregates from different quarries for preliminary evaluation

Name	Producer	Quarry	Size	Angularity
River sand	Rolla ready Mix	Jefferson City, Missouri River	Fine	Rounded
3/8 in. (9.5 mm) Clean CapitCoInc (# 9)	Capital Sand Company, Inc.	Wardsville, Osage River	Intermediate*	Crushed
5/16 in. (7.93 mm) Gravel CapitCoInc (# 9)	Capital Sand Company, Inc.	Jefferson City, Missouri River	Intermediate	Rounded
7/16 in. (11.1 mm) Gravel CapitCoInc (# 8)	Capital Sand Company, Inc.	Jefferson City, Missouri River	Intermediate	Rounded
Sand (Osage riv.) CapitCoInc	Capital Sand Company, Inc.	Wardsville, Osage River	Fine	Crushed
3/8 in. (9.5 mm) Minus CapitCoInc (# 9)	Capital Sand Company, Inc.	Wardsville, Osage River	Intermediate	Crushed
1/2 in. (12.5 mm) Clean CapitCoInc) (# 8)	Capital Sand Company, Inc.	Wardsville, Osage River	Intermediate	Crushed
Sand (Osage riv.) CapitCoInc	Capital Sand Company, Inc.	Wardsville, Osage River	Fine	Rounded
1 in. (25 mm) Clean CapitCoInc (# 67)	Capital Sand Company, Inc.	Wardsville, Osage River	Coarse	Rounded
1/2 in. (12.5 mm) (Captial Quar) (# 8)	Capital Quarries	Rolla	Intermediate	Crushed
3/8 in. (9.5 mm) Captial Quar (# 9)	Capital Quarries	Rolla	Intermediate	Crushed
1 in. (25 mm) Captial Quar) (# 67)	Capital Quarries	Rolla	Coarse	Crushed
1/2 in. (12.5 mm) Crushed Dolo (No. 8)	Capital Quarries	unknown	Intermediate	Crushed
APAC 1 in. (25 mm), LinCreek (# 27)	APAC - Missouri, Inc	Linn Creek Quarry, Gasconade	Coarse	Crushed
APAC MFS, LinCreek	APAC - Missouri, Inc	Linn Creek Quarry, Gasconade	Fine	Crushed
1 in. (25 mm) Dolo (# 67)	Riverstone Quarry Inc	Sullivan	Coarse	Crushed
APAC MFS, Tightwad	APAC - Missouri, Inc	Tightwad Quarry, Burlington	Fine	Crushed

* Intermediate aggregates have nominal maximum size varying from 12 to 6 mm (0.47 to 0.24 in.).

The PSDs of the fine, intermediate, and coarse aggregates are shown in Figure A.5 in Appendix A. The PSDs of sampled aggregates represent a wide range of aggregates located in Missouri. The fineness modulus of fine aggregates varies from 2.56 to 4.2. The maximum nominal size of

coarse aggregate was limited to 25 mm (1 in.), which is typically used for pavement and transportation infrastructure applications.

The influence of physical characteristics of aggregates, including shape, texture, PSD, and fineness modulus on packing density was determined. The packing density of aggregate was measured using three different methods. This included the loose packing (ASTM C29), dense packing using rodding procedure (ASTM C29), and dense packing using intensive compaction tester (ICT), as shown in Figure A.6 in Appendix. ICT is generally used for compaction of granular materials, such as soil, as well as zero slump/stiff concrete such as roller compacted concrete. A constant vertical pressure is applied on a sample placed inside the cylinder mold that rotates at a gyratory angle for a maximum of 512 cycles. Due to the gyratory inclination, a shear body develops during the measurement. Shear movement under vertical pressure allows solid particles to get closer to each other, thus leading to achieving a higher packing density. The packing density of granular materials (ϕ) is calculated as follows:

$$\phi = \frac{\rho_d}{\rho_{d \max}} \quad (2.1)$$

$$\rho_{d \max} = \frac{1}{\frac{P_1}{\rho_1} + \frac{P_2}{\rho_2} + \frac{P_3}{\rho_3} + \dots} \quad (2.2)$$

where P_1 , P_2 , and P_3 are mass percentages of the various materials used in the mixture, and ρ_1 , ρ_2 , and ρ_3 refer to specific gravity values of the different materials. The applied vertical pressure should be selected below a critical value that would lead to grinding or crushing of the particles. The critical pressure for tested granular material can be determined using the difference between its PSD before and after applying the various pressure values. After preliminary evaluation of various types of aggregates under different pressure values and consolidation cycles, the parameters of ICT were fixed, as presented in Table 2.3. The vertical pressure was adjusted to 2 bar (29 psi) to avoid aggregate crushing or grinding during the IC-testing.

Table 2.3. Testing parameters selected for ICT

Parameter	Unit	Available range	Selected
Vertical pressure	bar	0.5-10	2
Number of cycles	-	2-512	256
Velocity	rpm	0-60	60
Gyratory angle	mrاد	0-50	40

University of Oklahoma

Cementitious materials

After consulting with the Oklahoma Department of Transportation (ODOT), the cementitious materials chosen for this study consisted of Type I cement, Class C fly ash, and Type K shrinkage-compensating cement. Class C fly ash is the predominant fly ash available in the State of Oklahoma, and Type K shrinkage-compensating cement is the only shrinkage compensating material currently allowed in the ODOT Specifications. Type K cement is an expansive cement

containing anhydrous calcium alumniosulfate, calcium sulfate, and uncombined calcium oxide. The chemical and physical properties of these cementitious materials are shown in Table 2.4.

Table 2.4. Chemical and physical properties of cementitious materials

Property	Type I cement	Class C FA	Type K cement
SiO ₂ (%)	19.8	35.5	7.7
Al ₂ O ₃ (%)	4.8	20.5	7.0
Fe ₂ O ₃ (%)	3.1	6.8	1.2
CaO (%)	63.2	26.3	50.1
MgO (%)	1.4	5.5	0.1
SO ₃ (%)	3.1	2.4	26.0
Na ₂ O eq. (%)	-	-	0.6
LOI (%)	2.7	0.3	2.3
Specific gravity	3.1	2.7	3.0
Blaine fineness (m ² /kg)	395	475	505

Aggregates

Aggregates for the research study consisted of natural river sand and limestone donated by Dolese Bros. Co. from their Davis Quarry (Figure A.7 in Appendix A). The fine aggregate consisted of natural river sand while the coarse aggregate consisted of two gradations, a No. 57 and a No. 8. The aggregate gradations and ODOT gradation limits are provided in Tables 2.5, 2.6, and 2.7 for the sand, No. 57, and No. 8 coarse aggregates, respectively, all of which meet the requirements. The specific gravity, dry rodded unit weight (DRUW), absorption, and LA abrasion values for each aggregate type are provided in Table 2.8. The No. 57 and No. 8 coarse aggregates met the minimum abrasion resistance requirements of the ODOT specifications.

Table 2.5. Fine aggregate gradation and percent passing limits

Sieve size/No.	Sieve opening (mm)	ODOT lower bound (%)	Percent passing tested (%)	ODOT upper bound (%)
3/8 in.	9.5	100	100	100
#4	4.75	95	99	100
#8	2.36	80	95	100
#16	1.18	50	80	85
#30	0.60	25	47	60
#50	0.30	5	14	30
#100	0.15	0	2	10
#200	0.075	0	0	3

Table 2.6. No. 57 coarse aggregate gradation and percent passing limits

Sieve Size/No.	Sieve opening (mm)	ODOT lower bound (%)	Percent passing tested (%)	ODOT upper bound (%)
1-1/2 in.	37.5	100	100	100
1 in.	25	95	99	100
3/4 in.	19	-	79	-
1/2 in.	12.5	25	47	60
3/8 in.	9.5	-	10	-
#4	4.75	0	1	10
#8	2.36	0	0.5	5
#16	1.18	-	0.4	-
#200	0.075	0	0.04	2

Table 2.7. No. 8 coarse aggregate gradation and percent passing limits

Sieve Size/No.	Sieve opening (mm)	ODOT lower bound (%)	Percent passing tested (%)	ODOT upper bound (%)
1/2 in.	12.5	100	100	100
3/8 in.	9.5	85	94	100
#4	4.75	10	13	30
#8	2.36	0	4	10
#16	1.18	0	3	5
#200	0.075	0	0	2

Table 2.8. Aggregate properties

Aggregate	Specific gravity (g/cm ³ , lb/yd ³)	DRUW (g/cm ³ , pcf)	Absorption (%)	LA abrasion (%)
Sand	2.58 (4348.7)	-	0.40	-
No. 57	2.64 (4449.9)	1.6 (101.5)	0.86	24
No. 8	2.60 (4382.4)	1.7 (104.3)	1.01	21

Admixtures

The concrete mixtures developed in this study used two types of chemical admixtures to achieve the necessary durability and workability requirements. The first consisted of a synthetic-based air-entraining admixture (AEA) that met the requirements of ASTM C 260. The second consisted of a polycarboxylate-based water reducer/high range water reducer. This admixture met the requirements of ASTM C 494 for both a Type A water reducing admixture (WRA) and a Type F high range water reducing admixture (HRWRA). The dosages of both chemical admixtures were adjusted to achieve the desired air entrainment and flowability for each specific concrete mixture.

Fibers

The concrete mixtures developed in this study used both micro- and macro-sized synthetic fibers. The micro fibers were a high-tensile strength, high modulus of elasticity, ultra-thin monofilament polypropylene fiber designed to quickly distribute uniformly throughout the concrete matrix. These fibers help to reduce plastic shrinkage, plastic settlement, and shrinkage cracking. The macro fibers in use were a high-tensile strength, high modulus of elasticity, embossed fiber manufactured from a blend of polypropylene resins. These fibers were engineered for use as secondary reinforcement to control shrinkage and temperature cracking as well as settlement cracking. They can increase residual strength in hardened concrete.

Material properties and the recommended dosages of the fibers are provided in Table 2.9. A photograph of the micro and macro fibers is shown in Figure A.8 in Appendix A.

Table 2.9. Synthetic fiber properties and recommended contents

Property	Micro fibers	Macro fibers
Specific gravity	0.91	0.91
Tensile strength (MPa, ksi)	483 (70)	586 (85)
Nominal length (mm, in.)	19.05 (0.75)	53.34 (2.10)
Equivalent diameter (microns)	12	-
Nominal aspect ratio	-	70
Recommended dosages (kg/m ³ , lb/yd ³)	0.30 (0.5)	1.78 to 7.12 (3 to 12)

Rutgers, The State University of New Jersey

Materials were obtained from various local suppliers in NJ and Eastern PA. Both fine and coarse aggregates were obtained from Clayton Concrete plant in Edison, NJ. Grade 120 slag cement and Type I portland cement were supplied by LaFarge-Holcim in Camden, NJ and Whitehall, PA, respectively. The chemical admixtures and micro polypropylene (PPE) fibers were provided by Euclid Chemical in East Brunswick, NJ. The list of suppliers of each material is summarized in Table 2.10.

Type I portland cement is tested by the manufacturer to comply with all the requirements set by ASTM C150 including chemical composition, physical properties, reactivity and strength requirements. Similar requirements are outlined in ASTM C989 for the slag cement used. Manufacturer testing assures that Grade 120 slag cement meets the reactivity and other requirements set by ASTM standards.

Table 2.10. Materials and suppliers

Material	Type	Supplier
Cement	Portland Type I	LaFarge-Holcim
Slag cement	Grade 120	LaFarge-Holcim
Fine aggregate	Concrete Sand	Clayton Concrete
Coarse aggregate	#8 (3/8 in.) granite	Clayton Concrete
Micro PPE Fibers	Polypropylene 1/4 in.	Euclid Chemical
HRWR	Plastol 5000	Euclid Chemical
AEA	AEA-92S	Euclid Chemical

Sieve analyses on both types of aggregate were performed according to ASTM C136. Coarse aggregate properties, including density, specific gravity, and absorption were determined using the procedure outlined in ASTM C127. The same properties of sand were determined using ASTM C128. The results of these tests are summarized in Table 2.11.

Table 2.11. Coarse and fine aggregate properties

Properties	Fine aggregate	Coarse aggregate
Specific gravity (unit-less)	2.62	2.83
Fineness modulus (unit-less)	2.35	6.03
Absorption (%)	1.10	0.40

The PPE fiber used in this study complies with ASTM C1116 and ASTM D7508. The properties of PPE fiber provided by the manufacturer are summarized in Table 2.12.

Table 2.12. Polypropylene fiber properties

Material	Monofilament polypropylene
Specific gravity (unit-less)	0.91
Length (in., mm)	1/4 (63.5)
Melting point (°F, °C)	320 (160)
Denier	15

2.2. Testing program

The experimental program from the three different universities are described below.

Missouri University of Science and Technology

The methodology to develop and optimize the crack-free and Eco-HPC for a given performance-based specification was carried out through four phases, as described below:

Subtask I - Optimization of binder composition

This subtask aims at optimizing the binder composition of Eco-Pave-Crete and Eco-Bridge-Crete based on the HRWR demand, packing density, flow characteristics, rheological properties, and development of compressive strength, as well as drying shrinkage and bulk resistivity. Extensive information reviewed from current literature was analyzed to finalize the laboratory testing program. This phase was conducted using concrete equivalent mortar (CEM) formulated from environmentally friendly Eco-HPC mixture design proportioned with binder contents of 320 kg/m³ (20 lb/ft³) and 350 kg/m³ (22 lb/ft³) targeted for Eco-Pave-Crete and Eco-Bridge-Crete, respectively. The mixture design parameters and material constituents targeted for different applications (Eco-Pave-Crete and Eco-Bridge-Crete) are summarized in Table 2.13.

Table 2.13. Testing program for binder optimization

Concrete type	Powder type	Content, by volume	w/cm	Cementitious materials content	Chemical admixture type	HRWR content
Eco-Pave-Crete	Ordinary portland cement (OPC)	-	0.40	320 kg/m ³ (20 in.)	High-range water reducer (HRWR)	Adjusted to secure the mini-slump flow of 135 ± 10 mm (5.3 ± 0.4 in.)
	Blast furnace slag (SL)	0-60%				
	Class C fly ash (CFA)	0-55%				
Eco-Bridge-Crete	Ordinary portland cement (OPC)	-	0.40	350 kg/m ³ (22 in.)	High-range water reducer (HRWR)	Adjusted to secure the mini-slump flow of 190 ± 10 mm (7.5 ± 0.4 in.)
	Blast furnace slag (SL)	0-60%				
	Class C fly ash (CFA)	0-55%				
	Silica fume (SF)	0-10%				

In total, 11 CEM mixtures were made with different types and replacement rates of binary and ternary cementitious materials. The mixture proportions of the evaluated mortar mixtures are listed in Table A.2 in Appendix A.

Subtask II - Optimization of aggregate characteristics

The goal of this subtask was to optimize the aggregate proportions to achieve the maximum possible packing density that was evaluated on blends of fine, intermediate, and coarse aggregates. Given various aggregate combinations and blends, the preliminary selection of optimum aggregate combination was carried out using existing theoretical packing density models to determine the optimal aggregate combinations and blends. The selected aggregate combinations (sand, intermediate, and coarse aggregates) with relatively high packing density were experimentally validated. In this phase, the results of experimentally measured packing densities were compared with those estimated from theoretical packing density models. The selected aggregate combinations were proportioned with various sand-to-total aggregate ratios to

optimize the proportioning for a given aggregate combination. In order to determine the optimum proportioning of aggregate blend, the statistical mixture design (SMD) method was utilized. SMD method provides an efficient tool for determining the predicted model as well as for optimizing the mixture proportion. In this method, the main principle is that the sum of all constituents for a given mixture is equal to 1. In general, assuming that the mixture consists of n constituents at which x represents the proportion of the i th constituent in the mixture, the sum of the material constituents is expressed as follows:

$$0 \leq x_i \leq 1 \quad i = 1, 2, \dots, n \quad \sum_{i=1}^n x_i = 1 \quad (2.3)$$

This method can be effectively employed to determine the optimum proportions of blended aggregates to achieve the maximum possible packing density. An example of various aggregate proportions used for SMD is given in Table A.3 in Appendix A. The results of packing density of blended aggregates are used as input to derive the prediction model for packing density response. The derivation of numerical model enables the determination of optimal aggregate proportion corresponding to the maximum achievable packing density. It is important to note that the model considers the shape characteristics of the aggregates.

Finally, the selected aggregate blends were ranked based on the residual error defined as the minimum deviation of aggregate blends from the target grading. The target grading was considered to be the modified Andreasen grading with the maximum and minimum particle size varying between 20 micron and 19 mm (0.75 in.), respectively.

Subtask III - Evaluation of shrinkage mitigating strategies

This subtask focused on evaluating the effect of different shrinkage mitigating materials on autogenous and drying shrinkage, and compressive strength development of CEM mixtures. Depending on the binder composition, the effectiveness of incorporating shrinkage mitigating materials can be different. Therefore, in this phase the effect of shrinkage mitigating materials on shrinkage properties of mortars proportioned with optimized binder compositions from phase 1 of this investigation was examined. The investigated materials included expansive agents (CaO-based and MgO-based), crack reducing admixture (CRA), and lightweight sand (LWS). In total, 20 mortars made with different binder compositions and shrinkage mitigating materials were evaluated, as given in Table A.4 in Appendix A. The experimental program, including workability, shrinkage, mechanical properties, and durability is presented in Table A.5 in Appendix A.

The investigated mixtures from this subtask were also subjected to different durations of initial moist curing to evaluate the influence of curing regime on the performance of various shrinkage mitigating materials. Table A.6 in Appendix A presents the proposed initial moist curing duration of the mixtures.

Subtask IV - Development of crack-free Eco-Crete

This subtask was carried out to evaluate and optimize Eco- and crack-free HPC. Based on the results from previous phases, the effect of different binder compositions, aggregate characteristics, and shrinkage mitigating materials were evaluated and the results were analyzed

to design Eco- and crack-free HPC with different targeted applications (Eco-Pave-Crete and Eco-Bridge-Crete). The investigated mixture design parameters for the design of Eco-HPC are summarized in Table A.7 in Appendix A.

University of Oklahoma

The baseline mixtures for comparison are two standard ODOT mixtures, one for pavement construction, Class A, and one for bridge superstructure construction, Class AA. The ODOT requirements for these two standard mixtures are shown in Table 2.14. The slump requirement is prior to addition of any water reducer or high range water reducer.

Table 2.14. Baseline ODOT mixture design requirements

Class of concrete	Minimum cement content (kg/m ³ , lb/yd ³)	Air content (%)	w/cm	Slump (mm, in.)	Minimum 28-day compressive strength (MPa, psi)
A	871 (517)	6 ± 1.5	0.25 – 0.48	50.8 ± 25.4 (2 ± 1)	20.7 (3,000)
AA	951 (564)	6.5 ± 1.5	0.25 – 0.44	50.8 ± 25.4 (2 ± 1)	27.6 (4,000)

The following sections discuss the binder optimization and aggregate optimization techniques that were employed during the mixture development phase.

(1) Binder optimization technique

The binder composition was optimized through application of the modified Andreasen and Andersen model, as shown in Eq. (2.4):

$$P(D) = \frac{D^q - D_{min}^q}{D_{max}^q - D_{min}^q} \quad (2.4)$$

where D is the particle size (μm), $P(D)$ is a fraction of the total solids being smaller than size D , D_{max} is the maximum particle size (μm), D_{min} is the minimum particle size (μm), and q is the distribution modulus (Yu et al., 2013).

Different types of concrete can be designed using Eq. (2.4) by applying different values for the distribution modulus, q , as it determines the proportion between the fine and coarse particles in the mixture. For mixtures containing a high amount of fine particles, or when optimizing just the cementitious or paste fraction of a mixture, a value of 0.22 or 0.23 for q is recommended (Yu et al., 2013). The technique for optimizing the composition is to adjust the proportions of each material in the mixture until the combined gradation matches the target curve, as represented by Eq. (2.4), as closely as possible. A Least Squares Method (*LSM*) is commonly employed in an optimization algorithm, where the deviation between the target curve and composed mixture is expressed by the sum of the squares of the residuals (*RSS*) at defined particles sizes, as shown in Eq. (2.5). The optimum composition is reached when the *RSS* value is minimized (Yu et al., 2013).

$$RSS = \sum_{i=1}^n (P_{mix}(D_i^{i+1}) - P_{tar}(D_i^{i+1}))^2 \quad (2.5)$$

where P_{mix} is the composed mixture, and P_{tar} is the target gradation calculated from Eq. (2.4).

(2) Aggregate optimization technique

The aggregate composition was optimized through application of the following three techniques:

- coarseness factor chart
- 0.45 power chart
- individual percent retained chart

The coarseness factor (CF) chart is based on volumetric relationships between the coarse, intermediate, and fine fractions of the combined aggregate (Richardson, 2005). The coarse fraction, Q , is the material retained on the 3/8 in. sieve, the intermediate fraction, I , is the material passing the 3/8 in. sieve and retained on the #8 sieve, and the fine fraction, W , is the material finer than the #8 sieve and coarser than the #200 sieve.

As shown in Figure A.9 in Appendix A, the CF chart relates the percentages of each aggregate fraction to characteristics of the mixture, such as harshness, sandiness, excessive shrinkage, pumpability, finishing characteristics, proneness to segregation, and so forth. The horizontal axis plots the coarse fraction as a percentage of the coarse plus intermediate fractions, $[Q/(Q+I)] \times 100$, and the vertical axis plots the fine fraction as a percentage of the total aggregate volume, $[W/(Q+I+W)] \times 100$. The chart also contains delineation zones for predicting behavior of a concrete mix containing the specified aggregate proportions. Zone I signifies coarse, gap-graded mixtures that tend to segregate, Zone II signifies well-graded aggregate applicable to most mixtures depending on use, Zone III signifies 3/4 in. and finer pea gravel mixtures, Zone IV signifies over-sanded mixtures that tend to be sticky, and Zone V signifies rocky mixtures most applicable for mass concrete. The trend bar, labeled “0”, is an optimal zone that requires excellent control of the mix to prevent problems. Zone II is further subdivided into five areas: II-1 indicates excellent mix behavior but caution to prevent problems, II-2 indicates excellent paving and slip form applications, II-3 indicates high quality slab mixtures, II-4 indicates good general mixtures, and II-5 varies with material characteristics and construction needs.

The 0.45 power chart is based on an ideal particle size distribution to achieve the maximum density of the aggregate materials within a concrete mixture (Richardson, 2005). The combined coarse and fine aggregate gradation is plotted as shown in Figure A.10 in Appendix A, with the percent passing on the vertical axis and the sieve sizes raised to the 0.45 power on the horizontal axis. The maximum density line is drawn from the origin to the intersection of the 100 percent passing line with either the first sieve to retain aggregate or the nominal maximum size. The optimum grading will follow the maximum density line with the exception of the fines, which tend to fall noticeably below the reference line at sieve sizes smaller than #16. The 0.45 power chart is based on Eq. (2.6):

$$P_i = \left(\frac{d_i}{D}\right)^{0.45} \quad (2.6)$$

where P_i is the percentage passing the i^{th} sieve, d_i is the opening size of the i^{th} sieve, and D is the maximum particle size (nominal maximum size).

The individual percent retained chart also uses the combined gradation of the coarse and fine aggregates but uses percent retained on each sieve size. A typical chart is shown in Figure A.11 in Appendix A. There are minimum and maximum boundary lines that the gradation should fall between, typically at 8% and 18%, thus the chart is also commonly referred to as the 8/18 method. This approach ensures an adequate percentage of intermediate particle sizes, which tends to improve particle packing and thus reduce the need for mortar to fill voids. By using mortar to fill voids, less of it is available to provide workability, and the mix becomes harsh and difficult to finish (Richardson, 2005).

Rutgers, The State University of New Jersey

A total of four fiber-reinforced concrete mixtures were prepared for this experimental study. The proportions of these mixtures are based primarily on the findings of a previous study conducted by the Virginia Transportation Research Council (Brown et al., 2008). All samples for each mixture were cast from a single batch to ensure uniformity. The mixture proportions are summarized in Table 2.15. In an effort to isolate variables, mixture proportions were kept identical in all four mixtures except fiber content. Each mixture contains 4005 kg/m³ (675 lb./yd³) of total cementitious material, while 35% of which is Grade 120 slag cement and 65% of which is Type I portland cement. A w/cm of 0.425 is targeted with a tolerance of ± 0.02. Equal amounts of coarse and fine aggregates of 852 kg/m³ (1,436 lb/yd³) were used in each mixture, and the coarse-to-fine ratio is 1-to-1.

Table 2.15. Mixture proportions

Mixture ID	PPE 0.00	PPE 0.10	PPE 0.15	PPE 0.20
Type I Portland cement (kg/m ³ , lb/yd ³)	260 (439)	260 (439)	260 (439)	260 (439)
Grade 120 slag cement (kg/m ³ , lb/yd ³)	140 (236)	140 (236)	140 (236)	140 (236)
Total cementitious material (kg/m ³ , lb/yd ³)	400 (675)	400 (675)	400 (675)	400 (675)
W/C ratio	0.425	0.425	0.425	0.425
#8 coarse aggregate (kg/m ³ , lb/yd ³)	852 (1436)	852 (1436)	852 (1436)	852 (1436)
Fine aggregate (kg/m ³ , lb/yd ³)	852 (1436)	852 (1436)	852 (1436)	852 (1436)
HRWR (kg/m ³ , oz./yd ³)	2.5 (68)	3 (81)	3 (81)	3.5 (95)
Fiber (% by volume)	0	0.1	0.15	0.2

This research was carried out using PPE fibers. Fiber volume was varied between mixtures, beginning with the control mixture (PPE 0.00) having no fibers and other mixtures (PPE 0.10, PPE 0.15 and PPE 0.20) having 0.10%, 0.15% and 0.20% fiber by volume, respectively. As the addition of fibers resulted in lower workability, additional HRWR was added to the batch until the desired workability and flowability were met to compensate for the loss in workability. The

control mixture included 2.5 kg/m³ (68 fl. oz./yd³) of HRWR, while PPE 0.10 and PPE 0.15 mixtures contained 3 kg/m³ (81 fl. oz./yd³) PPE 0.20 mixture utilized 3.5 kg/m³ (95 fl. oz./yd³) of HRWR.

2.3. Mixing procedure

The following mixing procedures were used for the work carried out at Missouri S&T for mortar and concrete mixture. Similar mixing protocols was used for the work that conducted by University of Oklahoma, and Rutgers, The State University of New Jersey, except that PPE fibers were added in the last step for concretes produced by Rutgers, The State University of New Jersey.

The mixing sequence for the mortar mixtures consisted of homogenizing the sand for 60 sec, before introducing half of the mixing water. The cementitious materials were then added and mixed for 30 sec followed by the HRWR diluted in the remaining water. The mortar was mixed for 3 min and remained at rest for 2 min for fluidity adjustment before remixing for 3 additional min.

The mixing procedure for the concrete mixtures that were prepared using a drum mixer with 150 L (5 ft³) capacity is as follows:

- (1) Homogenize sand and pre-wetted lightweight sand (if used) for 60 sec.
- (2) Incorporate coarse aggregate, fibers (if used), half of the mixing water, and AEA and mix for 1 min.
- (3) Add the powder materials (and EX if used) and mix for 30 sec.
- (4) Add half of the remaining water, and mix for 1 min.
- (5) Add the remaining water and HRWR, and mix for 3 min (and SRA if used).
- (6) Keep the concrete at rest for 2 min followed by remixing for additional 2 min.

2.4 Test methods

2.4.1. Test methods for mortar mixtures

Concrete equivalent mortar (CEM) mixtures were made to evaluate the performance of different SCM types and replacement rates on fresh and hardened properties as well as assess the effect of various shrinkage mitigating materials on autogenous shrinkage, drying shrinkage, and compressive strength development. The laboratory investigations used for CEM are presented below.

Hydration kinetics

The heat flow evolution during hydration of the investigated CEMs was determined using isothermal calorimetry (Figure A.12 in Appendix A) at a constant temperature of 20 °C (68 °F) for 3 days. The thermal power and energy measured to maintain the temperature at 20 °C (68 °F) were then used to evaluate the influence of SCM replacements on reaction kinetics and cumulative heat released of the mortar mixtures.

Rheological properties

The coaxial cylinders rheometer with inner and outer radii of 50 and 62 mm (2.0 and 2.4 in.), respectively, was employed to determine the rheological properties of mortar, as shown in Figure 2.13 in Appendix A. The testing procedure consisted of pre-shearing the sample at the maximum rotational velocity applied during the test for 30 sec, followed by a time step decrease of the rotational velocity from 0.5 rps (10 steps) to 0.025 rps. The rheological properties were obtained by taking the average of the torque and rotational velocity during the last four seconds of each step, ensuring the fact that the torque was in equilibrium. The Reiner–Riwlin transformation was applied to calculate yield stress and plastic viscosity. Special attention was provided during the measurements and analysis to identify and eliminate artefacts, such as thixotropy, segregation, and plug flow. In the case of potential plug flow, the correction was applied by means of an iterative procedure (Feys et al., 2015). In parallel to the rheological properties, the mini-slump flow test was used to evaluate the fluidity retention of the mortar mixtures at 10 and 70 min following the first contact of cementitious materials with water.

Autogenous shrinkage

Autogenous shrinkage of mortars made with different shrinkage reducing strategies was determined according to ASTM C1698, as seen in Figure A.14 in Appendix A. For each mixture, two corrugated cylindrical samples were prepared using polyethylene tubes. According to ASTM C1698, the initial reading for the autogenous shrinkage of a mortar sample should be carried out at the final setting time of the mortar. Therefore, the final setting time of mortar mixtures was determined according to ASTM C403, as indicated in Figure A.15 in Appendix A.

Drying shrinkage

Drying shrinkage of the mortar (ASTM C596) was determined using a digital type extensometer to measure changes in length of prismatic specimens measuring $25 \times 25 \times 285$ mm ($1 \times 1 \times 11.25$ in.), as shown in Figure A.16 in Appendix A. After demolding at 24 h, the beam specimens were immersed in water for 6 days, then the samples were transferred to a temperature and humidity controlled room set at 23 ± 1 °C (73.4 ± 33.8 °F) and $50\% \pm 3\%$ RH, and the shrinkage was monitored until the age of 56 days.

Compressive strength

The 1-, 3-, 7-, 28-, 56-, and 91-day compressive strengths of mortars were determined using 50-mm cube specimens according to ASTM C109. The cubes were demolded after one day and stored in lime-saturated water at 21 ± 2 °C (69.8 ± 35.6 °F) until testing age. The results of compressive strength represent the average values of three specimens. The values of coefficient of variation (COV) of compressive strength results were lower than 5%.

2.4.2. Test methods for concrete mixtures

The experimental matrix carried out on the concrete phase is summarized in Table 2.16.

Mechanical properties

Cylindrical specimens measuring 100×200 mm (4×8 in.) were cast to determine compressive strength (ASTM C39), modulus of elasticity (ASTM C469), and splitting tensile strength (ASTM C496) at 3, 28, 56, and 91 days. Prismatic specimens measuring $75 \times 75 \times 400$ mm ($3 \times 3 \times 16$ in.) were cast to determine the flexural strength and toughness of fiber-reinforced concrete (FRC)

according to ASTM C1609 (Figure A.17 in Appendix A). The toughness of the FRC was calculated from the load-deflection curve under displacement control.

Table 2.16. Experimental matrix for concrete phase

Concrete property	Concrete type		Test
	Eco-Pave-Crete	Eco-Bridge-Crete	
Workability	*	*	Unit weight (ASTM C138), air content (ASTM C 231), slump
Mechanical properties	*	*	Compressive strength (ASTM C39) at 3, 7, 28, 56, and 91 days
	*	*	Modulus of elasticity (ASTM C469), splitting tensile strength (ASTM C496) at 56 days
	*	*	Flexural strength (ASTM C78) at 56 and 91 days
	*	*	Flexural performance of fiber reinforced concrete (ASTM C1609) at 56 and 91 days
Durability	*	*	Resistance to freezing and thawing (ASTM C666, Proc. A)
	*	*	De-icing salt scaling resistance (ASTM C672)
	*	*	Water absorption (ASTM C642) at 56 and 91 days
	*	*	Sorptivity (ASTM C1585) at 56 and 91 days
		*	Surface resistivity (AASHTO T95) at 56 and 91 days
		*	Bulk electrical conductivity (ASTM C1760) at 56 and 91 days
Shrinkage properties	*	*	Abrasion resistance (ASTM C944) at 56 days
	*	*	Autogenous shrinkage (ASTM C1698) and drying shrinkage (ASTM C157)
	*	*	Restrained shrinkage ring test (ASTM C1581)

Durability

The abrasion resistance of concrete mixtures was evaluated in accordance with ASTM C944, as shown in Figure A.18 in Appendix A. The specimens were moist cured for 56 days before testing. The abrasion test consists of three abrasion cycles at which each cycle lasts two minutes. A double load of 197 N was applied at a rate of 300 rpm using a drill press. After each cycle, mass loss was calculated by subtracting the initial from final mass.

Prisms measuring 75 × 75 × 400 mm (3 × 3 × 16 in.) were prepared to evaluate freeze-thaw resistance of concrete mixtures according to the ASTM C666, Procedure A (Freezing and thawing in water). Given pozzolanic reactivity of SCMs, concrete made with a high replacement rate of SCMs requires higher curing time compared to concrete made with 100% OPC. In general, the use of longer period of moist curing for concrete containing high volume of SCMs can result in a denser microstructure and lower capillary porosity compared to the similar mixture subjected to lower moist curing period. Therefore, the specimens were moist cured for

56 days before freeze-thaw testing. Specimens were subjected to 300 freeze-thaw cycles, and after every 36 cycles, the mass loss and transverse frequency of concrete specimens were monitored. The ultrasonic pulse velocity test was used to determine the dynamic modulus of elasticity of the specimens. The freeze-thaw chamber and ultrasonic pulse velocity instrument is shown in Figure A.19 in Appendix A.

The de-icing salt scaling was determined in accordance with ASTM C672. Slabs had a minimum surface area of 0.045 m² (69.75 in.) and 75 mm (2.95 in.) in depth. A dike was placed on the finished surface of the specimen. This dike was used for ponding the surface of the specimen with a solution of calcium chloride with a concentration of 4.0%. The specimens were subjected to 50 cycles of freezing and thawing. The curing regime consisted of 28 days of moist curing followed by 14 days of air drying at 23 ± 1 °C and 50% ± 3% relative humidity. The top surface of the slab was washed, and the damage was qualitatively assessed after every five cycles. In this procedure, the surfaces of samples were rated based on a scale of 0 to 5, corresponding to no scaling to severe scaling, respectively. The mass of scaling residue of the tested mixtures was also measured.

The electrical resistivity measurement was used to classify the concrete according to the corrosion rate. The measurement of electrical resistivity was determined using two different methods; direct two-electrode method (ASTM C1760) and the four-point Wenner probe method (AASHTO TP 95-11), corresponding to bulk electrical conductivity and surface resistivity, respectively (Figure 2.3). The electrical resistivity was measured using cylindrical samples measuring 100 mm (3.94 in.) in diameter and 200 mm (7.87 in.) in height and cured in saturated lime water until the age of testing. The electrical resistivity is calculated as follows:

$$\rho = R \times k \quad (2.7)$$

where ρ is the resistivity, and R and k refer to measured resistance and geometry correction factor, respectively. The geometry correction factor for surface resistivity and bulk electrical conductivity can be calculated as:

$$k(\text{surface resistivity}) = \frac{2\pi a}{1.1 - \frac{0.73}{d/a} + \frac{7.82}{(d/a)^2}} \quad (2.8)$$

$$k(\text{bulk electrical conductivity}) = \frac{A}{L} \quad (2.9)$$

where d , A , a , and L refer to diameter, cross section area, probe spacing, and length of the specimen, respectively.



Figure 2.3. Bulk electrical conductivity (left) and surface resistivity (right)

Cylindrical specimens measuring 100×100 mm (3.94×3.94 in.) were sampled to determine the water absorption of concrete according to ASTM C642. This test method determines the water absorption after immersion in water (B). Samples were dried in an oven at a temperature of $110 \pm 5^\circ\text{C}$ ($230 \pm 41^\circ\text{F}$) until the difference between any two consecutive mass values is less than 0.5% of the obtained lowest value (A). The water absorption of concrete specimens is calculated as follows:

$$\text{Absorption after immersion} = [(B-A)/A] \times 100 \quad (2.10)$$

The sorptivity of concrete mixtures was determined in compliance with ASTM C1585. The test consisted of measuring the increase in mass of a disc specimen at given intervals of time when permitted to absorb water by capillary suction. After 56 days moist curing, cylinder samples from each mixture were cut in three disc specimens measuring 50 mm (2 in.). The specimens were then placed in the environmental chamber at a temperature of 50°C (122°F) and RH of 80% for 3 days. After the 3 days, each specimen was placed inside a sealable container and stored at a temperature of $23 \pm 2^\circ\text{C}$ ($73.4 \pm 35.6^\circ\text{F}$) for at least 15 days until the samples reached the equilibrium mass at which the moisture distribution is consistent within the test specimen. Prior to absorption testing, the side surface of the samples was sealed with aluminum tape and the top surface was covered with plastic wrap. This was to prevent drying of the sample from these surfaces. The test procedure is schematically illustrated in Figure A.20 in Appendix A. The amount of absorbed water is normalized by the cross-section area of the specimen exposed to the fluid as follows:

$$I = \frac{m_t}{a \times d} \quad (2.11)$$

where I is the absorption, m_t is the specimen mass at time t (gr); a is the exposed area of the specimen (mm^2), and d is the density of the water. The absorbed fluid volumes are then plotted as a function of the square root of time. The initial sorptivity is determined from the slope of the curve during the first 6 h according to ASTM C1585, while secondary sorptivity is determined using the slope of the same measurements between 1 day and 7 days, as outlined in ASTM C1585.

Shrinkage and cracking resistance

Drying shrinkage of concrete mixtures (ASTM C157) was determined with a digital type extensometer using prismatic specimens measuring $75 \times 75 \times 285$ mm ($3 \times 3 \times 11.25$ in.). After demolding at 24 h, the prismatic specimens were immersed in water for 6 days. The samples were

then stored in a temperature and humidity controlled room at $23 \pm 1^\circ\text{C}$ ($73.4 \pm 33.8^\circ\text{F}$) and $50\% \pm 3\%$ RH. Shrinkage was then measured until stabilization of shrinkage readings. Similarly, prismatic samples were cast and sealed after demolding at 24 h using adhesive aluminum tape to determine autogenous shrinkage. Figure A.21 in Appendix A shows the shrinkage setup used for sealed and unsealed specimens.

A ring-type test (ASTM C1581) was used to evaluate the resistance of concrete to restrained shrinkage cracking (Figure A.22 in Appendix A). The test consists of casting concrete in an annular spacing with two concentric rings with an inner rigid steel ring instrumented with three electrical strain gauges. The gauges are used to monitor stress development induced by restrained shrinkage in the concrete. The steel strain is monitored starting immediately after casting with subsequent readings taken every 20 min until the concrete shell element begins to crack. A sudden decrease in steel strain refers to shrinkage cracking of the concrete ring. Two concrete ring specimens were cast for each mixture. The concrete rings were moist cured for 24 h under wet burlap after casting. The specimens were demolded and moist cured for an additional two days before the initiation of the drying process. After the curing process, the top surface of the ring specimen was sealed with adhesive aluminum tape, thus restricting drying to the outer circumferential surface of the concrete ring. The ring specimens were stored at $23 \pm 1^\circ\text{C}$ ($73.4 \pm 33.8^\circ\text{F}$) and $50 \pm 3\%$ RH and the results were continuously recorded until the onset of restrained shrinkage cracking.

Fresh concrete property test

The team measured the concrete fresh properties in accordance with ASTM C1611 which uses the inverted slump cone to measure slump flow, as shown in Figure A.23(a) in Appendix A. The time elapsed between the lifting of the slump cone and the time for the slump flow reaching a 20 in. diameter was measured as the T20 time in seconds. When the flow stopped, the largest diameter as well as a 90° offset of that diameter were recorded and averaged for the slump flow.

The segregation and bleeding were observed after the slump flow test and before cleaning the base plate. A VSI of 0 (zero) indicates no bleeding or segregation, and a VSI of 1 means slightly visible bleeding in the form of sheen on the concrete. When a slight mortar halo appears around the edges of the slump flow less than 12.7 mm ($1/2$ in.) in thickness, the concrete is deemed unstable with a VSI of 2. If the halo exceeds 12.7 mm ($1/2$ in.) in thickness or a pile of aggregate is visibly segregated in the center of the slump flow, a VSI of 3 is assigned and the concrete is deemed highly unstable. Only VSI less than 1 is acceptable for application. Moreover, the J-ring test was performed in accordance with ASTM C1621 to determine passing ability as shown in Figure A.23(a) in Appendix A. A 12 in. diameter of metal J-Ring with 16 vertical rebars was used for this test. The slump cone was filled and lifted as it was in the slump flow test, so that the SCC flew through the vertical rebars. When the concrete stopped flowing, the largest diameter and 90° -degree offset diameter from the largest were measured and averaged to calculate the J-ring flow. In general, the J-ring value is compared to the slump flow to determine the blocking assessment. A difference of less than 1 in. indicates no significant blocking of the flow. When the difference is between 25.4 and 50.8 mm (1 and 2 in.), minimal blocking may be occurring. The difference of greater than 50.8 mm (2 in.) indicates extreme blocking.

In addition to the ASTM standards, the team also performed the L-box test as a comparative measure of passing ability as shown in Figure A.24 in Appendix A (Raymond, 2012). The L-box consists of a 24 in. high, 101.6 × 203.2 mm (4 × 8 in.) shaft with a hole measuring 152.4 × 203.2 mm (6 × 8 in.) at the bottom. The gate covering the hole leads to a tray measuring 609.6 mm (24 in.) long and 203.2 mm 8 in. wide onto which the concrete flows. The concrete was scooped into the top of the shaft and allowed to fall to the bottom while the gate was closed. Once the shaft was filled, the concrete sat for one minute and then leveled without the use of any compaction or vibration. The gate was then lifted so that the concrete was allowed to pass through three 9.5 mm (3/8 in.) diameter steel rebar (12.7 mm apart) [2 in. apart] and onto the tray. After the flow stopped, the concrete height was taken at the wall of the gate opening (h1) and at the opposite end of the tray (h2). The ratio of these two heights (h1/h2) was taken and compared between mixtures to see the performance of each mixture in a confined space.

A Type B pressure air meter was used to determine the air content of the concrete mixtures according to ASTM C231. The pressure air test was performed immediately after the slump flow test. The unit weight, yield and gravimetric air content were measured using the procedure dictated by ASTM C138. The test used the same measuring bowl used for the pressure air content to calculate concrete density and the air content by means of the gravimetric air content test. The difference in the two values, the theoretical density of the components and the actual density of the concrete, is due to the entrainment of air within the concrete.

Mechanical property test

Compressive strength tests were performed at 28 days after casting according to ASTM C39. The cylinders were capped with a sulfur capping compound in accordance with ASTM C617 to ensure a flat surface for consistent results. Three cylinders were used and the average values were determined to represent the strength at 28 days. If the compressive strength varied more than 10% from other results, the result was discarded and additional cylinder was tested.

Splitting tensile strength and modulus of elasticity were measured for each mixture at 28 days in accordance with ASTM C496 and C469, respectively. For tensile strength, each specimen was placed horizontally in the testing machine between two 1 in. wide pieces of plywood. The cylinder was then loaded until splitting occurred. Three specimens were tested for each mixture to ensure accuracy, and 10% variance rule was also applied. For modulus of elasticity, samples were also capped with sulfur as the samples for compression test. The cylinders were loaded until 35%-40% of their compressive strength with displacement readings being taken every 1813.37 kg (4,000 lb). Each cylinder was tested twice for consistency and three specimens were tested for each mixture.

Free shrinkage test

Free shrinkage measurements were taken regularly using a length comparator according to ASTM C157. Two prism samples 76.2 × 76.2 × 297.69 mm (3 in. wide × 3 in. deep × 11-3/4 in. long) per mixture were prepared with two embedded stainless steel studs at both ends. Samples were stored and tested in an environmentally controlled environment at 23.3 °C (74 °F) and 50% relative humidity to prevent any thermal expansion. At each testing period, a reference bar was placed into the length comparator and the minimum length reading was taken. The prism sample was then placed into the length comparator and the minimum measurement was recorded. The

process was repeated for each sample at least twice per week over the course of testing period of 28 days.

Restrained shrinkage test

Two AASHTO T334 rings were collected for each mixture design. The AASHTO standard ring consists of a 12.7 mm (1/2 in.) thick steel ring with an outer diameter of 304.8 mm (12 in.) and an inner diameter of 11 in., and 3 in. thick and 6 in. high concrete ring surrounding the steel ring. As the concrete shrinks, the steel ring provides restraint to the concrete ring and induces tensile stress resulting in cracking. A slight modification of testing method was made for the AASHTO standard ring based on a previous study performed by the RIME Team (Nassif, 2007). Both rings have four (4) foil strain gauges (FSGs) attached at four equidistant mid-height locations on the ring as per AASHTO T334 to measure the strain applied on the steel ring. In addition to FSGs, one AASHTO ring has an additional six (6) vibrating wire strain gauges (VWSGs) to monitor the strain applied on the concrete ring. Both ends of the VWSGs were embedded into the concrete by 76.2 mm (3 in.) bolts at the time of casting, and 6 VWSGs formed a closed hexagon loop along the top surface. The finished hexagonal VWSG setup is shown in Figure A.25 in Appendix A and the setup of modified AASHTO ring is shown in Figure A.26 in Appendix A. The advantage of using VWSG is to monitor directly the strain and deformation occurring within the concrete, and therefore, the VWSGs are used to signal the cracking location. FSGs are manufactured by Vishay Micro-Measurements and measure the strain using a Wheatstone bridge circuit. In a Wheatstone bridge, a charge is run through the circuit and the resistance is measured. As the gauge lengthens or shortens, the circuit itself changes as well, and the resistance is altered. The change in resistance is easily converted to a strain value using a gauge factor provided by the manufacturer. To ensure proper functionality, the surface of the ring is smoothed and cleaned prior to gauge installation. FSGs are glued to the steel ring along the circumference and sealed by a layer of epoxy to prevent moisture from damaging the gauge. VWSGs manufactured by Geokon Inc. have an incased steel wire anchored tightly at two ends. As the VWSG is compressed or extended, the frequency at which this wire vibrates is altered, and a plucking coil reads the frequency. The plucking coil is attached to a sensor wire that is attached to a data acquisition system (DAS). Using the gauge factor provided, the change in frequency can be converted to a strain value.

After 1 day wet-curing period covered by the wet burlap and plastic sheet, a coat of paraffin wax was poured along the top surface of the ring. The ring was placed on a plexiglass surface and a lining of silicone caulk was spread along the bottom edge of the ring. This process was intended to prevent any evaporation other than from side surfaces. The strain gauges (FSGs and VWSGs) were wired to the data acquisition system (DAS). Strain readings were collected at two-minute intervals and readings were monitored for any indication of cracking. If cracking was suspected, the surface of the ring was observed using a digital microscope with up to 200x magnification to quantify the crack extent and to develop a crack map until the ring reaches 28 days in age.

Data acquisition system

All sensors (FSGs and VWSGs) were connected to the DAS and data was recorded once every two minutes. A modular system manufactured by Campbell Scientific was used, as shown in Figure A.27 in Appendix A. The system allows for the collection of data from both types of sensors at two-minute intervals for a given setup, to convert the raw data into strain values, and

to store the strain data on a hard drive. The collected data was compiled every 2 to 3 days to check the temperature and humidity readings (for a consistent environment) and the strain (for any indication of cracking). If any FSG showed any jumps or relaxation in stresses or VWSG exceeded the cracking resistance defined by the concrete's tensile strength divided by the elastic modulus, the surface of the ring was monitored on the same day using the digital microscope to quantify the cracks.

3. TEST RESULTS AND DISCUSSION

Fresh and hardened properties of optimized binder and aggregate systems carried out on CEM mortar, development of Eco- and crack free HPC are discussed in the following section. The main findings of several efforts carried out by the various universities are discussed below.

Missouri University of Science and Technology

3.1. Optimization of binder composition

In total, 11 CEM mixtures were made with different types and replacement rates of binary and ternary cementitious materials. The mixture proportions of the evaluated mortar mixtures are presented in Table 3.1. The binder contents of the mortars varied between 320 kg/m³ (20 lb/ft³) and 350 kg/m³ (22 lb/ft³) targeted for Eco-Pave-Crete and Eco-Bridge-Crete, respectively. As presented in Table 3.1, the partial substitution of cement by SCMs varied from 40% to 70%, by total volume of binder content. Given different target slump consistencies aimed for different applications, the HRWR dosage was adjusted to secure the mini-slump flow of 135 ± 10 mm (5.3 in.) and 190 ± 10 mm (7.5 in.) in the mortar fraction of the Eco-Pave-Crete and Eco-Bridge-Crete, respectively. The water-to-cementitious material ratio (w/cm) was fixed at 0.4 for all mixtures.

Table 3.1. Mixture proportions of investigated CEM mixtures (volume-basis)

Type	Mixture no.	Codification	OPC	SL	CFA	SF	Binder content (kg/m ³ , lb/ft ³)	HRWR, by mass of binder (%)
Eco-Pave-Crete having mini-slump flow of 135 ± 10 mm (5.3 ± 0.4 in.)	1-1	1-OPC	100	0	0	0	320 (20)	0.34
	1-2	1-FA55	45	0	55	0	320 (20)	0.27
	1-3	1-SL60	40	60	0	0	320 (20)	0.28
	1-4	1-SL20FA35	45	20	35	0	320 (20)	0.26
	1-5	1-SL20FA50	30	20	50	0	320 (20)	0.29
Eco-Bridge-Crete having mini-slump flow of 190 ± 10 mm (7.5 ± 0.4 in.)	2-1	2-OPC	100	0	0	0	350 (22)	0.42
	2-2	2-FA40	60	0	40	0	350 (22)	0.27
	2-3	2-SL60	40	60	0	0	350 (22)	0.28
	2-4	2-FA40SF5	55	0	40	5	350 (22)	0.38
	2-5	2-SL60SF5	35	60	0	5	350 (22)	0.38
	2-6	2-SL20FA35	45	20	35	0	350 (22)	0.27

Note: CFA: Class C fly ash, SL: slag, and SF: silica fume

3.1.1. Time dependent rheological properties

The effect of SCM substitutions on time dependent rheological properties of the investigated binary and ternary binder compositions is presented in Figure 3.1. The retention of rheological

properties was evaluated over 70 min following the initial contact of the cementitious material with water. The tested mixtures remained covered in the recipient of the viscometer at rest between the 10 and 70 min test durations. Regardless of the binder composition, all of the mixtures exhibited similar yield stress values, which is due to the similar initial fluidity values. Except for binary mixture containing 60% slag cement replacement, all of the investigated binary and ternary mixtures had relatively lower yield stress and plastic viscosity values at 70 min of age compared to the reference mixture made with 100% OPC. In general, the high volume replacement of cement by slag cement was shown to increase the yield stress and plastic viscosity by 20% and 15%, respectively, after 70 min of age compared to the reference mixture. However, the ternary blends of 60% SL and 5% SF exhibited lower yield stress and plastic viscosity. This can be attributed to the lower inter-particle friction and higher packing density of such binder due to the use of SF replacement, thus reflecting lower changes in rheological properties over time. The highest retention of rheological properties (lowest variations in results between 10 and 70 min of age) was observed for binary mixture containing 40% FA. This corresponds to the fact that the proper substitution of cement by SCMs can lead to longer retention of rheological properties and lower fluidity loss with respect to the mixture with 100% cement. Caufin and Papo (1986) reported that hydration resulting from portland cement increases the solid volume concentration through the production of a large number of very fine particles, thus increasing viscosity and yield stress. Therefore, when substituting cement by a quantity as high as 50% SCM, it can be expected that the magnitude of restructuring and strength of inter-particle links can be reduced due to the lower reactivity of such materials. This results in lower variation in rheological properties over time.

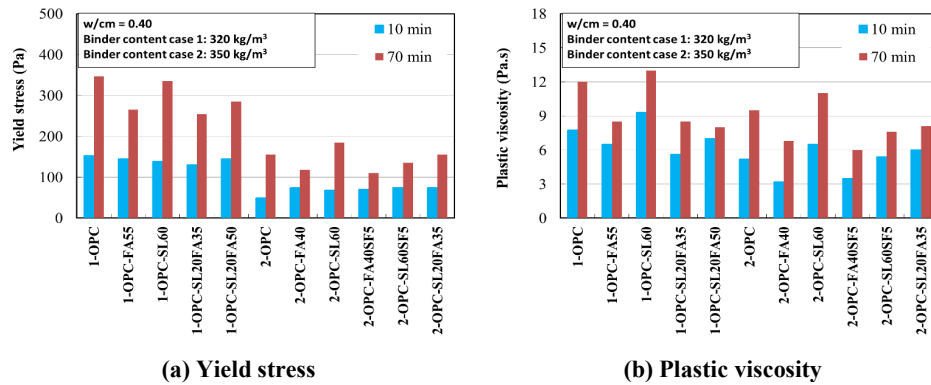


Figure 3.1. Effect of SCM substitutions on rheological properties of mortars

It is important to point out that all of the mixtures made with 350 kg/m³ (22 lb/ft³) and initial mini-slump flow value of 190 ± 10 mm (7.5 ± 0.4 in.) had lower variation in rheological properties over time compared to the similar mixtures made with 320 kg/m³ (20 lb/ft³) and initial mini-slump flow of 135 ± 10 mm (5.3 ± 0.4 in.). Lower degree of variation in rheological properties contributes to the ease of handling and casting operations of the mixture.

3.1.2. Heat of hydration

The heat flow evolution and cumulative heat release (normalized per gram binder) of the investigated mixtures is shown in Figure 3.2. As expected, the partial substitution of cement by FA and SL reduces the heat evolution of the matrix, given lower reactivity and dilution effect of the SCMs. Generally, the total amount of heat liberated depends on the pozzolanic activity and proportion of the added SCMs (Snelson et al., 2008). An increase in the FA replacement resulted in a longer induction period and lower heat flow at peak, while the incorporation of SL shifted the peak heat toward the left side, corresponding to a shorter induction period, and increased the slope of acceleration phase. This results in higher early-age mechanical properties compared to the mixtures containing FA mixtures. The incorporation of 5% SF was shown to significantly accelerate the heat of hydration and enhance the heat peak. This is attributed to the relatively fine surface area of SF, which can provide additional surface sites for hydration products as well as enhance the pozzolanic reactivity, thus shortening the induction period and enhancing the nucleation density of C-S-H. Therefore, the ternary combination of FA with either SL or SF can lead to an acceleration of hydration reaction, thus enhancing the rate of mechanical properties development compared to the similar mixtures containing binary mixture of FA replacement.

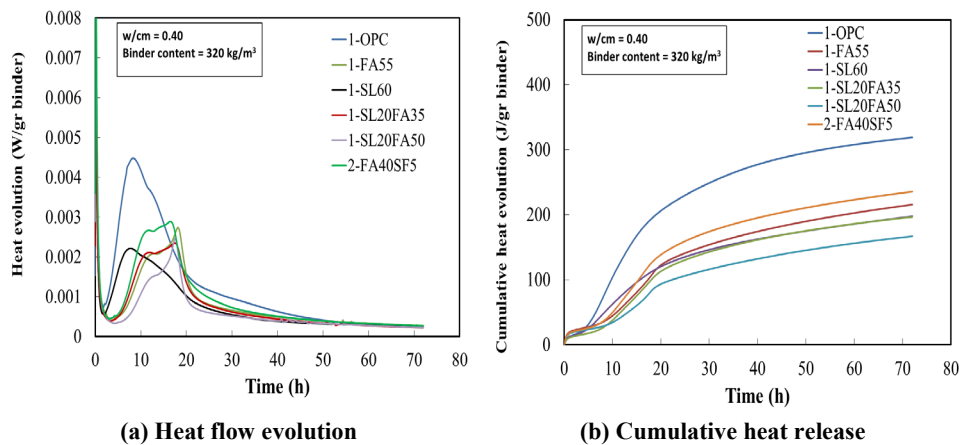


Figure 3.2. Effect of SCM substitutions on hydration heat evolution

3.1.3. Hardened characteristics

Figure 3.3 indicates the compressive strength development of the evaluated CEM mixtures made with different binder compositions. The compressive strengths at 3 and 91 days of the evaluated CEM mixtures ranged from 14 to 40 MPa (2.0 to 5.8 ksi) and 40 to 71 MPa (5.8 to 10.3 ksi), respectively. It is important that high early strength is not necessarily desirable for bridge deck construction given the high risk of cracking. As expected, the greatest early-age compressive strength of 40 MPa (5.8 ksi) at 3 days was observed for mortar made with 100% OPC followed by 27.5 MPa (3.4 ksi) for ternary binder composition containing 20% SL and 35% FA replacements. On the other hand, regardless of the binder content, all of the evaluated binder compositions exhibited approximately comparable long-term compressive strength to that of the control mixture, with the exception of the mortar made with 20% SL and 50% FA. The

SL20FA50 and FA40SF5 mixtures had the lowest and greatest strengths among the evaluated SCM combinations. Given higher reactivity, the incorporation of 5% SF combined with other cementitious materials was shown to be fully effective in developing compressive strength at 3 and 91 days. For example, the ternary mixture made with 40% FA in combination with 5% SF resulted in 17% and 20% higher compressive strength values at 3 and 91 days, respectively, compared to the similar mixture made with only 40% FA replacement.

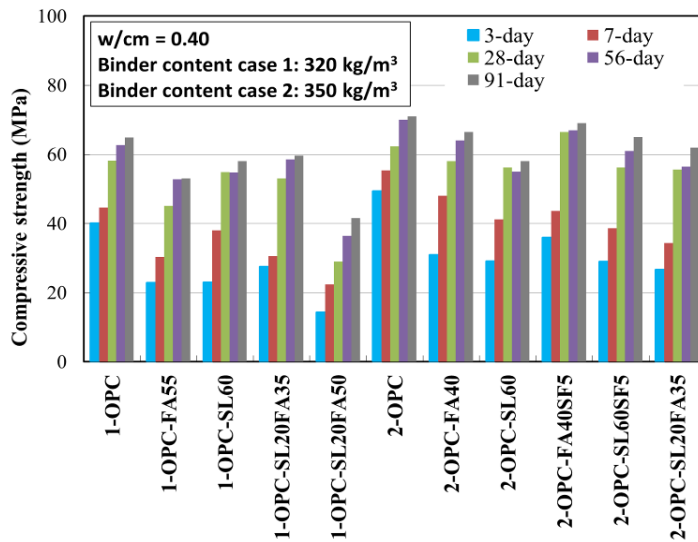


Figure 3.3. Effect of SCM substitutions on compressive strength development of mortars

The effect of SCM substitution on drying shrinkage of the mortar mixtures is presented in Figure 3.4. Regardless of the binder content, all binary and ternary blends of SCMs resulted in lower drying shrinkage compared to that of the control mixture made with 100% OPC. As expected, the increase in the binder content resulted in higher drying shrinkage, regardless of the binder compositions. The control mixtures with binder contents of 320 kg/m³ (20 lb/ft³) and 350 kg/m³ (22 lb/ft³) and containing 100% OPC exhibited the highest drying shrinkage values of 840 and 940 μ strain, respectively, after 150 days of drying, among the investigated binder compositions. Mixtures proportioned with SCMs exhibited drying shrinkage values ranging between 520-790 and 695-810 μ strain for binder contents of 320 kg/m³ (20 lb/ft³) and 350 kg/m³ (22 lb/ft³) after 150 days of drying. The mixture made with 320 kg/m³ containing 20% SL and 50% FA exhibited the lowest drying shrinkage value of 520 μ strain after 150 days of drying. Additionally, in the case of binder content of 350 kg/m³ (22 lb/ft³), the ternary blends of 40% FA and 5% SF was shown to have the lowest drying shrinkage of 695 μ strain after 150 days of drying. Therefore, the incorporation of Class C FA was shown to be quite beneficial in mitigating drying shrinkage. This can be attributed to the slower reactivity at early-age and pozzolanic reactivity at later ages, which can lead to a denser microstructure and reduce the capillary porosity.

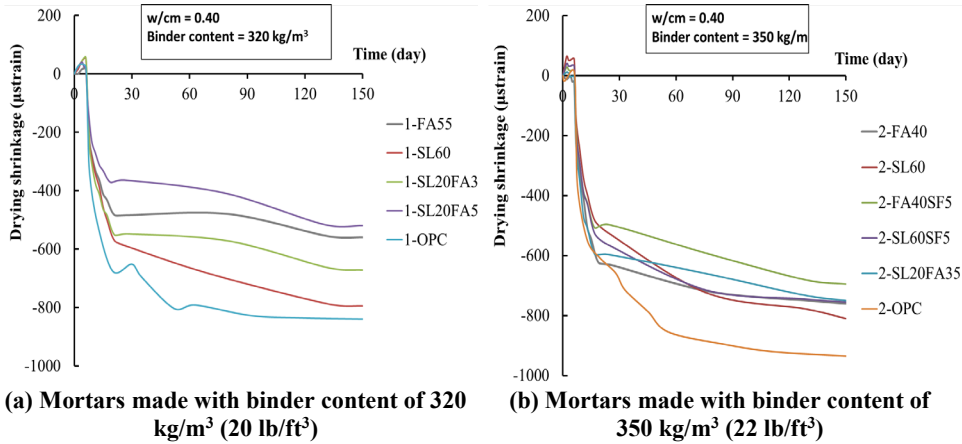


Figure 3.4. Drying shrinkage of mortars made with different SCM substitutions

3.1.4. Selection of optimum binder composition

In order to select the optimum binder compositions for construction applications defined in this investigation, the performance rank analysis was carried out. The selected test properties for the selection of optimum binder composition and the weighted factor assigned to each test property are presented in Tables 3.2 and 3.3 for Eco-Pave-Crete and Eco-Bridge-Crete, respectively.

Table 3.2. Selected test properties to optimize binder composition for Eco-Pave-Crete

Fresh properties (weighted factor)	Hardened properties (weighted factor)
HRWR demand (2)	Compressive strength at 3 days (1)
Initial plastic viscosity (1)	Compressive strength at 91 days (1)
Variation in plastic viscosity (1)	Drying shrinkage at 3 days of moist curing (1)
CO ₂ emission (2)	Drying shrinkage at 120 days of drying (2)

Table 3.3. Selected test properties to optimize binder composition for Eco-Bridge-Crete

Fresh properties (weighted factor)	Hardened properties (weighted factor)
HRWR demand (2)	Compressive strength at 3 days (1)
Initial plastic viscosity (1)	Compressive strength at 91 days (1)
Variation in plastic viscosity (1)	Drying shrinkage at 3 days of moist curing (1)
CO ₂ emission (2)	Drying shrinkage at 120 days of drying (2)
	Electrical resistivity at 91 days (2)

Based on the results from fresh and hardened characteristics of the investigated binders, all mixtures were ranked using performance rank analysis. The normalized response of the investigated mixtures for each property is calculated as follows:

$$\text{Normalized property (\%)} = \frac{R_{\max} - R_i}{R_{\max} - R_{\min}} \times 100 \quad (3.1)$$

where R_i is the test response of the investigated mixture, for a given property; and R_{\max} and R_{\min} are the maximum and minimum test response among the investigated mixtures for any particular property, respectively.

The normalized response ranges from 0 to 100%, corresponding to the least and best performing mixtures among the investigated systems. Figures 3.5 and 3.6 indicate the normalized ranking analysis of the investigated binders targeted for Eco-Pave-Crete and Eco-Bridge-Crete, respectively. For both types of binder optimization, the lowest performance was obtained for the control mixture made with 100% OPC. The ternary blend of 20% SL and 35% FA was shown to have desirable performance for both the pavement and transportation infrastructure applications. The ternary combination of 60% SL and 5% SF was considered to be the best binder among the investigated mixtures made with binder content of 350 kg/m³ (22 lb/ft³). Therefore, proper substitution of cement by SCMs can ensure greater packing density of solid particles, reduce water/admixture demand, and improve rheological and hardened properties of cement-based materials.

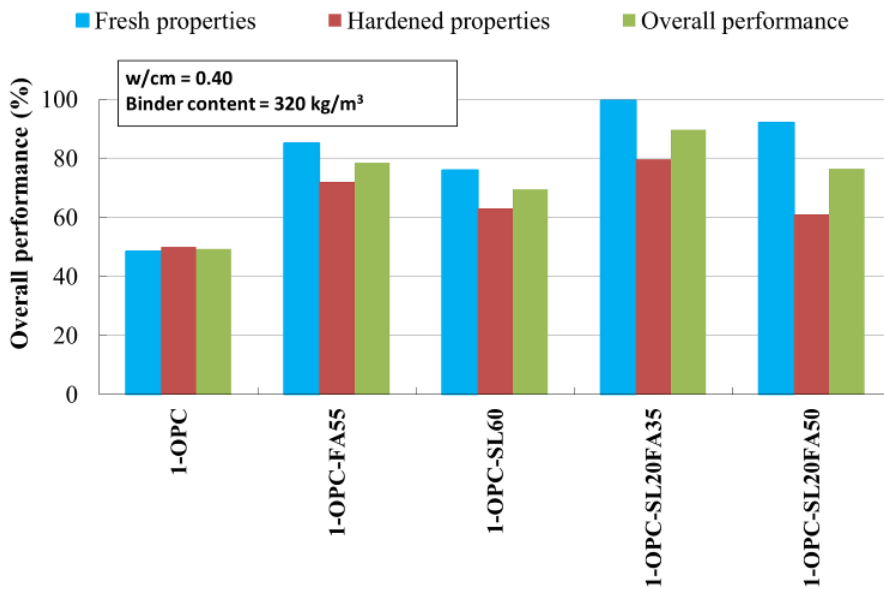


Figure 3.5. Overall performance of mortars made with 320 kg/m³ (20 lb/ft³) binder content

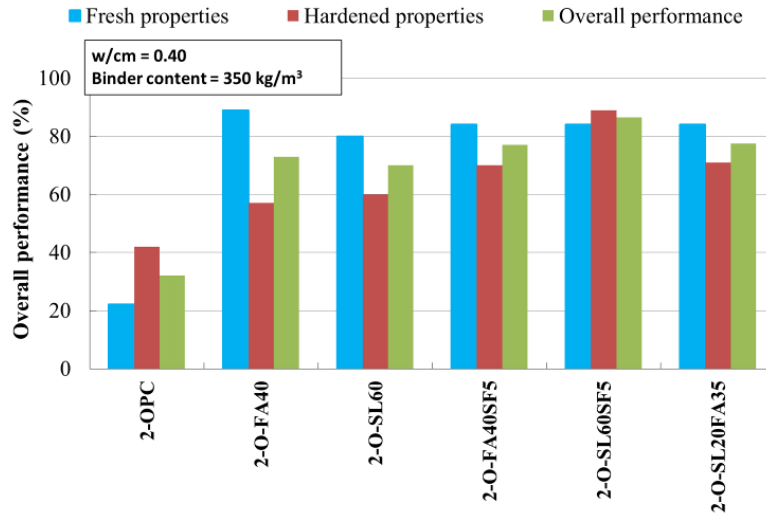


Figure 3.6. Overall performance of mortars made with 350 kg/m³ (22 lb/ft³) binder content

Based on the obtained results from fresh and hardened characteristics of the investigated binary and ternary binders in Subtask I, the selected optimum binder compositions for the Eco-Pave-Crete and Eco-Bridge-Crete applications are summarized in Table 3.4.

Table 3.4. Selected optimal binder compositions

Concrete type	Cementitious materials content	Codification	Replacement rate of cementitious materials (% by volume)			
			OPC	SL	CFA	SF
Reference	-	Ref	100	0	0	0
Eco-Pave-Crete	320 kg/m ³ (20 lb/ft ³)	1-FA40	60	0	40	0
		1-SL20FA35	45	20	35	0
Eco-Bridge-Crete	350 kg/m ³ (22 lb/ft ³)	2-SL60SF5	35	60	0	5
		2-SL20FA35	45	20	35	0

OPC: Ordinary portland cement, SL: Blast furnace slag, CFA: Class C fly ash, and SF: silica fume

3.2. Optimization of aggregate characteristics

The aim of this phase is to optimize the aggregate proportions to achieve the maximum possible packing density. In total, 17 different aggregate types (fine, intermediate, and coarse aggregates) were sampled to evaluate the effect of aggregate characteristics on packing density of the granular skeleton. The packing density of aggregate was measured using three different methods, including loose packing (ASTM C29), dense packing using rodding procedure (ASTM C29), and dense packing using ICT (combination of shear and compression stresses). The results of packing density of individual aggregate samples are presented in Table 3.5. The packing density

of mono aggregate is required for numerical modelling of packing density for various aggregate blends. Variations in packing density of mono aggregates are shown in Figure 3.7. The packing densities of aggregates are shown to vary with size, shape, surface texture, and angularity of aggregate. The packing densities of the investigated fine, intermediate, and coarse aggregates vary between 0.58-0.73, 0.6-0.73, and 0.57-0.61, respectively.

Table 3.5. Packing densities of investigated aggregates

	Name	Relative density	Bulk density (kg/m ³ , lb./ft ³)			Packing density		
			ICT	Loose	Rodding	ICT	Loose	Rodding
Fine Aggregate	Sand (Osage riv.) CapitCoInc	2510 (157)	1834 (114)	1677 (105)	1799 (112)	0.730	0.668	0.717
	Sand (Osage riv.- Manufactured) CapitCoInc	2480 (155)	1616 (101)	1454 (91)	1549 (97)	0.652	0.586	0.624
	River Sand, Missouri River	2517 (157)	1816 (113)	1729 (108)	1793 (112)	0.721	0.687	0.712
	APAC MFS, LinCreek	2582 (161)	1535 (96)	1353 (84)	1493 (93)	0.594	0.524	0.578
	APAC MFS, Tightwad	2606 (163)	1891 (118)	1670 (104)	1760 (110)	0.726	0.641	0.675
Intermediate Aggregate	Gravel (7/16 in.) CapitCoInc	2590 (162)	1660 (103)	1583 (99)	1652 (103)	0.641	0.611	0.638
	3/8 in. Clean CapitCoInc	2430 (151)	1485 (93)	1354 (85)	1471 (92)	0.611	0.557	0.605
	Gravel (5/16 in.) CapitCoInc	2590 (162)	1698 (106)	1604 (100)	1695 (106)	0.645	0.619	0.654
	1/2 in. Clean CapitCoInc	2430 (152)	1537 (96)	1415 (88)	1505 (94)	0.655	0.582	0.619
	3/8 in. Minus CapitCoInc	2450 (153)	1651 (103)	1546 (97)	1653 (103)	0.674	0.631	0.675
	1/2 in. (Captial Quar)	2462 (154)	1613 (101)	1452 (91)	1570 (98)	0.640	0.590	0.637
	3/8 in. (Captial Quar)	2450 (153)	1518 (95)	1362 (85)	1473 (92)	0.620	0.560	0.600
	Crushed Dolo (1/2 in.)	2730 (170)	1642 (103)	1502 (94)	1622 (101)	0.601	0.550	0.594
Coarse Aggregate	1 in. Clean CapitCoInc, Osage River	2450 (153)	1485 (93)	1426 (89)	1499 (94)	0.606	0.582	0.612
	1 in. (Captial Quar)	2572 (161)	1515 (95)	1464 (92)	1534 (96)	0.591	0.569	0.596
	1 in. Dolo Riverstone Quarry	2570 (160)	1500 (94)	1419 (89)	1531 (96)	0.583	0.552	0.596
	APAC 1 in., LinCreek	2689 (168)	1644 (102)	1471 (92)	1584 (99)	0.611	0.547	0.589

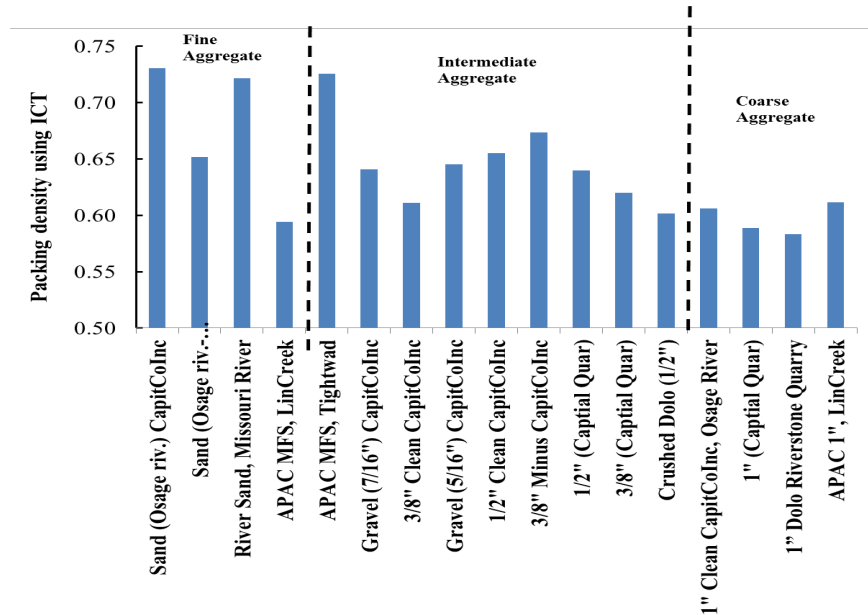


Figure 3.7. Variations in packing density of mono aggregates using ICT

3.2.1. Aggregate optimization using packing density approach

Packing density of binary aggregate blends

The experimental packing density study is initially focused on binary mixtures. As presented in Table 3.6, nine different binary mixtures were tested at different fine-to-total aggregate ratios (F/A) to determine the optimum combination of binary mixtures. For each set of aggregate blend, 7 to 12 different mixtures were tested to determine the packing density as a function of fine to coarse aggregate ratio.

The variations of packing density for different aggregate types and proportions are shown in Figure 3.8. Regardless of aggregate type, the packing density of blended aggregate increases with the increase in F/A up to a certain threshold value, beyond which the maximum packing density decreases with further increase in fine aggregate replacement. This decrease in packing density can be due to the loosening and wall effects, which can push the large particles away, thus resulting in lower packing density. For instance, for B1 blend proportioned with rounded fine and coarse aggregates, the increase in F/A from 0 to 50% resulted in an increase in the packing density from 0.61 to 0.78, while the use of 80% F/A reduced the packing density to 0.76. Therefore, there exists an optimum F/A corresponding to the maximum achievable packing density, which varies with aggregate types and combinations. Blends made with rough and angular aggregate need more content of fine particles to reach similar packing density as those of mixtures proportioned with smooth and rounded aggregate blends. This can be attributed to the higher internal friction between crushed particles which requires more fines to reduce the inter-

particle friction and achieve maximum packing density. Among the investigated binary blends, the B1, B3, and B5 blends exhibited packing density higher than 0.75.

Table 3.6. Packing density of binary aggregate blends

Blend	Aggregate 1	Aggregate 2	Φ_2/Φ_1	proportion corresponding to Φ_{max}	Φ_{max}
B1	River Sand, Missouri River	1 in. Clean CapitCoInc, Osage River	0.84	50% – 50%	0.79
B2	Gravel (5/16 in.) CapitCoInc	1 in. Clean CapitCoInc, Osage River	0.93	80% – 20%	0.608
B3	River Sand, Missouri River	1 in. Dolo Riverstone Quarry	0.88	60% – 40%	0.783
B4	3/8 in. Clean CapitCoInc	1 in. (Capital Quarry)	0.96	50% – 50%	0.642
B5	Sand (Osage riv.) CapitCoInc	1 in. (Capital Quarry)	0.81	60% – 40%	0.774
B6	APAC MFS, LinCreek	APAC 3/4 in., Marshall	0.98	50% – 50%	0.685
B7	Sand (Osage riv.- Manufactured)	Gravel (5/16 in.) CapitCoInc	1.00	50% – 50%	0.709
B8	Sand (Osage riv.- Manufactured)	APAC 3/4 in., Marshall	0.89	50% – 50%	0.740
B9	Sand (Osage riv.) CapitCoInc	3/8 in. Minus CapitCoInc	0.92	40% – 60%	0.714

Φ : packing density of aggregate

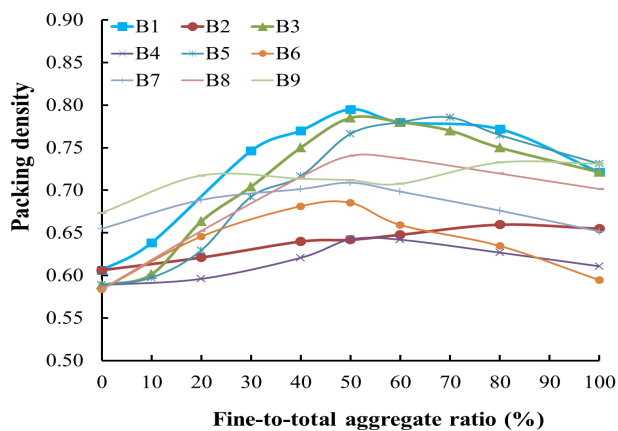


Figure 3.8. Variations in packing density for binary aggregate blends

Packing density of ternary aggregate blends

Based on the results of packing density determined for mono and binary aggregates, five ternary combinations of aggregate were selected. The investigated ternary aggregate blends are presented in Table 3.7. For each ternary combination, 15 to 25 different proportions were made by varying fine/intermediate/coarse aggregate proportions to cover a wide range of experimental domain.

Table 3.7. Packing density of ternary aggregate blends

Code	Type	Aggregate name	Packing density	Mix proportion (at Φ_{max})	Φ_{max}
TM1	Fine	River Sand, Missouri River	0.721	55%	0.803
	Inter.	3/8 in. Clean CapitCoInc	0.611	6%	
	Coarse	1 in. (Capital Quarry)	0.589	39%	
TM2	Fine	River Sand, Missouri River	0.721	40%	0.815
	Inter.	Gravel (5/16 in.) CapitCoInc	0.655	20%	
	Coarse	1 in. Clean CapitCoInc, Osage	0.606	40%	
TM3	Fine	River Sand, Missouri River	0.721	56%	0.787
	Inter.	1/2 in. Clean CapitCoInc	0.632	15%	
	Coarse	APAC 3/4 in., Marshall	0.583	29%	
TM4	Fine	River Sand, Missouri River	0.721	40%	0.808
	Inter.	3/8 in. Minus CapitCoInc	0.674	25%	
	Coarse	1 in. Dolo Riverstone Quarry	0.58	35%	
TM5	Fine	APAC MFS, Tightwad	0.674	56%	0.780
	Inter.	1/2 in. (Capital Quarry)	0.64	0%	
	Coarse	APAC 1 in., LinCreek	0.611	44%	

A ternary packing diagram (TPD) was developed based on the packing density of measured and interpolated data points, as shown in Figure 3.9. Given different aggregate blends and proportions, packing density varied from 0.63 to 0.82. The maximum packing density obtained for each ternary aggregate blend and its corresponding proportion are given in Table 3.7. The maximum packing density of rounded and crushed aggregates were 0.815 and 0.809, respectively. In general, smooth and rounded blends exhibited higher packing density compared to the crushed and rough aggregate combinations. In the case of rounded aggregates, the difference between minimum and maximum packing density is 0.21, which should be filled with the paste. Therefore, there exists an optimum value of aggregate proportions, corresponding to maximum packing density, which can significantly reduce the void volume between particles, thus lowering the paste volume required to fill the voids between the granular skeleton. This is an essential step and key parameter in the design and mixture proportioning of Eco-Crete. The packing density contours in Figure 3.9 indicates that higher packing density of blended aggregate was obtained with low volume of medium aggregate, regardless of the aggregate types. In other words, coarse and fine aggregates play a more dominant role in the increase of packing density.

The highest packing density (more than 0.80) values were obtained for the blends TM2 and TM4 (Result of TM4 is shown in Figure B.1 in Appendix B).

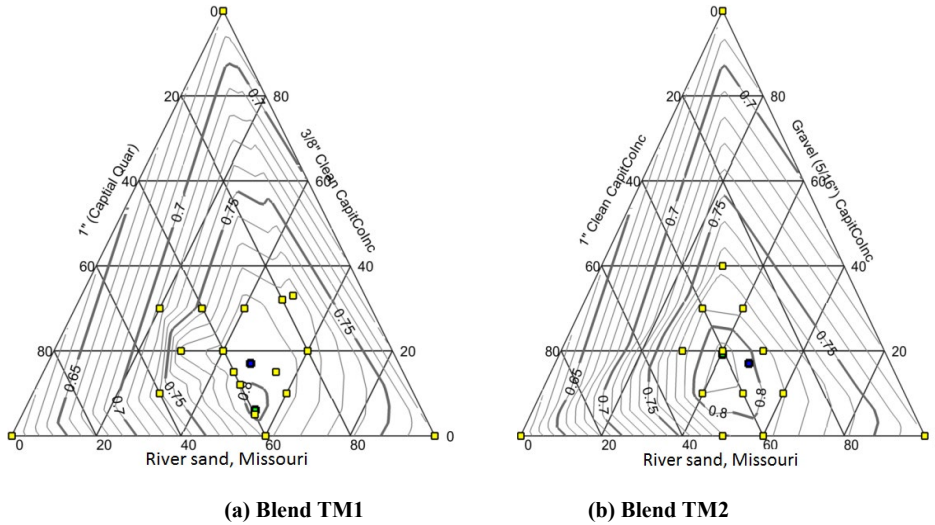


Figure 3.9. Ternary Packing diagram of various aggregate blends measured by ICT

3.2.2. Optimization of aggregate proportioning using SMD method

The aim of using SMD technique was to determine the optimum aggregate proportioning to achieve maximum possible packing density as well as derive the statistical model to estimate the packing density of the blended aggregate. This phase was carried out on the TM4 blend that was one of the optimal aggregate combinations among the investigated aggregate blends in the previous section. In order to cover a wide range of experimental domain, the packing density of 20 different aggregate proportions were experimentally measured using ICT. The red points in Figures B.2 and B.3 in Appendix B refer to experimentally measured data points. The significance of variables and their interactions was determined by the analysis of variance (ANOVA) using the least squares fitting technique. Statistical models presented in this study were established by multi-regression analysis, as follows:

$$Y = \beta_0 + \sum_{i=1}^n \beta_i X_i + \sum_{i < j}^n \sum_j^n \beta_{ij} X_i X_j \quad (3.2)$$

where Y is the predicted response, X_i and X_j are the coded values of the modeled variables, β_i is linear coefficient, β_{ij} is the coefficient of the interaction, and n is the number of the modeled parameters.

The contour diagram and surface response of the packing density for the ternary aggregate blend are presented in Figures B.2 and B.3 in Appendix B, respectively. Depending on the aggregate proportions, the packing density values varied from 0.60 to 0.80. The packing density of blended

aggregate is shown to increase with incorporating fine aggregate to a maximum possible packing density, thereafter the packing density of blended aggregate decreased with further fine particles addition.

The derived statistical model to estimate the packing density is expressed as follows:

$$\begin{aligned}
 \text{Packing density} = & \\
 & + 0.71 * \text{Fine Agg.} \\
 & + 0.45 * \text{Intermediate Agg.} \\
 & + 0.62 * \text{Coarse Agg.} \\
 & - 0.14 * \text{Fine Agg.} * \text{Intermediate Agg.} \\
 & + 0.42 * \text{Fine Agg.} * \text{Coarse Agg.} \\
 & + 0.12 * \text{Intermediate Agg.} * \text{Coarse Agg.}
 \end{aligned} \tag{3.3}$$

The correlation coefficient (R^2) of the derived model is about 0.95. As indicated in Eq. (3.3), the fine aggregate has a higher significant effect on the packing density of the blended aggregated compared to other constituents.

A multi-objective optimization technique was carried out to determine the optimum combination of aggregate blends required to achieve maximum packing density. This technique involves satisfying the defined properties without compromising any of the requirements (Montgomery, 2005). For the targeted properties, the desirability functions (d_i) are obtained and these functions are simultaneously optimized to determine the best combination. The overall desirability function (D) proposed by Derringer and Suich (1980) is expressed as follows:

$$D = (d_1^{r_1} \times d_2^{r_2} \times d_3^{r_3} \times \dots \times d_n^{r_n})^{1/\sum r_i} = \left(\prod_{i=1}^n d_i^{r_i} \right)^{1/\sum r_i} \tag{3.4}$$

where n is the number of individual responses in the optimization, and r_i refers to the relative importance of each individual property. The r_i varies from 1 to 5, reflecting the least to most important, respectively. The d_i ranges between 0 (for a completely undesired response) and 1 (for a fully desired response). The D value close to 1 reflects that the optimal combination of variables is able to secure the target properties. The contour diagram of overall desirability for target property (maximum possible packing density) is shown in Figure B.4 in Appendix B. The highest desirability value of 0.96 was achieved for the aggregate combination of 43% fine aggregate (River Sand, Missouri River), 22% intermediate aggregate (3/8 in. Minus CapitCoInc), and 35% coarse aggregate (1 in. Dolo Riverstone Quarry) that resulted in packing density of 0.801.

Based on the derived statistical model, the optimum proportioning for the investigated aggregate blend, corresponding to maximum packing density, is presented in Table 3.8. The optimal aggregate proportioning determined from the SMD method is consistent with those determined from experimentally measured packing density.

Table 3.8. Optimum aggregate proportions using SMD method

Type	Aggregate name	Proportion	Max. packing density
Fine aggregate	River Sand, Missouri River	40%	0.808
Intermediate aggregate	3/8 in. Minus CapitCoInc	25%	
Coarse aggregate	1 in. Dolo Riverstone Quarry	35%	

The PSD of the selected aggregate combination is plotted in Figure 3.10. The selected aggregate blend had a packing density of 0.808 and its PSD is close to Andreasen model with a q value of 0.275.

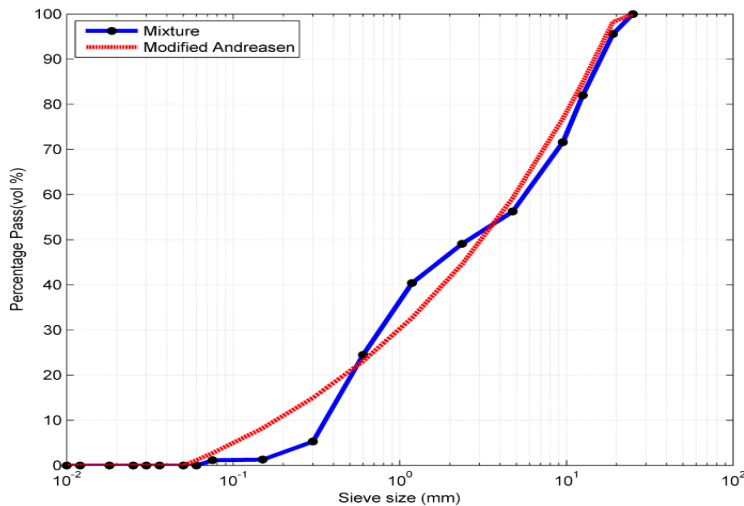


Figure 3.10. PSD of selected aggregate blend

3.2.3. Comparison of shrinkage mitigating strategies

This subtask focused on evaluating the effect of different shrinkage reducing/compensating materials on autogenous and drying shrinkage and mechanical properties of concrete equivalent mortars (CEMs) proportioned with optimized binder compositions determined from Subtask I. The investigated shrinkage mitigating materials included expansive agents (CaO-based and MgO-based), crack reducing admixture (CRA), and lightweight sand (LWS) with various particle size distributions. The use of lightweight aggregate has the significant benefit of providing internal curing and enhanced cement hydration along with forming new hydration products via pozzolanic reaction of the SCMs. Based on the obtained results from fresh and hardened properties of investigated binders in Subtask I, the selected binder compositions for Eco-Pave-Crete and Eco-Bridge-Crete applications are summarized in Table 3.9. In total, 18

CEMs made with different binder compositions and shrinkage reducing/compensating materials were evaluated, as given in Table 3.10. The w/cm of the investigated mixtures remained constant at 0.40. The EX and CRA contents were considered as a part of cementitious materials and mixing water, respectively. Depending on the concrete type, the binder content of the evaluated mortars varied between 320 and 350 kg/m³ (20 and 22 lb/ft³), as presented in Table 3.9. Given different target slump consistencies aimed for different construction applications, the HRWR concentrations were adjusted to secure the mini-slump flow of 135 ± 10 mm (5.3 ± 0.4 in.) and 190 ± 10 mm (7.5 ± 0.4 in.) in the mortar fraction of Eco-Pave-Crete and Eco-Bridge-Crete, respectively. The investigated mixtures were subjected to different durations of initial moist curing of 0, 3, and 7 days to examine the influence of initial moist curing period (IMCP) on shrinkage and compressive strength development.

Table 3.9. Selected optimum binders targeted for Eco-Pave-Crete and Eco-Bridge-Crete

Concrete type	Cementitious materials content (kg/m ³ , lb/ft ³)	Codification	Replacement rate of cementitious materials			
			OPC	SL	CFA	SF
Reference		Ref	100	0	0	0
Eco-Pave-Crete	320 (20)	1-FA55	45	0	55	0
		1-SL20FA35	45	20	35	0
Eco-Bridge-Crete	350 (22)	2-SL60SF5	35	60	0	5
		2-SLA20FA35	45	20	35	0

OPC: Ordinary portland cement, SL: Blast furnace slag, CFA: Class C fly ash, and SF: silica fume

The quantity of LWS was theoretically estimated based on the internal curing water required to eliminate the self-desiccation proposed by Bentz et al. (2005). This can be expressed as follows:

$$M_{LWS} = \frac{C_f \times CS \times \alpha_{max}}{S \times W_{LWS}} \quad (3.5)$$

where M_{LWS} and C_f refer to the dry mass of LWS (kg/m³) and binder content (kg/m³), respectively, CS is the chemical shrinkage of the binder (kg of water per kg of binder), and α_{max} is the maximum potential degree of hydration of binder varying from 0 to 1. The S value represents the degree of saturation of the LWS, and M_{LWS} is the mass of internal curing water released by LWS. In this study, CS and α_{max} values were considered to be 0.07 and 1, respectively (Bentz et al., 2005). The partial replacement of sand by 25% LWS, corresponding to M_{LWS} of 185 kg/m³, can provide internal curing water of 24 kg/m³.

Table 3.10. Mixture design parameters investigated for shrinkage mitigating strategies

Codification	Description	Binder type				Lightweight sand (LWS)	Expansive agent (EX)		Crack reducing admixture (CRA)
		Ref	Pavement	Bridge deck			7.5% CaO-based system	5% MgO-based system	
		100% OPC	45% OPC + 55% Class C FA	35% OPC + 60% SL + 5% SF	45% OPC + 20% SL + 35% Class C FA				
OPC	Effect of binder composition	x							
FA55			x						
SL60SF5				x					
SL20FA35					x				
E-OPC	Effect of CaO-based EX	x					x		
E-SL60SF5			x				x		
E-FA55				x				x	
E-SL20FA35					x			x	
P-OPC	Effect of MgO-based EX	x						x	
P-SL60SF5			x					x	
P-FA55				x				x	
P-SL20FA35					x			x	
E-L-OPC	Combined effect of LWS 1 and EX	x				x	x		
E-L-SL60SF5			x			x	x		
E-L-SL20FA35				x		x	x		
E-L-FA55					x	x	x		
C-OPC	Effect of CRA	x						x	
E-L2-OPC	Effect of LWS type	x				x	x		

Codification: E-L-OPC = 7.5% CaO-based EX + 25% lightweight sand type 1.

3.2.4. Autogenous shrinkage

The variations in autogenous shrinkage of mortars made with different shrinkage mitigating materials and binder compositions are shown in Figure 3.11. As outlined in ASTM C1698, time zero or starting point for autogenous shrinkage measurement was set at the final set of the investigated mixtures. All mixtures made with shrinkage mitigating materials exhibited lower autogenous shrinkage compared to $-350 \mu\text{strain}$ for control mixture after 150 days.

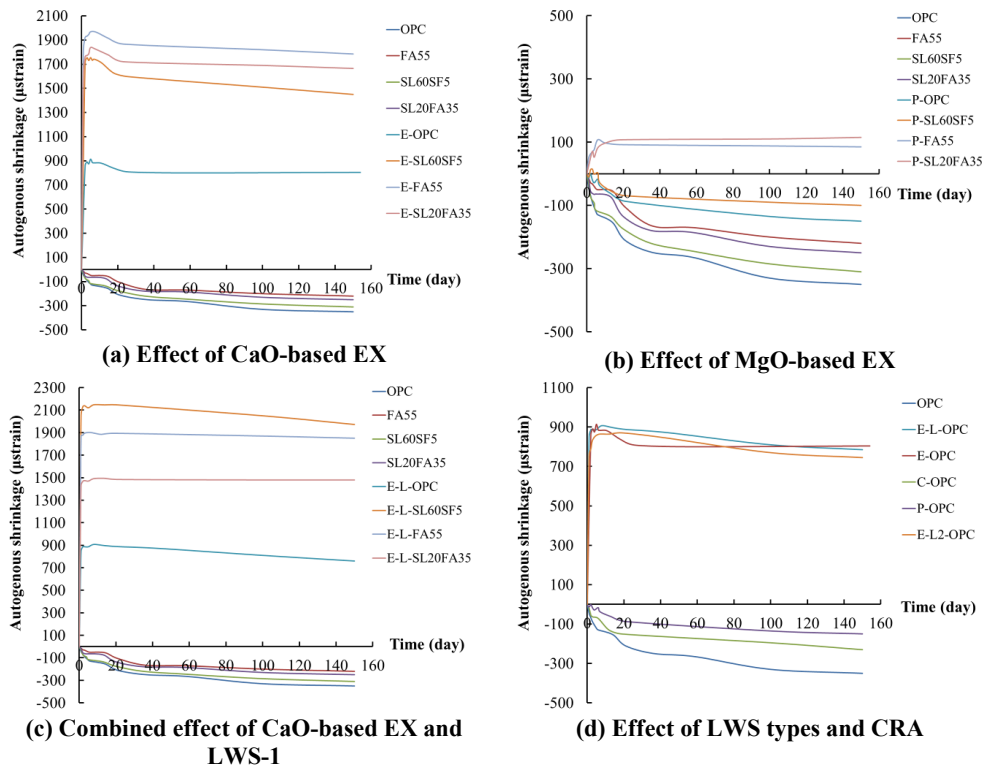


Figure 3.11. Autogenous shrinkage of mortars made with various binder compositions and shrinkage mitigating materials

Regardless of the binder composition, the incorporation of expansive agent led to a significant expansion, especially in the case of the CaO-based EX system. The expansion provided by EX was more pronounced for mixtures containing high volume SCMs. This can be due to the lower resistance of such mixtures to expansion, resulting in larger free movement. The highest expansion of 1780 μ strain was observed for the mixture made with 55% FA replacement and 7.5% CaO-based EX. The magnitude, rate, and duration of expansion were influenced by the EX type, as shown in Figure 3.11. Mixtures incorporating 7.5% CaO-based EX exhibited substantially higher magnitude and rate of expansion for a longer duration compared to the 5% MgO-based EX. The use of CRA was shown to be effective in reducing the autogenous shrinkage. The incorporation of 2% CRA concentration resulted in an autogenous shrinkage of 230 μ strain compared to 350 μ strain for control mixture after 150 days. The synergistic effect between EX with LWS resulted in lower autogenous shrinkage or higher expansion magnitudes for a longer duration. The highest expansion of 1980 μ strain was found for the E-L-SL60SF5 mixture with binary system of shrinkage mitigating materials including 7.5% CaO-based EX and 25% LWS replacement. This is attributed to the couple effect of lower self-desiccation and larger

expansion resulting from the use of LWS along with EX systems. The internal relative humidity (RH) of the prismatic samples was measured under sealed conditions using cast-in sensors. The sequence of casting and measurement procedure consists of casting the CEM in a prism measuring $75 \times 75 \times 285$ mm ($2.95 \times 2.95 \times 11.22$ in.) followed by inserting two hollow PVC tubes with diameters of 20 mm and embedment depth of 40 mm into the fresh mixture. Following final set, the sensors are embedded at the bottom of PVC tubes in contact with the CEM surface. The RH is measured by inserting a probe into the PVC tube after contact with the embedded sensors. The specimen was wrapped using two layers of adhesive aluminum sheet to prevent any moisture loss due to external drying. Figure 3.12 shows the effect of using LWS replacement on RH of CEMs. The mixture made with 25% LWS replacement had 18% higher RH after 10 days compared to the control mixture. The higher degree of saturation extends the wet curing period, which can reduce the capillary stresses induced by self-desiccation. Therefore, the higher degree of saturation of cement resulting from the use of LWS can enhance the magnitude and duration of expansion provided by the use of EX.

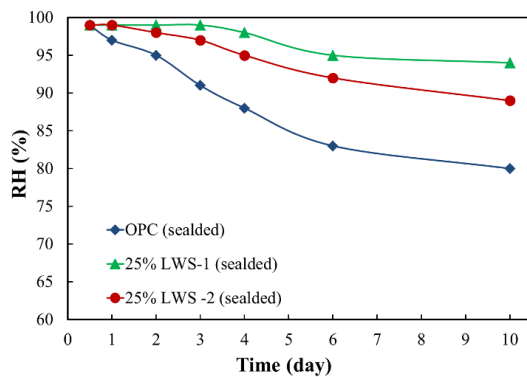
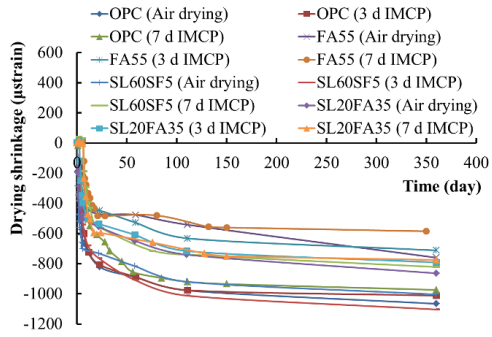


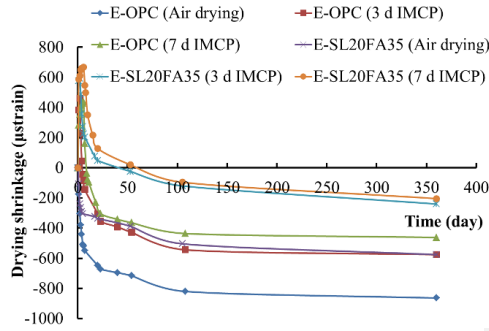
Figure 3.12. Effect of using LWS on RH of mortars over time

3.2.5. Drying shrinkage

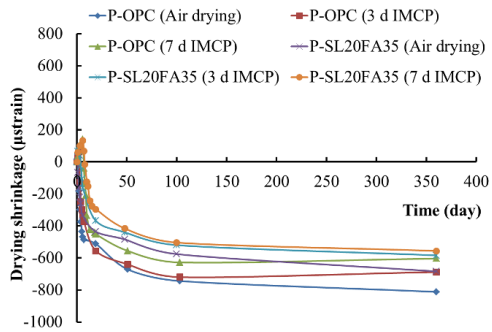
Figure 3.13 shows the drying shrinkage of mortars made with different shrinkage mitigating materials and initial moist curing durations. Regardless of initial moist curing period, all mixtures containing shrinkage mitigating materials exhibited lower drying shrinkage than the control mixture made with 100% OPC. For a given IMCP, mixtures proportioned with CaO-based EX exhibited larger expansion values compared to the similar mixtures made with 5% MgO-based EX. It is important to note that effectiveness of incorporating shrinkage mitigating materials to control shrinkage was shown to be significantly affected by the IMCP, especially for EX systems. As shown in Figure 3.13 (b) and (c), in the absence of IMCP, mixtures made with 7.5% EX or 5% MgO-based EX systems resulted in no expansion. However, in the presence of 6 days of IMCP, the EX1 mixture resulted in an expansion of $450 \mu\text{strain}$ after 6 days followed by a shrinkage of $460 \mu\text{strain}$ after 360 days compared to $865 \mu\text{strain}$ for a similar mixture when no IMCP was applied. Therefore, for EX systems, an initial moist curing should be applied to develop its potential expansion and consequently lower drying shrinkage.



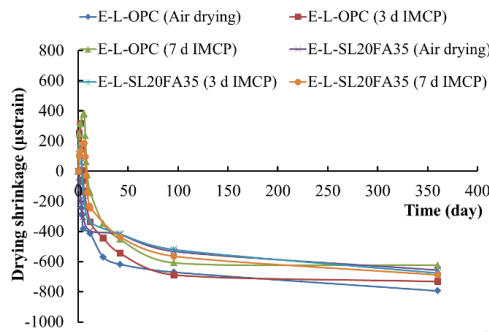
(a) Effect of binder compositions



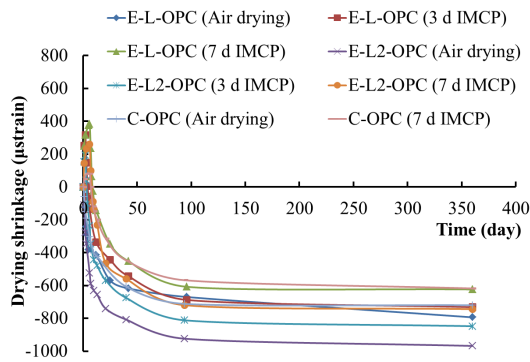
(b) Effect of CaO-based EX



(c) Effect of MgO-based EX



(d) Combined effect of CaO-based EX and LWS-1



(e) Effect of LWS types and CRA

Figure 3.13. Drying shrinkage of mortars made with various binder compositions and shrinkage mitigating materials as a function of IMCP

As in the case of autogenous shrinkage, the incorporation of EX for a mixture made with a SCM replacement resulted in larger expansion and lower drying shrinkage compared to the similar mixture containing 100% OPC. In other words, for a given IMCP, mixtures made with SCM replacement resulted in higher expansion when combined with EX. For example, in the case of 6 days of IMCP, the E-SL20FA35 mixture exhibited an expansion of 670 μ strain compared to the 450 μ strain for similar mixture containing OPC and 7.5% CaO-based EX. The duration of initial moist curing period was shown to have higher impact on shrinkage reduction than LWS replacement. In other words, moist cured mixtures exhibit lower drying shrinkage compared to the use of 25% LWS without moist curing. Unlike the autogenous shrinkage trend, the combined use of EX and LWS resulted in lower expansion magnitude along with shorter expansion duration. Comparison between the two investigated LWSs in Figure 3.13 (e) indicates that the use of LWS-1 is more efficient to reduce the drying shrinkage. This is attributed to the larger desorption capacity of this aggregate which can provide more internal water, thus resulting in lower shrinkage.

3.3. Development of Eco and crack-free HPC

This subtask was undertaken to optimize the mixture design and evaluate the performance of Eco and crack-free HPC. Based on the obtained results from Subtasks 2-1, 2-2, and 2-3, the effect of different binder compositions, aggregate characteristics, and shrinkage mitigating materials were incorporated to design Eco- and crack-free HPC with different targeted applications (Eco-Pave-Crete and Eco-Bridge-Crete). The mix design parameters are summarized in Tables 3.11 and 3.12 present the mixture proportions of the investigated Eco- and crack-free mixtures. The binder contents were 320 and 350 kg/m^3 (20 and 22 lb/ft^3) for pavement and transportation infrastructure applications, respectively. The OPC reference mixture was made with 100% cement and binder content of 350 kg/m^3 . The mix design parameters included four different binder compositions, two types of fibers, and two various shrinkage mitigating materials. Depending on the targeted application, the HRWR dosage was adjusted to secure the slump consistencies varying between 50 mm and 200 mm. The AEA concentration was also adjusted to ensure the fresh air volume of $5\% \pm 2\%$ for all mixtures. The w/cm was fixed at 0.40 for all mixtures. The test properties included workability, shrinkage, mechanical properties, and durability.

Table 3.11. Investigated mixture design parameters in Subtask 2-4

Codification	Description	Binder content		Binder type				Fiber type and content			Shrinkage mitigating strategy	
		320 (kg/m ³)	350 (kg/m ³)	100% OPC	60% OPC + 40% Class C FA	45% OPC + 20% SL + 35% Class C FA	35% OPC + 60% SL + 5% SF	TUF strand fiber (0.35%)	STRUX® 90/40 synthetic fiber (0.35%)	Recycled steel fiber from tire fiber (0.35%)	25% LWS	7.5% CaO-based EX
350-OPC	Reference mixture		x	x								
320-20SL-35FA	Effect of binder type	x				x						
350-20SL-35FA			x			x						
320-40FA			x			x						
350-60SL-5SF				x				x				
350-20SL-35FA-25LWS	Effect of LWS		x			x					x	
320-40FA-25LWS		x			x						x	
350-60SL-5SF-25LWS			x					x				x
350-20SL-35FA-0.35FT	Effect of fiber type		x			x		x				
350-20SL-35FA-0.35FG			x			x			x			
350-20SL-35FA-0.35FRW			x				x			x		
350-20SL-35FA-7.5EX	Effect of EX		x			x						x
350-20SL-35FA-7.5EX-0.35FT	Combined effect of fiber and EX		x			x		x				x
350-20SL-35FA-7.5EX-0.35FRW			x				x			x		x

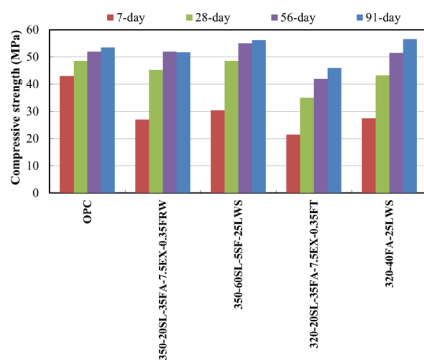
OPC: Ordinary portland cement, SL: Blast furnace slag, CFA: Class C fly ash, and SF: silica fume, EX: expansive agent, LWS: lightweight sand
 Codification: 350-20SL-35FA-7.5EX-0.35FRW: Binder content of 350 kg/m³ containing 20% SL, 35% FA and 7.5% CaO-based EX and 35% recycled steel fibers

Table 3.12. Mixture proportions of Eco and crack-free HPC mixtures

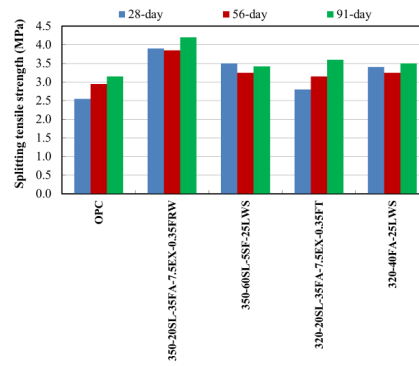
	350- OPC	320- 20SL- 35FA	350- 20SL- 35FA	320- 40FA	350- 60SL- 5SF	320- 40FA- 25LWS	350- 20SL- 35FA- 25LWS	350- 60SL- 5SF- 25LWS	350- 20SL- 35FA- 0.35FT	350- 20SL- 35FA- 0.35FG	350- 20SL- 35FA- 0.35FRW	350- 20SL- 35FA- 7.5EX	350-20SL- 35FA- 7.5EX- 0.35FT	350-20SL- 35FA- 7.5EX- 0.35FRW
Cement (kg/m ³)	350	144	158	192	158	192	158	158	158	158	158	145	158	158
Fly ash (kg/m ³)	—	97	106	111	—	111	106	—	106	106	106	98	106	106
Slag (kg/m ³)	—	60	64	—	192	—	64	192	64	64	64	60	64	64
Silica fume (kg/m ³)	—	—	—	—	13	—	—	13	—	—	—	—	—	—
Water (kg/m ³)	140	128	140	128	140	128	140	140	140	140	140	140	140	140
Sand (kg/m ³)	744	761	744	761	744	570	560	560	744	744	744	560	744	744
Agg. 3/8 in. (kg/m ³)	465	475	465	475	465	476	465	465	555	555	650	465	555	650
Agg. 1 in. (kg/m ³)	650	666	650	666	650	666	650	650	565	565	480	650	565	480
LWS (kg/m ³)	—	—	—	—	—	190	186	186	—	—	—	—	—	—
CaO-based EX (kg/m ³)	—	—	—	—	—	—	—	—	—	—	—	23	23	23
Fiber, by volume (type)	—	—	—	—	—	—	—	—	0.35 (synthetic)	0.35 (synthetic)	0.35 (steel fibers)	—	0.35 (synthetic)	0.35 (steel fibers)
HRWRA (l/kg ³)	1.12	0.45	0.89	0.9	1.05	1.1	1.05	1.25	1.05	1.2	1.2	0.9	1.1	1.4
AEA (ml/kg ³)	28	26	28	16	17	17	14	17	20	20	14	15	15	15

3.3.1. Mechanical properties

The development of mechanical properties of the selected Eco-HPCs is presented in Figure 3.14. The mixture made with 0.35% recycled fibers and containing 20% slag and 35% fly ash replacements developed approximately similar compressive strength as that of the control mixture made with 100% cement. The incorporation of fibers in concrete made with high volume of SCMs is shown to have 30% higher splitting tensile strength than that of the control mixture made with 100% cement. The mixture made with 0.35% recycled steel fibers developed the greater area under load-deflection curve compared to other mixtures proportioned with synthetic fiber. The reference mixture developed the lowest ductility behavior and residual strength among all mixtures. The 56 day flexural toughness (area under the load-deflection curve) results of mixtures made with fibers are compared in Figure 3.14 (e). It is interesting to note that for a given fiber content, the use of steel fibers recovered from waste tires had two times higher flexural toughness compared to the similar mixture made with synthetic fibers. In addition, the incorporation of expansive agent in combination with fibers (especially steel fibers) would enhance the reinforcing mechanism provided by fibers. This may be due to the induced compressive stress provided by expansive cements which can lead to forming of internal pre-stressed condition in concrete. Internal pre-stressed concrete may result in higher residual strength and flexural toughness. Bentz and Jensen (2004) also reported that as long as proper restraint is provided, the expansion of self-stressing materials can pre-stress concrete and improve its tensile capacity.



(a) Compressive strength



(b) Splitting tensile strength

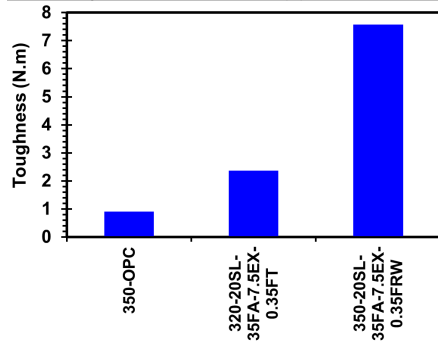
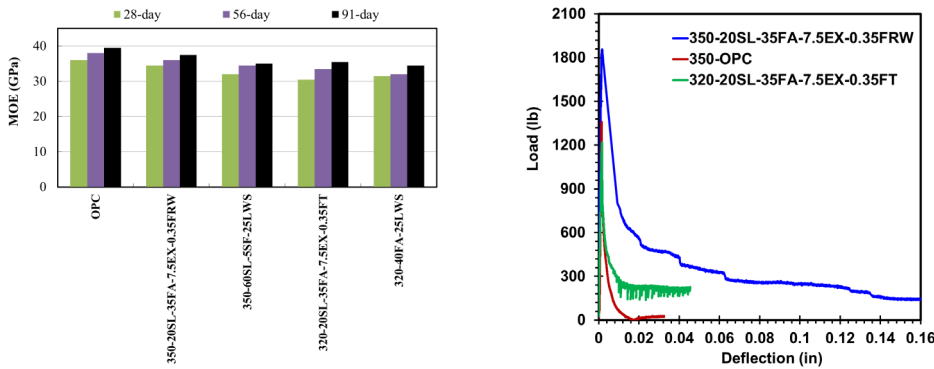


Figure 3.14. Mechanical properties of selected HPC mixtures

3.3.2. Shrinkage

The results of drying and restrained shrinkage of the selected mixtures are shown in Figure 3.15. Restrained shrinkage and cracking potential of mixtures were evaluated using ASTM C1581 ring test. Mixture made with 100% cement exhibited the highest drying shrinkages of 550 μ strain after 250 days of drying. The optimized Eco-HPC mixtures had lower drying shrinkage of 300 μ strain after 250 days of drying. The incorporation of 7.5% Type G expansive agent resulted in a significant early-age expansion of 100 μ strain. It is interesting to point out that no restrained shrinkage cracking was observed for the optimized concrete mixtures after 55 days of testing. However, the control mixture made with 100% cement exhibited elapsed time to cracking after 22 days. For mixtures containing EX, the tensile stress induced by restrained shrinkage was compensated by expansion induced by using EX, thus reflecting no cracking after 55 days. Average stress rate and cracking potential classification of investigated mixtures are summarized in Table 3.13. In accordance with ASTM C1581, the stress rate development induced by restrained shrinkage at the age of cracking can be calculated as follows:

$$q = \frac{G|\alpha_{avg}|}{2\sqrt{t_r}} \quad (3.6)$$

where q is the stress rate in each test specimen, MPa/day, G is a constant based on the ring dimension 72.2 GPa, and t_r is the elapsed time to cracking or elapsed time when the test is terminated for each test specimen. $|\alpha_{avg}|$ is the absolute value of the average strain rate factor for each test specimen, ($\mu\text{strain/day}^{1/2}$) which is determined as a slope of a fitted line between steel strain and square root of elapsed time.

Mixtures made with EX had positive strain rate factor due to the expansion of such mixtures. In accordance with ASTM C1581, the reference mixture made with 100% cement was considered to exhibit moderate shrinkage cracking potential. On the other hand, mixtures proportioned with shrinkage reducing materials have low cracking potential with compressive stress rate ranging between -6.9 to 1.7 MPa/day.

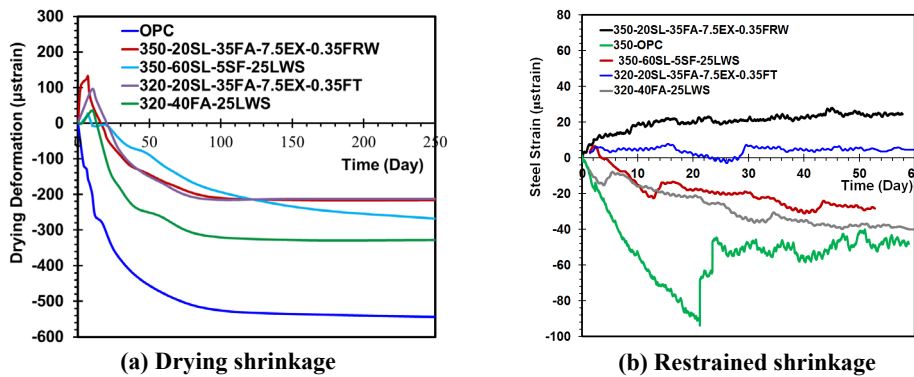


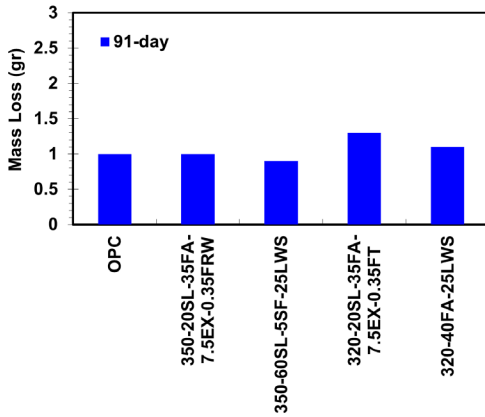
Figure 3.15. Shrinkage of selected HPC mixtures

Table 3.13. Cracking potential classification of HPC mixtures

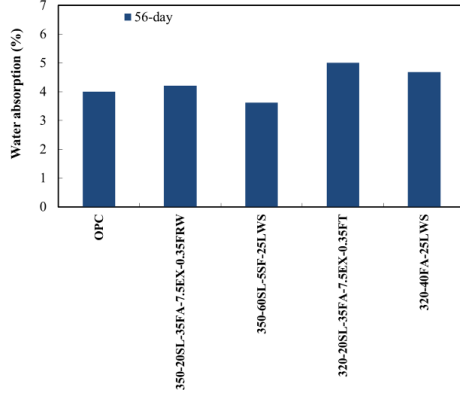
Mixture	Time to cracking (day)	Average strain rate factor ($\mu\text{strain/day}^{1/2}$)	Average stress rate (MPa/day)	Potential of cracking (ASTM C 1581)
350-OPC	22	-23.6	-26.4 (tension)	Moderate
350-20SL-35FA-7.5EX-0.35FRW	—	2.4	1.7 (compression)	Low
350-60SL-5SF-25LWS	—	-4.9	-3.5 (tension)	Low
320-20SL-35FA-7.5EX-0.35FT	—	1.3	1 (compression)	Low
320-40FA-25LWS	—	-9.7	-6.9 (tension)	Low

3.3.3. Durability

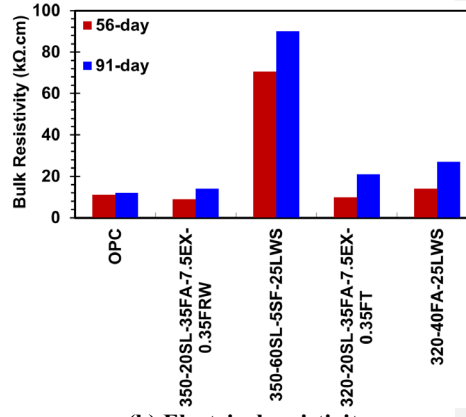
The performance of the selected Eco-HPCs for different durability aspects is presented in Figure 3.16. All selected Eco-HPC mixtures was moist cured for 56 d, as described in Section 2.4.2. All mixtures developed approximately similar performance as that of the control mixture made with 100% OPC. All Eco-HPCs developed frost durability factor values higher than 80% after 300 freeze-thaw cycles, except for ternary blends of 60% SL and 5% SF with durability factor of 70%.



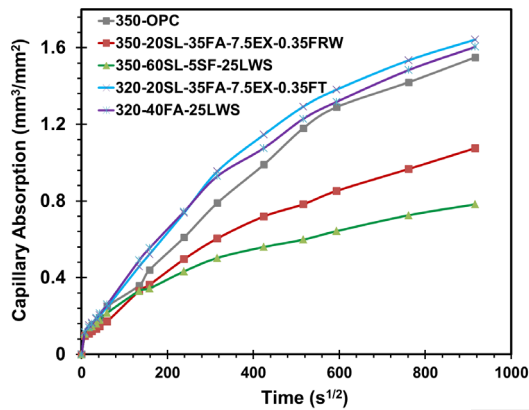
(a) Abrasion resistance



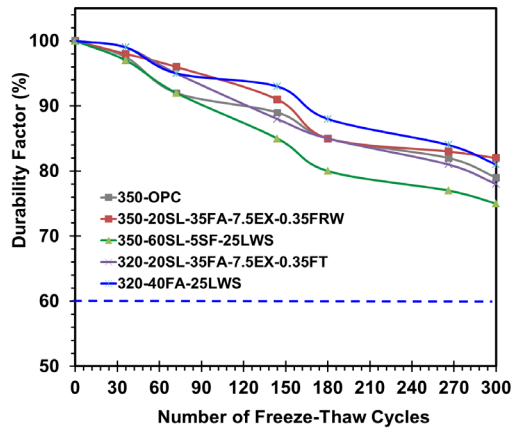
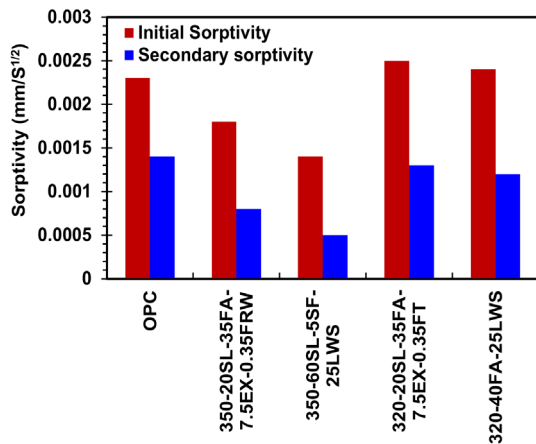
(c) Water absorption



(b) Electrical resistivity



(d) Capillary absorption



(e) Sorptivity index

(f) Frost durability factor

Figure 3.16. Durability performance of selected HPC mixtures

The results of deicing salt scaling rating and cumulative mass of scaling residue of the investigated mixtures are presented in Table 3.14 and Figure 3.17, respectively. The former corresponds to visual rating, and the latter involves the measuring of mass loss of test samples. The upper limit to adequate deicing salt scaling loss is 1 kg/m². After 50 cycles of freezing and thawing, the deicing salt scaling of all mixtures was below 1 kg/m². The partial substitution of cement by SCMs was shown to increase the mass of scaling residue compared to the reference mixture made with 100% OPC. Slightly high scaling values were obtained for binder compositions made with high volume SCM replacements of more than 50%.

Table 3.14. Deicing salt scaling rating of HPC mixtures

Mixture	Number of freeze-thaw cycles						
	7	14	21	28	35	42	50
OPC	0	0	0	0	1	2	3
320-20SL-35FA	0	1	1	2	3	3	4
350-20SL-35FA	0	0	1	1	2	3	3
320-40FA	0	1	1	2	2	3	4
350-60SL-5SF	0	1	1	2	3	3	4
320-40FA-25LWS	0	1	1	2	2	3	3
350-60SL-5SF-25LWS	0	1	1	2	2	3	3
350-20SL-35FA-7.5EX	0	1	1	1	2	3	3
350-20SL-35FA-7.5EX-0.35FT	0	0	1	2	3	3	3
350-20SL-35FA-0.35FRW	0	1	1	2	3	3	4
350-20SL-35FA-25LWS	0	1	1	2	3	4	3
350-20SL-35FA-7.5EX-0.35FRW	0	0	1	1	2	2	3

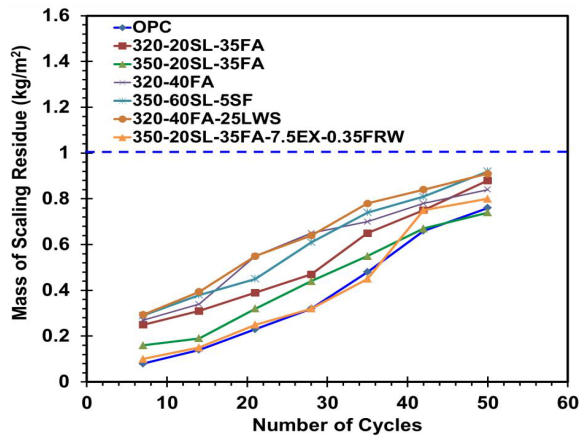


Figure 3.17. Durability performance of selected HPC mixtures

University of Oklahoma

3.4. Final mixture design

Table 3.15 summarizes the control, eco-pave-crete, and eco-bridge-crete mixture designs. The ODOT Class A mixture is for pavement applications, and the ODOT Class AA mixture is for bridge applications. These final mixture designs were based on 12 trial mixtures using the optimized binder compositions, optimized aggregate gradations, and the shrinkage mitigating strategies discussed previously. Eco-Bridge-Crete Mixture No. 1 used only micro-fibers while Mixture No. 2 used both the micro- and macro-fibers. These mixture designs served as the basis for subsequent study.

Table 3.15. Final mixture designs

Concrete mixture design components				
Material	Class A	Eco-Pave-Crete	Class AA	Eco-Bridge-Crete
Cement (Type I) (kg/m ³ , lb./yd ³)	306.7 (517)	175.7 (296.1)	348.8 (588)	214.7 (361.9)
Fly ash (Class C) (kg/m ³ , lb./yd ³)	-	50.2 (84.6)	-	61.3 (103.4)
Type K (kg/m ³ , lb./yd ³)	-	25.1 (42.3)	-	30.7 (51.7)
w/cm	0.45	0.45	0.40	0.40
Fine aggregate (River Sand) (kg/m ³ , lb./yd ³)	869.2 (1465)	793.8 (1338)	784.9 (1323)	784.3 (1322)
Coarse aggregate (#8 Limestone) (kg/m ³ , lb./yd ³)	-	456.2 (769)	-	450.3 (759)
Coarse aggregate (#57 Limestone) (kg/m ³ , lb./yd ³)	1097.6 (1850)	765.9 (1291)	1101.7 (1857)	750.5 (1265)
S/A by volume	0.44	0.41	0.42	0.40
AEA (kg/m ³ , oz./yd ³)	0.14 (3.9)	0.11 (3.0)	0.16 (4.4)	0.12 (3.2)
WRA (kg/m ³ , oz./yd ³)	0.57 (15.5)	0.44 (12.0)	0.99 (26.7)	1.27 (34.2)
Micro-fibers (kg/m ³ , lb./yd ³)	-	0.3 (0.5)	-	0.3 (0.5)
Macro-fibers (kg/m ³ , lb./yd ³)	-	-	-	1.8 (3.0) (Mixture No. 2)

3.4.1. Fresh properties

The fresh concrete properties for the five research mixtures are summarized in Table 2.6. The Class A and Eco-Pave-Crete mixtures compared very well in terms of slump, air content, and unit weight, with each meeting the ODOT specifications. The Class AA and two Eco-Bridge-Crete mixtures also compared very well in terms of fresh concrete properties, with all three also meeting the ODOT specifications. The Eco-Bridge-Crete 2 mixture did suffer a slight reduction in slump due to using both the micro- and macro-fibers but still has an acceptable level of workability.

Table 3.16. Fresh concrete properties

Mixture	Slump (mm, in.)	Air content (%)	Unit weight (pcf)
Class A	95.25 (3.75)	6.0	142.9
Eco-Pave-Crete	76.2 (3)	5.2	143.1
Class AA	152.4 (6)	6.1	143.7
Eco-Bridge-Crete 1	139.7 (5.5)	7.2	141.9
Eco-Bridge-Crete 2	101.6 (4)	4.6	142.5

3.4.2. Mechanical properties

The mechanical properties for the five research mixtures are shown in Table 3.17. The Class A and Eco-Pave-Crete mixtures compared very well and, in fact, the Eco-Pave-Crete mixture slightly outperformed the Class A mixtures even with a 20% reduction in cementitious content. The Class AA and Eco-Bridge-Crete mixtures also compared very well. The Eco-Bridge-Crete 1 mixtures had a slightly lower 28 day compressive strength compared to the Class AA, but had higher modulus of rupture and split cylinder strengths. The Eco-Bridge-Crete 2 mixture surpassed the Class AA mixture slightly in terms of 28 day compressive strength but noticeably exceeded the Class AA mixture in terms of modulus of rupture and split cylinder strength. This result is likely due to the macro-fibers included in this mixture design. All five mixtures showed comparable rates of compressive strength gains between 1 and 28 days.

Table 3.17. Mechanical properties

Mixture	Compressive strength (MPa, psi)	Modulus of rupture (MPa, psi)	Split cylinder strength (MPa, psi)	Modulus of elasticity (MPa, psi)
Class A	28.4 (4152)	3.6 (517)	2.5 (357)	24324.7 (3,528,000)
Eco-Pave-Crete	30.9 (4482)	3.8 (554)	2.7 (384)	25524.4 (3,702,000)
Class AA	32.7 (4747)	4.0 (583)	2.6 (375)	27444.6 (3,980,500)
Eco-Bridge-Crete 1	30.6 (4437)	4.3 (617)	2.7 (393)	24900.4 (3,611,500)
Eco-Bridge-Crete 2	33.1 (4805)	4.9 (712)	3.0 (435)	28440.9 (4,125,000)

Table 3.18 presents the normalized mechanical properties of the five research mixtures. The modulus of rupture and modulus of elasticity were normalized with respect to square root of the compressive strength, while the split cylinder strength was normalized with respect to the compressive strength taken to the two-thirds power. These are common normalization techniques used to compare concretes with different compressive strengths. The Eco-Pave-Crete mixture

slightly outperformed the Class A mixture. The Eco-Bridge-Crete mixtures noticeably outperformed the Class AA mixture in terms of modulus of rupture and split cylinder strength, with the Eco-Bridge-Crete 2 mixture having the highest performance of the three. It is apparent that the binder and aggregate optimization techniques resulted in mixture designs with less cementitious material but improved performance compared to the control mixtures.

Table 3.18. Normalized mechanical properties

Mixture	Modulus of rupture	Split cylinder strength	Modulus of elasticity
Class A	8.02	1.38	54,752
Eco-Pave-Crete	8.28	1.41	55,297
Class AA	8.46	1.33	57,773
Eco-Bridge-Crete 1	9.26	1.46	54,218
Eco-Bridge-Crete 2	10.27	1.53	59,508

Rutgers, The State University of New Jersey

3.5. Concrete performance evaluation

3.5.1. Fresh properties

Slump flow and J-ring test

The slump flow test was performed in accordance with ASTM C1611 using the inverted slump cone. Slump flow was the first test performed after the concrete batch was prepared. The target slump flow was between 546.1 mm (21.5 in.) and 546.1 mm (25.5 in.) Other subsequent mixtures used the same dosage of HRWR as the control mixtures, and then additional dosage of HRWR was added to compensate for the reduction of slump flow due to the addition of fibers. Table 3.19 shows the slump flows before and after adjustment and the final dosage of HRWR. The results clearly show that a reduction of slump flow was observed and the mixtures with PPE fibers obtained lower than the minimum required slump flow of 546.1 mm (21.5 in.) with as little as 0.10% fiber by volume. After the adjustment of HRWR was made, the minimum slump flow of 546.1 mm (21.5 in.) was achieved. It is important to determine the passing ability of an SCC mixture for field implementation in which the concrete should pass smoothly through tightly spaced reinforcement bars. As the J-ring value is highly dependent on the flowability, the mixture is considered to have an adequate passing ability if the J-ring test result is within three inches of the total slump flow. The J-ring values are presented in Table 3.19. It was noticed that mixtures containing fibers up to 0.15% by volume could pass the J-ring requirement set forth herein. However, once fiber volume increased further, passing ability became a big concern, and PPE 0.20 mixtures obtained the flow loss of 139.7 mm (5.5 in.) in the presence of tightly packed reinforcement. This indicates that additional attention is needed to use the FR-SCC mixture with more than 0.1% of PPE fiber when the reinforcement spacing is relatively small.

Table 3.19. Initial and adjusted slump values and J-Ring test results

Slump results	PPE 0.00	PPE 0.10	PPE 0.15	PPE 0.20
HRWR (kg/m ³ , fl. oz./yd ³)	2.52 (68)	3 (81)	3 (81)	3.5 (95)
Initial slump flow (mm, in.)	609.6 (24.0)	508 (20.0)	469.9 (18.5)	444.5 (17.5)
Adjusted slump flow (mm, in.)	609.6 (24.0)	584.2 (23.0)	558.8 (22.0)	571.5 (22.5)
J-ring (mm, in.)	571.5 (22.5)	533.4 (21.0)	482.6 (19.0)	431.8 (17.0)
+/- Slump (mm, in.)	-38.1 (-1.5)	-50.8 (-2.0)	-76.2 (-3.0)	-139.7 (-5.5)

T20 and visual stability index (VSI)

The T20 time was measured simultaneously with the slump flow test. The T20 time was limited within 20 seconds in order to assure the flowability of the SCC within a relatively short period of time. As a low-viscosity SCC mixture is generally preferred, the team designed to obtain a minimum 2 seconds of T20 time for the control mixture. Table 3.20 summarizes the T20 test results. The results show that the viscosity and T20 time generally increased as the fiber addition rate was higher. While the total slump flow remained relatively close for each mixture, the flow did move slower for the higher fiber mixtures. The VSI was taken immediately after the slump flow was measured. Table 3.20 presents the VSI results of four mixtures tested in this study. The first two mixtures (control mixture and minimum fiber mixture) obtained the same VSI of 0 indicating unlikely to segregate or bleed. As fibers were added and slump flow was inhibited slightly, a halo-like ring was formed around the slump flow indicating segregation may be occurred. For PPE 0.15 and PPE 0.20 mixtures, the halo-like rings remained small but the aggregate did not visibly segregate after the slump flow test, therefore it was determined to have the VSI of 1. While a VSI of 1 was the highest found in the mixtures in this study, trial mixtures have shown that additional fibers could lead to a higher degree of segregation or VSI of 2 or 3. The VSI of 0 is considered ideal, and the VSI of 1 also is acceptable in most cases. The VSI of 2 or 3 indicates the mixture is not ready for field implementation and additional measures must be taken to reduce segregation.

Table 3.20. T20 and VSI test results

Mixture	PPE 0.00	PPE 0.10	PPE 0.15	PPE 0.20
T20 (s)	6.1	5.5	7	9.6
VSI	0	0	1	1

L-box

The L-box test used in this study is described in Section 2.3.2. A desirable h1/h2 ratio is set forth to be below 2.0 based on the previous study performed by the RIME Team (Nassif, 2008). If the h1/h2 ratio of L-box test exceeds 2.0, the SCC will have trouble passing through confined reinforcement. Table 3.21 summarizes the L-Box testing results. Similar to the J-ring test, it was noticed that the PPE 0.20 mixture did not pass the set forth h1/h2 ratio because of higher friction

between fibers and cement matrix. Therefore, a precaution should be made for the mixtures with the addition of fibers beyond 0.15% by volume.

Table 3.21. L-Box test results

Mixture	PPE 0.00	PPE 0.10	PPE 0.15	PPE 0.20
h1/h2 ratio	1.2	1.5	2	2.5

3.5.2. Air content

Adequate air entrainment is an important factor where concrete may be subjected to freeze and thaw cycles. The targeted air content of 4-8% by volume is suggested, and Table 3.22 shows the air contents measured by two test methods; pressure and gravity. The air content differed slightly between methods, however, the variance was relatively small and both values were within the desired air content range. In general, the air content increases as the fiber content increases; however, this is deemed to be a side-effect of the increased dosage of HRWR with higher fiber volume.

Table 3.22. Air content test results

Mixture	PPE 0.00	PPE 0.10	PPE 0.15	PPE 0.20
Air content (Pressure)	7%	7%	7.8%	8%
Air content (Gravity)	6.2%	6.5%	7.1%	6.9%

As a summary, FR-SCC mixtures with maximum 0.15% PPE by volume provide similar fresh concrete properties as the control SCC mixture. However, a precaution should be made if over 0.20% PPE volume is utilized.

3.5.3. Mechanical properties

Mechanical properties including compression, tension, and modulus of elasticity were tested for the FR-SCC mixtures at 28 days after mixing. The samples were stored in the environmental chamber to provide steady temperature of 74°F and relative humidity of 50%. A total of 9 cylindrical samples from each mixture were used for the mechanical testing. Six samples were capped using a sulfur capping compound to distribute the stress on the cylinder where three of which were for the compression test and other three were used for the modulus of elasticity test. The last 3 samples were used for the splitting tensile strength test. The cracking strain which is the splitting tensile strength divided by the modulus of elasticity, was calculated. The cracking strain represents the cracking capacity that a mixture can sustain before cracking begins. Table 3.23 summarizes the testing results of these mixtures. The parentheses next to each value indicates the percentage difference compared to control mixture, PPE 0.00.

Table 3.23. Mechanical properties (% difference compared to the control mix, PPE 0.00)

	PPE 0.00	PPE 0.10	PPE 0.15	PPE 0.20
Compressive strength (MPa, psi)	38.8 (5,632)	37.1 (5,364) (-4.8%)	37.9 (5,494) (-2.5%)	35.4 (5,130) (-8.9%)
Tensile Strength (MPa, psi)	2.5 (361)	2.7 (385) (6.6%)	2.7 (398) (10.2%)	2.8 (410) (13.6%)
Elastic Modulus (MPa, ksi)	29.6 (4,295)	28.7 (4,165) (-3.0%)	29.03 (4,210) (-2.0%)	27.5 (3,981) (-7.3%)
Cracking Strain ($\mu\epsilon$)	84	92 (9.5%)	95 (13.1%)	103 (22.6%)

It was noticed that as fiber content increased, the compressive strength slightly decreased by 8.9%. This is because the strength of the concrete comes from the bond between cement paste and aggregate, but the flexible fibers mixed into the cement matrix may weaken the bond strength between them. The modulus of elasticity also decreased by a small margin of 7.3%. The splitting tensile strength, however, increased with the addition of fibers up to 13.6%. The friction between cement paste and fiber help increase the tensile strength, and the fibers helped prevent pulling out and made the concrete become more ductile. The increase in tensile strength and decrease in modulus of elasticity increased the cracking strain and is a key to increase the cracking capacity which mitigate cracking in restrained shrinkage rings.

3.5.4. Shrinkage properties

Free shrinkage

Comparator measurements for free shrinkage were taken throughout the testing period at least twice every week. The free shrinkage is an indicator of the stresses induced in the restrained shrinkage rings. Figure 3.18 represents the free shrinkage results of this study. It was observed that free shrinkage decreased as fiber content increased. When PPE fibers were added at 0.20% by volume, free shrinkage decreased by 9%. However, the shrinkage improvement was not as effective as other studies. It was reported that the free shrinkage of fiber-reinforced concrete was about two-third less than that of the control mixture when the fiber content was used up to 0.75% by volume (Saje, 2011). Such small improvement of free shrinkage strain could be a result of the curing regime, because it was reported that no curing increased the ultimate free shrinkage as well as the shrinkage rate (Na, 2013). The fact that the shrinkage specimens were not moisture cured after 1 day may greatly influence the free shrinkage while the effect of fibers was negligible compared with curing regime.

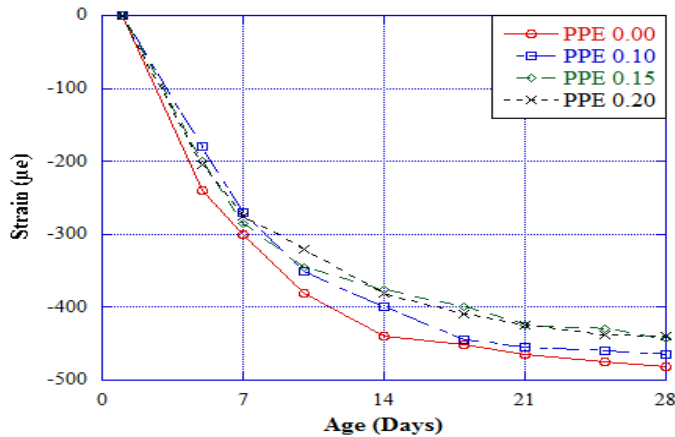


Figure 3.18. Free shrinkage strain

Restrained shrinkage

The restrained shrinkage testing was performed in accordance with ASTM C1581. Two AASHTO restrained shrinkage rings were prepared. Two rings were equipped with the FSGs (foil strain gage) attached to the inner surface of the steel ring, and one ring out of two also equipped with the six embedded VWSGs forming the closed hexagon along the top surface of the concrete ring. Data for the sensors were monitored regularly for any indications of cracking on the steel and concrete rings. Once a crack was suspected, a digital microscope was used to observe the crack over the course of testing period and check its propagation and widening as shrinkage continued.

Crack map development

Once FSG or VWSG indicated any possible crack, the ring was then observed using the digital microscope. If the crack was not yet visible on the surface, the ring was checked daily based to find the first signs of cracking. The cracks observed using the digital microscope were monitored over the course of the test. The major crack became apparent propagating up and down the surface of the ring at 28 days. As stresses built, the crack propagated inward towards the steel ring at the center of the specimen. Once the crack reached the ring, a line typically appeared through the layer of paraffin wax coating the top surface of the ring. The day on which this line appeared was noted as the day the crack has propagated completely. Figures 3.19 and 20 show the restrained shrinkage results of PPE 0.00 mixture. The cracking strain was calculated by the splitting tensile strength divided by the modulus of elasticity shown in Table 3.23. A crack-map taken over the course of the monitoring period, up to 28 days, is developed as shown in Figure B.5 in Appendix B. The numbers next to each crack indicate the crack length and width in millimeters, and the day when it was first observed. The control SCC mixture (PPE 0.00) showed extensive cracking throughout the entire ring at the end of the testing period. Soon after the wet-curing process was completed, the concrete started shrinking and the stress in the concrete, as well as steel rings, began developing immediately (see Figures 3.19 and 20). Figure 3.19 shows that three VWSGs developed tensile stresses while the other three sensors developed compressive stresses. This is because when one portion of the concrete ring is in tension, the

adjacent portions are in compression by the equilibrium. Figure 3.20 shows that all FSGs develop tensile stresses because of the shrinkage of the concrete ring.

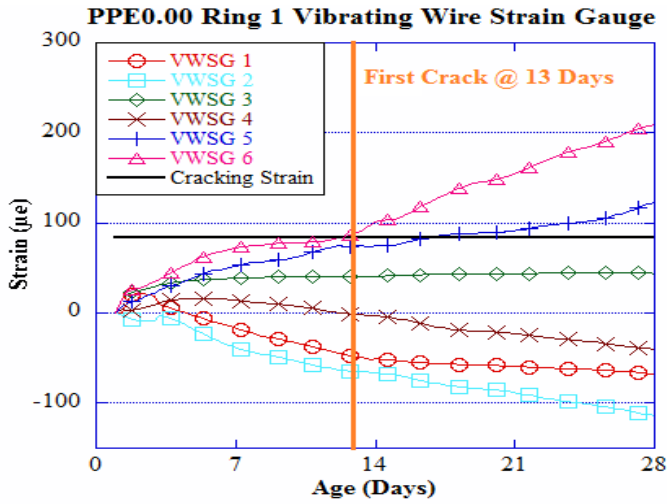


Figure 3.19. Concrete strain (VWSG) of PPE 0.00 mixture ring 1

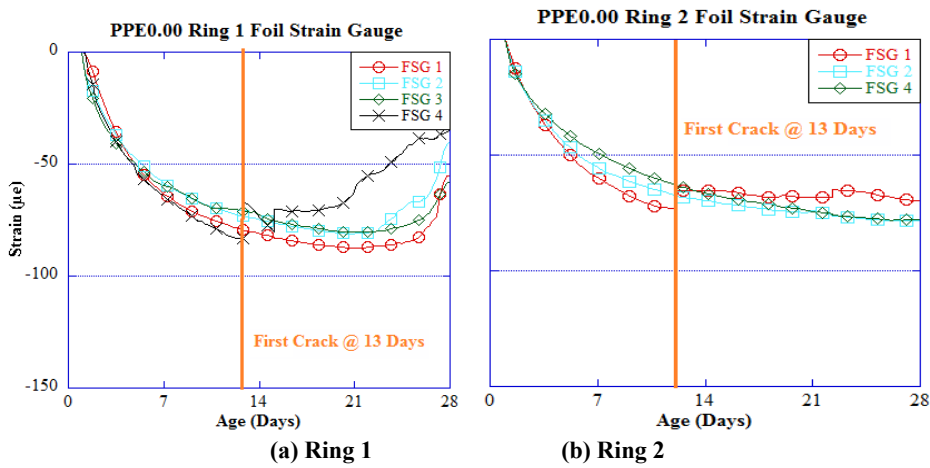


Figure 3.20. Steel strain (FSG) of PPE 0.00 mixture

The Ring 1 on which both VWSGs and FSGs were installed developed tensile stress within VWSG-3, -5 and -6 sections and compressive stress in all FSGs. FSG-4 indicated a drop in strain of approximately $20 \mu\epsilon$ at 13 days (Figure B.5 in Appendix B). This loss of restraint indicated that cracking may have begun in that quadrant of the ring (in the vicinity of FSG-4). Shortly

thereafter, VWSG-6 of the same ring detected a strain exceeding the calculated cracking strain of $83 \mu\epsilon$.

The ring surface was monitored to quantify the cracks as soon as either FSG or VWSG indicated a potential crack. Although both FSG and VWSG provided a signal of cracking at 13 days, no crack was observed by visual monitoring. A preliminary crack-map was performed at 14 days, and a crack was found within the vicinity covered by FSG-4 between VWSG-5 and VWSG-6. This indicates that cracking began in the concrete close to the steel ring on the 13th day and worked its way outward by the 14th day. Additional crack was found at 19-20 days near VWSG-5, and the strain in concrete exceeded the cracking threshold. The crack found at 14 days propagated completely throughout the entire ring at 20 days when additional stress release on FSG-4 was observed.

The Ring 2, with FSGs only, showed an increase in strain similar to Ring 1. A slight jump in the FSG data indicated a crack at 13 days in the vicinity of FSG-1. The crack was observed with the microscope on 14 days but did not propagate fully until 20 days. The crack was initially observed at 14 days as Ring 1 in the vicinity between FSG 1 and FSG 2. Smaller and insignificant cracks later formed in other regions of the ring. At 20 days, the major crack was observed and extended the entire height of the ring. A small opaque line was visible through the wax as shown in (Figure B.6 in Appendix B) showing the hardened paraffin wax has split due to the pulling apart of the crack.

The restrained shrinkage results for PPE 0.10 mixture are shown in Figures B.7 and B.8 in Appendix B. The crack-maps developed over the course of monitoring period up to 28 days, and they are shown in Figure B.7 in Appendix B. The numbers next to each crack indicate the crack information as addressed earlier. The addition of 0.10% PPE fibers showed a small but noticeable effect on the concrete shrinkage resistance. Free shrinkage was slightly reduced by approximately 4% at 28 days, while the cracking strain was increased by almost 6%. When they were coupled, the crack initiation was delayed, resulting in less shrinkage induced cracking. Ring 1 of PPE 0.10 mixture showed that the tensile stresses were concentrated at opposite ends of the ring near VWSG-3 and VWSG-6, as shown in Figure B.8 in Appendix B. FSGs in Ring 1 indicated a crack formed at 14 days after a large drop in strain in FSG-2. VWSG-3 exceeded the cracking strain of $92 \mu\epsilon$ after 3 days indicating a crack occurred at the depth of the anchor bolt of strain gauges. This crack became visible at 21 days in the vicinity of VWSG-3 as shown in the red line in Figure B.9 in Appendix B, and propagated the full height of the ring. Once the crack propagated throughout the concrete ring, the strain in the steel ring was leveled off, indicating no significant stress development in the ring and no additional shrinkage stress development in the concrete ring.

The Ring 2 performed similarly to Ring 1 through the first 14 days. Figure B.8 in Appendix B (b) shows a significant change in strain or a stress relaxation at 14 days at FSG-2. A crack was observed via the digital microscope on the next day (15 days) in the vicinity between FSG-1 and FSG-2. Shortly after the first jump, approximately at 17 days, other two FSGs (FSG-1 and -4) also experienced a sudden loss in strain. This strain loss was likely caused by additional cracks forming in the region around FSG-1 and -4 as well as by the growth of the main crack around FSG-2. The crack between FSG-1 and FSG-2 shown in red in Figure B.9 in Appendix B

eventually extended the entire height of the ring by day 20. At 20 days, the crack became visible through the layer of paraffin wax coating, and stresses in all sensors were leveled off or fell indicating a loss in restraint along the ring.

PPE 0.15 mixture had a higher cracking strain than both the control and PPE 0.10 mixture. Figure B.10 in Appendix B represents the concrete strain monitored by VWSGs and Figure B.11 in Appendix B represents the steel strain recorded by FSGs for this mixture. Figure B.12 in Appendix B summarizes the crack-maps developed during the monitoring period of 28 days.

The stress in Ring 1 developed more slowly than in previous mixtures. FSGs indicated the first crack happened at 18 days, centered on FSG-4. The crack was observed while developing the crack-map at 18 days, as shown in Figure B.13 in Appendix B. The crack was fully propagated at 23 days. However, VWSGs did not exceed the cracking strain threshold until shortly after 19 days, as shown in Figure B.10 in Appendix B, unlike previous mixtures where VWSGs indicated cracking just before the crack was visible. Once VWSG-6 indicated a possible crack, strains in nearby sensors decreased notably in VWSG-5. Ring 2 of PPE 0.15 mixture was found to have cracked earlier than Ring 1. Two FSGs (FSG-1 and -3) attached to the ring simultaneously jumped at 15 days. After the first crack was formed, strain continued to increase in all FSGs until 21 days. A crack map developed at 22 days shows that the initial cracking near FSG-3 had reached the full height of the ring, the stress relaxation occurred on the steel. Albeit cracking in the Ring 2 started earlier, the crack intensity was not as extensive as in Ring 1. After initial cracking, the strain in the steel continued to build in the other three FSGs. Small cracks were observed in the vicinity of FSG-1, and secondary cracking may have occurred at 22 days when the compressive strain in FSG-1 began to decrease. Similar to previous other mixtures, the crack in Ring 1 propagated outward and increased lengthwise as time passed. After the crack fully propagated at 23 days, strain values leveled off, as shown in both Figures B.10 and B.11 in Appendix B for VWSGs and FSGs, respectively.

The restrained shrinkage results for the PPE 0.20 mixture are shown in Figures B.13 (VWSGs) and and Figure B.14 (FSGs) in Appendix B. The cracks were monitored by the digital microscope, and the crack map is shown in Figure B.15 in Appendix B. As described above, the additional fibers (0.20% by volume) improved the free shrinkage by 9% compared to the control SCC mixture. When this improvement was coupled with the higher cracking strain, the crack resistance to the restrained shrinkage was significantly improved.

Figure B.14(a) in Appendix B shows that the first ring of PPE 0.20 mixture had a steady increase in steel strain up until day 21, at which FSG-1 experienced an immediate strain loss by $20\mu\epsilon$. The crack map developed at 22 days showed a small crack forming between VWSG-1 and VWSG-2. Figure B.13 in Appendix B shows VWSG-1 and -2 having high tensile stress when the cracking was observed and exceeding the cracking strain threshold of $103\mu\epsilon$ at 22 days. At 25 days, VWSG-1 began to show a large increase in tensile strain. This is because cracking likely propagated the entire height of the ring at this time. Observation of the paraffin wax layer on the top surface showed that the crack had expanded. The crack map at 28 days shows that most cracking was centered near VWSG-1 and VWSG-2, while most other vicinities remained intact, as shown in Figure B.15 in Appendix B.

Ring 2 of PPE 0.20 mixture showed signs of cracking earlier at 18 days in the vicinity of FSG-4. The visual inspection confirmed that this crack was located near FSG-4. Strain in the steel steadily increased in the un-cracked portions of the ring until 23 days, at which two FSGs showed a rapid decrease in compressive strain, while two showed an increase. Observation of the ring showed that the initial crack had reached the steel at 23 days. The crack map developed at 28 days showed that the single large crack formed outside of the ring was not as widespread as it was with other mixtures. While some cracks appeared in the region surrounding FSG-2 and -3, PPE 0.20 attained much less cracking overall. One of the parameters to compare the cracking resistance performance against the restrained shrinkage is the age of first cracking. If the mixture is improved, it will delay the onset of cracking in the restrained shrinkage test. In this study, FSGs showed a sudden drop in compressive strain in the steel ring, and it was noticed that a drop of at least $20 \mu\epsilon$ is a good indicator that cracking has begun, especially when the strain continued to decrease afterwards. Alternatively, VWSGs also can be used to determine the development of the crack in the ring. In this study, when the strain measured by VWSGs exceeded the cracking strain, cracks were present in the vicinity of VWSGs. Table 3.24 summarizes the various cracking age measured during the course of this study. A general trend of increasing cracking age was observed as fiber contents increased. At the highest fiber content (PPE 0.20), it took 4-9 days longer or 30-70% increase to show initial signs of cracking than the control mixture. In the context of this study, such increase is a significant amount of time when considering the free shrinkage of PPE 0.20 mixture increased by 10% at 28 days. The duration for the crack to propagate outwards was fairly consistent at 4-6 days between mixtures regardless of fiber content.

Table 3.24. First cracking age for restrained shrinkage rings

Age of cracking	PPE 0.00		PPE 0.10		PPE 0.15		PPE 0.20	
	R-1	R-2	R-1	R-2	R-1	R-2	R-1	R-2
Cracking onset 1 by FSG	13	13	14	15	18	15	22	17
Cracking onset 2 by VWSG	13	N/A	15	N/A	19	N/A	22	N/A
First crack observed	14	14	16	15	18	16	22	18
Complete propagation	20	20	22	20	23	21	25	23

Both types of sensors used on the restrained shrinkage rings were found to be helpful in determining the age of cracking in the restrained shrinkage ring. While VWSGs seem more capable of finding the specific location of a current or future crack, their function is limited once a crack opens up. FSGs, however, seem to be better indicators when the crack will happen, often showing a strain jump at the same time or slightly before the crack is visible on the surface. VWSGs on the other hand lag behind slightly; reaching cracking strain just after the crack is detected by FSGs. Both sensors can be used to provide the cracking onset without adversely affecting the cracking behavior. Measuring the largest crack width in each sample can be an indicator of the effectiveness of PPE fibers in preventing cracks from opening up. The digital microscope used for crack observation allowed for precise measuring of crack width at 0.0002 in. interval. Smaller crack width indicates the concrete may retain some strength even after cracking occurs, thereby preventing excessive crack propagation. The crack widths measured are summarized in Table 3.25.

Table 3.25. Max crack widths and cracking area for restrained shrinkage rings

	PPE 0.00		PPE 0.10		PPE 0.15		PPE 0.20	
	R-1	R-2	R-1	R-2	R-1	R-2	R-1	R-2
Max crack width (mm, in.)	0.076 (0.003)	0.086 (0.0034)	0.076 (0.003)	0.076 (0.003)	0.076 (0.003)	0.076 (0.003)	0.061 (0.0024)	0.071 (0.0028)
Cracking area (mm ² , in. ²)	19.1 (0.03)	19.1 (0.03)	16.8 (0.03)	17.3 (0.03)	15.5 (0.02)	15.4 (0.02)	12.7 (0.02)	13.1 (0.02)

It was noticed that there was a decrease in crack width as fiber volume was increased. Average crack width between samples were from 0.081 mm (0.0032 in.) (PPE 0.00) to 0.066 mm (0.0026 in.) (PPE 0.20) or a decrease of 19%. Fibers added into the mixture have been found to bridge the gap created by the crack. As a result, a greater force is required for this crack to expand and so crack width is limited. An alternative metric used to quantify the extent of cracking throughout the ring test is the measurement of cracking area. To calculate the cracking area of a ring sample, the length and width of all cracks are measured through the digital microscope described earlier and the area of all the cracks is calculated. Unlike the maximum crack width measurement, the cracking area gives us a better understanding of the extent of cracking throughout the ring rather than at one specific point. For FR-SCC, this is especially important because fibers may cause smaller, numerous, more closely dispersed, cracks as opposed to a single large crack. The results of the cracking area measurements are summarized in Table 3.25. It is apparent that the cracking area reduced noticeably with even the smallest addition of fibers tested in this study. Even as the maximum crack width remained unchanged from PPE 0.10 to PPE 0.15, the cracking area was reduced with the small addition of fibers from an average of 17.10 mm² (0.0265 in²) to 15.48 mm² (0.024 in²). The average cracking area was reduced by 34% compared to the control mixture when fibers were added at 0.20% by volume.

4. VALIDATION OF ECO-HPC PERFORMANCE IN LARGE-SCALE ELEMENTS

The aim of this section is to validate the performance of optimized Eco-HPCs in large-scale elements. Focus was placed to evaluate the shrinkage of slab sections and flexural performance of reinforced concrete beams made with optimized Eco-Bridge-Crete. As such, large-scale specimens, including reinforced slab and beam elements were cast, which is described in details below.

4.1. Shrinkage of concrete slab section

The aim of this subtask was to evaluate the shrinkage deformation of concrete slabs made with selected concrete mixtures. As shown in Figure C.1 in Appendix C, three slabs measuring 1.8×1.8 m (6×6 ft.) and 150 mm (0.5 ft.) in depth were constructed to evaluate the variation in relative humidity and shrinkage deformation of different concrete mixtures. The mixture parameters include the incorporation of fiber, lightweight sand, expansive agent, and high volume SCMs and the results were compared with that of the MoDOT reference mixture. The mixture design parameters of selected concrete mixtures for slab sections are presented in Table 4.1.

The slabs were fully instrumented by utilizing strain gauges, relative humidity sensors, and thermocouples to monitor the deformation caused by concrete shrinkage, humidity and temperature variations over time. A detailed description of the instrumentation used in this investigation is provided below. In this study, the embedment type of strain gauges (KM-120-120-H2-11, manufactured by KYOWA) was used to monitor the shrinkage deformation of concrete, as shown in Figure C.2 in Appendix C. The sensor has the outer body of 120 mm (4.7 in.) sensing grid with an effective gauge length of 75 mm (3.0 in.). The gauge is waterproof and is designed to be placed in fresh concrete to directly measure the shrinkage deformation associated with concrete. The sensor consists of a 75 mm (3.0 in.) 120 ohm (Ω) foil strain gauge (nickelchromium alloy on polyimide backing). The surface of the gauge is designed to have a honeycomb pattern that enables adequate bond to concrete. The thermocouple wire (UX-08542-24, manufactured by Coleparmer) used in the instrumentation was a Type T 20 gauge wire. These thermocouples consist of copper and constantan wires, and are functional between -250 to 250°C (-418 to 482 °F). The ends of the solid thermocouple wires were twisted and then soldered to ensure an adequate electrical connection.

Table 4.1. Selected concrete mixtures for slab sections

Concrete type	Codification	Reinforcement	w/cm	Binder content		Binder type	Fiber type and content		Shrinkage mitigating materials	
			0.40	350 kg/m ³	375 kg/m ³	75% OPC + 25% Class C FA	45% OPC + 20% SL + 35% Class C FA	TUF strand fibers (0.35%)	Steel fibers from tire (0.35%)	25% LWS
MoDOT reference mixture	FA25	x	x		x	x				
Optimized Eco-Bridge-Crete	SL20FA35-25LWS	x		x			x			x
	SL20FA35-7.5EX-0.35FRW	x		x			x	x		x

The small (6 × 20 mm) [0.24 × 0.79 in.] capacitive relative humidity sensor (HIH-4030, manufactured by Sparkfun) was used to measure the relative humidity inside concrete. The accuracy of the sensors is reported by the manufacturer to be ±2% RH between 10% and 90% RH, and range up to ±4% at 100% RH. In order to embed the RH sensor in concrete, the sensor was placed inside the 12 mm (1/2 in.) PVC tube and the end of the tube was covered by Gore-Tex to allow moisture transmission, while preventing the penetration of liquid water and solid particles that may lead to an error in measurement. The encapsulated RH sensor before embedding in concrete is shown in Figure C.3 in Appendix C.

Figure C.4 in Appendix C shows the instrumentation layout, including embedded concrete strain gauge, relative humidity sensor, and thermocouple for monitoring the shrinkage deformation of concrete used for slab sections. As indicated in Figure C.5 in Appendix C, each slab was instrumented at three different locations to monitor the concrete shrinkage behavior at the center, edge, and corner of the slab, corresponding to points A, B, and C, respectively. Station A, located at the center of slab, has three embedded strain gauges in the longitudinal direction, three thermocouples, and three relative humidity sensors placed along the height of the slab. Stations B and C, located at the edge and corner of the slab, have similar instrumentation layout, including four embedded strain gauges (two in the longitudinal, as well as two in the transverse direction), two thermocouples, and two relative humidity sensors. Sensors were placed at different thicknesses of slab to monitor strain, temperature and relative humidity along the height of slabs.

Both the strain and the temperature data was recorded using Campbell Scientific data acquisition hardware and software. Lead wires from the strain gauges were routed through an AM16-32

multiplexer, using a separate completion module for each gauge on the multiplexer. The data logger used was a Campbell Scientific CR1000. The thermocouple wires were routed through an AM25T multiplexer, which has an internal RTD (resistance temperature detector) to measure the cold junction temperature required to compute the temperature at the soldered end of the thermocouple. The multiplexer was controlled by the CR1000 data logger. In addition to the strain and temperature instrumentation, relative humidity sensors were collected.

A summary of the instrumentation plan and designation of sensors utilized for each slab are listed in Tables 4.2 and 4.3, respectively.

Table 4.2. Summary of instrumentation plan used for each slab

Point	# Embedded strain gauge	# Relative humidity sensor	# Thermocouple
A	3 (longitudinal direction)	3	3
B	4 (two longitudinal and two transverse directions)	2	2
C	4 (two longitudinal and two transverse directions)	2	2
Sum	11	7	7

Table 4.3. Codifications of sensors used for slab instrumentation

Slab #1 made with 25% FA (FA25)			
Strain sensors	Humidity sensors	Temperature sensors	Codifications
1-M-SL-1	1-M-H-1	1-M-T-1	<ul style="list-style-type: none"> • 1 refers to slab made with FA25 mixture (MoDOT reference mixture). • M, S, and C refer to center, side and corner points of slab. • S, H, and T refer to strain, humidity and temperature sensors. • SL and ST refer to strain gauges in longitudinal and transvers directions. • 1, 2, and 3 represents bottom, middle, and top parts along height of concrete slab. • Similar designations are used for other slabs, except that slabs made with SL20FA35-25LWS and SL20FA35-7.5EX-0.35FRW mixtures are designated as 2 and 3, respectively.
1-M-SL-2	1-M-H-2	1-M-T-2	
1-M-SL-3	1-M-H-3	1-M-T-3	
1-S-SL-1	1-S-H-1	1-S-T-1	
1-S-ST-1	1-S-H-3	1-S-T-3	
1-S-SL-3	1-C-H-1	1-C-T-1	
1-S-ST-3	1-C-H-3	1-C-T-3	
1-C-SL-1			
1-C-ST-1			
1-C-SL-3			
1-C-ST-3			

All slabs were reinforced with two reinforcement mats of longitudinal #4 bars spaced at 250 mm (9.8 in.) which were placed at the top and bottom parts of slabs. The top and bottom rebar mats were located 25 and 50 mm (0.98 and 2 in.) from the top and bottom of the concrete, respectively. All concrete mixtures were made in a local concrete batching plant to confirm the

ability of proposed concrete mixtures to apply under actual field conditions. The HRWR dosage was adjusted to secure the slump consistencies, varying between 150 and 200 mm (5.9 and 7.9 in.). The AEA concentration was also adjusted to ensure the fresh air volume of $5\% \pm 2\%$ for all mixtures. The w/cm was fixed at 0.4 for all mixtures. In total, three concrete slabs were constructed including two optimized Eco- and crack-free HPC and a control concrete slab using MoDOT reference mixture targeted for bridge deck.

After casting, the top surface of the beams was covered with wet burlap and plastic sheeting, and a wet surface was maintained for seven days to retain moisture for a proper initial moist curing. After seven days, the burlap and plastic sheets were removed, and the slabs were demolded and exposed to air drying in the lab environment. Shrinkage of the concrete mixtures is not affected by humidity and temperature variations caused by seasonal changes. Therefore, the shrinkage results of the concrete mixtures can be isolated from warping and curling deformations caused by seasonal variations. The slab construction procedures, including concrete arrival using mixing truck, placement, consolidating, finishing, and curing, are presented in Figure C.6 in Appendix C.

4.1.1. Shrinkage and relative humidity measurement

Figure C.7 in Appendix C presents the results of shrinkage deformation along the height at different stations of the investigated slabs. In this figure, negative and positive signs correspond to shrinkage and expansion, respectively. As mentioned earlier, all slabs were subjected to wet curing using wet burlap and plastic sheet for seven days before exposure to air drying condition. The results of shrinkage deformation were shown to be a function of concrete mix design, location, and depth of slab. Expectedly, the slab made with 25% FA replacement exhibited higher magnitude and rate of shrinkage deformation compared to the optimized Eco-Bridge-Crete. This difference became more dominant for the top surface of the concrete slab. For instance, cluster A (i.e., station A) of the control slab had an expansion of 100 μ strain after 7 days of wet curing followed by 100 μ strain shrinkage after 30 of drying (see sensor 1-M-SL-3). However, no shrinkage deformation was observed for other slabs prepared with optimized Eco-Bridge-Crete. Regardless of the concrete composition, the top part of slab underwent larger shrinkage deformation compared to the mid-height and bottom part of slab thickness. This is attributed to faster evaporation rate of the top surface of concrete. Given the expansion induced stresses, the SL20FA35-7.5EX-0.35FRW mixture containing 7.5% CaO-based EX exhibited significant expansion. The magnitude of expansion was shown to vary along the height of the slab. Strain gauges located at the top part of the concrete slab experienced larger extent of expansion compared to the middle and bottom parts of the slab. For example, the top surface of concrete exhibited 600-800 μ strain expansion compared to 350-400 μ strain expansion recorded for sensors located at the middle and bottom parts of the slab. This is due to higher exposure of the top surface to the moist curing provided by wet burlap during the first seven days. As explained earlier, the effectiveness of EX to generate expansion is significantly affected by the initial moist curing. The penetration of water into the concrete slab at early-age can provide more water to facilitate the hydration of CaO-based EX, thus indicating larger magnitude of expansion. The incorporation of 25% LWS was shown to be fully effective at reducing shrinkage rate and magnitude. No shrinkage was obtained for slabs made with 20% SL and 35% FA containing 25% LWS. This confirms that the combined use of SCM replacement and LWS can be fully beneficial at reducing shrinkage rate and magnitude. The slab containing 25% LWS

exhibited higher relative humidity after 30 days of drying. This enhanced relative humidity of paste matrix is attributed to the internal curing provided by LWS, which can maintain larger relative humidity within the paste matrix for a longer duration.

It can be noticed from Figure C.8 in Appendix C that shrinkage deformations recorded for side and corner (stations B and C) points of the slab were larger than that of the sensors located at the center (station A) of the slab. This is due to faster rate of evaporation of the concrete surface. This was consistent with results of humidity sensors placed at the side and corner parts of the slab, where a larger drop in relative humidity was exhibited, compared to that of the middle sensor, irrespective of concrete composition. Interestingly, this effect was less dominant for the slab made with 25% LWS. The lowest relative humidity values observed for the FA25, SL20FA35-25LWS, and SL20FA35-7.5EX-0.35FRW mixtures were 82%, 96%, and 90%, respectively, which were recorded by RH sensors located at the top-corner part of the slab. The shrinkage deformation values corresponding to such RH sensors were 80 μ strain (shrinkage), 40 μ strain (expansion), and 400 μ strain (expansion) for the FA25, SL20FA35-25LWS, and SL20FA35-7.5EX-0.35FRW mixtures, respectively, after 30 days of drying. Such shrinkage values corresponded to the largest deformation registered by sensors (the most critical point) after 30 days of drying. Trends of shrinkage deformation recorded by the transverse strain sensors are similar to those of the longitudinal sensors. This phase is currently underway to achieve the stabilized shrinkage deformation.

4.1.2. Temperature measurement

Figure C.9 in Appendix C shows the temperature variations at different locations along the height of the investigated slabs. It is interesting to note that the slab FA25 made with higher binder content and lower OPC replacement (i.e., only 25% FA substitution) developed higher temperature rise (due to the hydration evolution of binder after concrete placement) compared to other slabs made relatively high volume SCMs.

The maximum temperature recorded for slabs made with FA25, SL20FA35-25LWS, and SL20FA35-7.5EX-0.35FRW mixtures were 46°C (114.8 °F), 38°C (100.4 °F), and 42°C (107.6), respectively. The lowest temperature rise registered by embedded thermocouples was obtained for the slab prepared with 25% LWS. This mixture also exhibited lower rate of heat transfer compared to the faster heat reduction observed for other mixtures. As shown in Figure C.9 in Appendix, the embedded thermocouples located at three depths within the deck depth captured similar temperature variation throughout the section. This is due to placement of slabs in a lab environment, which had consistent daily temperature. Regardless of the concrete mixture design, all slabs had similar temperature of 25°C (77 °F) after 30 days of drying, which was consistent with ambient temperature registered for lab condition.

University of Oklahoma

4.1.3. Pavement test sections

In addition to these three slabs discussed above, the deformation (i.e., shrinkage) of two pavement mixtures (Class A and Eco-Pave-Crete) were tested by the University of Oklahoma

research team. Structural performance testing of the pavement mixture designs involved construction and instrumentation of full scale pavement sections as part of the Decatur Avenue Pavement Project. The project involved the Oklahoma Department of Transportation (ODOT), Garver Engineering, and the City of Norman. The final pavement design, shown in Figure C.10 in Appendix C, consisted of a 203.2 mm (8 in.) thick, dowel jointed concrete pavement (DJCP) with contraction joints spaced 4876.8 mm (16 ft.) longitudinally and 3352.8 mm (11 ft.) transversely. In accordance with ODOT requirements, the transverse joints use 25.4 mm (1 in.) diameter, 457.2 mm (18 in.) long epoxy coated smooth dowels, spaced 304.8 mm (12 in.) on center, while the longitudinal joints use deformed #4 bars measuring 762 mm (2.5 ft.) long and spaced 762 mm (2.5 ft.) on center.

Preparation work for the pavement included removal of the existing asphalt roadway, base, and subbase, as shown in Figure C.11 in Appendix C. Lime modification and compaction of the subgrade, and installation and compaction of the 152.4 mm (6 in.) thick aggregate base, as shown in Figure C.12 in Appendix C. The research team documented the construction work and performed ASTM testing of the subgrade and base in accordance with ODOT's specifications.

The instrumentation plan for the pavement sections consisted of vibrating wire strain (VWS) gauges placed in "trees" at three locations within a pavement section as shown Figure C.13 in Appendix C. Two of the trees were placed directly under the wheel load of a vehicle traveling on the roadway, while the third was placed in the direct center of the panel. A total of 8 VWS gauges were installed in each panel, with Tree No. 1 using 4 gauges and Tree Nos. 2 and 3 using 2 gauges each. The gauge orientation allowed for measuring both transverse and longitudinal shrinkage and temperature strains within the pavement sections.

Photographs of the VWS gauge placement for a typical panel are shown in Figure C.14 in Appendix C, which includes the overall layout as well as a close-up of Tree No. 1. Lead wires for the gauges were run to Geokon data acquisition (DAQ) boxes, which were placed within steel lockboxes for protection. The DAQ recorded shrinkage and temperature strains at 30 minute intervals for the initial 28 days and then at 2 hour increments for the remainder of the data acquisition period.

Figure C.15 in Appendix C details the concrete placement, consolidation, finishing, and protecting for one of the instrumented pavement panels. The research team worked with Dolese Bros., one of the project industrial partners, to transition the research mixture designs to their automated batching system. They provided all the concrete for the pavement project.

A comparison of the shrinkage data from one of the Class A panels and one of the Eco-Pave-Crete panels is shown in Figure C.16 in Appendix C. This result is representative of all of the gauges within each panel. As the figure indicates, the Eco-Pave-Crete panel exhibited significantly less shrinkage compared to the Class A panel. This behavior is a direct result of the decreased cementitious content of the Eco-Pave-Crete mixture as well as the use of 10% of a Type K shrinkage compensating cement. The results fulfill the objective of the research project to develop a new generation of high performance concrete that has relatively low binder content and low risk of cracking.

4.2. Structural performance of reinforced concrete beams

The aim of this phase was to evaluate the flexural strength of reinforced concrete beams made with selected Eco-Bridge-Crete mixtures. The results were compared with those obtained from MoDOT reference mixture. The detail of the selected concrete mixtures used for reinforced concrete beams is given in Table C.1 in Appendix C.

The beam dimensions, reinforcement layout, and position of strain gauges are depicted in Figure C.17 in Appendix C. All beams were designed to be under reinforced (longitudinal reinforcement ratio = 0.72%), and had identical reinforcement layout. The beams were reinforced with three longitudinal #4 bars for tension, two longitudinal #3 bars for compression, and steel stirrups of #3. The side and vertical clear covers were kept constant at 25 mm (0.98 in.) for all the beams. Each beam measured 2.40 m (94.49 in.) in length with a cross section of 200 × 300 mm (7.9 × 11.8 in.). All of the beams had #3 stirrups spaced at 10 cm (3.94 in.) within the bearing area to prevent premature failure, as well as #3 stirrups spaced at 12.5 cm (4.9 in.) within the middle region. The longitudinal and shear steel reinforcements consisted of ASTM A615, Grade 60 material.

After assembling of reinforcement cages, the beam specimens were instrumented with different types of measurement devices in order to monitor global and local deformations and strains. The load is directly measured from the load cell of the actuators. All devices are connected to a data acquisition system capable of reading up to 120 channels. Two types of electrical resistance gauges were used to monitor local strains in the longitudinal reinforcing bars and concrete of the test beams. The strain gauges consisted of constantan foil with 120 ohm resistance and had a linear pattern (uniaxial) with various gauge lengths of 6 and 70 mm (0.2 to 2.8 in.). All beams were instrumented using three small strain gauges installed at longitudinal reinforcing bars located at the bottom at midspan as well as two long strain gauges placed on the top and lateral side of the concrete surface at the midspan. In addition to strain gauges, a linear variable displacement transducer (LVDT) was used to monitor vertical deflection of the test beam under flexural testing. A loading system with hydraulic jacks and a load cell of 500 kN (112.4 kips) (maximum capacity) closed-loop MTS actuator was used to test beams under four-point bending, as demonstrated in Figure C.18 in Appendix C. A displacement controlled mode at a rate of 1.2 mm/min was selected for applying the load. The actuator was supported by a steel frame and the load was transferred from the actuator to the tested beam through a steel spreader I-beam applied on the full width of the beam. A roller support was obtained by placement of a steel cylinder between two steel flat plates. A pin support was obtained by using specially adapted steel I-beam. The upper plate of the I-beam had a spherical groove and the plate was supported on the web plate which had a spherical end to house the plate and allow rotation. At each end of the tested beam, the roller and pin support were rested on a steel I-beam, which was secured on the rigid floor of the lab. The combination of the two point loads and the two supports resulted in the desired four-point loading system. During loading, the crack pattern on the sides of the beams was marked and recorded. The applied load, deflection, and strain readings were electronically recorded during the test using the data acquisition system monitored by a computer.

The beam was supported at two points 150 mm (5.9 in.) from the both ends and was loaded in the middle using two point loads separated by 460 mm (18.1 in.) , as shown in Figure C.19 in

Appendix C. The applied load was measured by the internal load cell on the actuator and the beams were instrumented with LVDT and strain gauges for steel reinforcement and concrete, as shown in Figure C.20 in Appendix C. The loading was stopped when the first crack appeared. The first crack appearance was manually monitored and the width of the major crack was measured using a hand-held microscope. The visual observation of crack development was followed up throughout the loading operation. The crack network distribution on the lateral surface of the beams was marked.

All concrete mixtures were made in a local concrete batching plant to confirm the ability of proposed concrete mixtures to apply under actual field conditions. The beam construction procedure is shown in Figure C.21 in Appendix C. Due to the incorporation of high-volume SCMs in proportioning of Eco-HPC mixtures, the beams were cured between 40-55 days using wet burlap and plastic sheet before testing. Concrete cylinders measuring 100×200 mm (3.9×7.9 in.) were prepared to evaluate the compressive strength of concrete mixtures used for beams. All samples were subjected to similar environmental condition to those of the concrete beams to simulate match curing condition. The compressive strength results of concrete mixtures are present in Table C.2 in Appendix C. Regardless of binder composition and fiber inclusion, all mixtures achieved target range of 40 to 50 MPa (5801.5 to 7251.9 psi) at the age of testing.

4.2.1. Flexural load-deflection response

The load-deflection responses of the reinforced concrete beams are shown in Figure C.22 in Appendix C. The load-deflection relationship is tri-linear for all beams. The initial part up to flexural cracking was similar for all beams, which represents the behavior of the uncracked beam that depends on the gross moment of inertia of the concrete cross-section. The second part, corresponding to post-cracking up to steel yielding, represents the cracked beam with reduced moment of inertia. The third part, corresponding to steel yielding up to failure, shows degradation in the stiffness of the beams due to yielding of the reinforcing steel. Regardless of the binder composition, all concrete beams made with relatively high volume SCMs exhibited approximately comparable ultimate load to that of the FA25 (MoDOT reference mixture). It is noticed that the incorporation of either 0.35% structural synthetic fibers or 0.35% recycled steel fibers led to higher ductility compared to the concrete beams made without any fibers. In other words, the use of fibers substantially improved the post-cracking behavior and enhanced energy absorption. This is attributed to the fact that the addition of fibers acts as an additional reinforcement for concrete to the rebar, where the fibers delayed yielding of steel bars compared to the case of concrete made without any fibers. The maximum load carrying capacity was attained for beams containing fibers, especially for the case of 0.35% recycled steel fibers combined with 7.5% CaO-based expansive agent (EX). This can be attributed to the wavy form of recycled steel fibers which can provide better bond to the paste matrix as well as higher tensile strength compared to the synthetic fibers. This made steel fibers effective in contributing to the tensile strength of the concrete beam. This tensile strength is added to that contributed by the reinforcing bars to obtain the ultimate capacity of the beam.

The results of ultimate load (i.e., maximum load) of the beams are presented in Figure C.23 in Appendix C. In all beams, the longitudinal tensile steel bars initially yielded followed by the concrete crushing, which is a ductile failure mode, called tension failure. It is interesting to note

that all beams made with optimized concrete mixtures containing more than 50% SCM replacements exhibited comparable ultimate load as that of the control beam made with MoDOT reference mixture (F25). All beams made with fibers exhibited slightly higher ultimate flexural strength compared to the similar beams without any fibers. However, given the relatively low volume fraction, the contribution of fibers to enhance ultimate load is not quite significant.

These results indicated that the use of recycled steel fibers can redistribute stresses and undergo multiple cracking before fiber pullout failure. However, non-fibrous beams underwent wider cracks and more crushing in their compression zones. The deflection-crack width propagation (major crack) of the tested beams is depicted in Figure C.24 in Appendix C. The crack width development of tested beam was found to vary with fiber addition and lightweight sand. For a given beam deflection, the use of recycled steel fibers significantly reduced the crack width in relation to that of the non-fibrous beams. Furthermore, the inclusion of lightweight sand was shown to improve the post-cracking response and decrease the crack width (given higher distribution of cracks). Such beams indicated smaller crack width and more distributed crack pattern in comparison with the control beam containing 25% FA replacement.

Figure C.25 in Appendix C compares the flexural toughness of RC beams up to the failure or 75 mm midspan deflection of the tested beams. The toughness was obtained by calculation of the surface area under the curve of load-deflection of the beam. The inclusion of either structural synthetic fibers or recycled steel fibers was shown to substantially enhance the toughness of the beam. For example, beams made with SL20FA35-7.5EX-0.35FT, SL60SF5-7.5EX-0.35FRW, and SL20FA35-7.5EX-0.35FRW concrete mixtures developed 120%, 135%, and 130% higher flexural toughness, respectively, compared to the control beam prepared with MoDOT reference mixture. The highest load carrying capacity was obtained for the concrete beam made with 60% slag and 5% SF replacements and having 0.35% recycled steel fibers. In the absence of fibers, all concrete beams made with 350 kg/m³ (22 lb/ft³) more than 50% OPC replacement exhibited comparable flexural toughness to that of the control beam prepared with 375 kg/m³ (23.41 lb/ft³) containing 25% FA replacement. Therefore, in spite of incorporating high volume SCM replacements (more than 50% OPC replacement), the use of fibers was shown to have good bond with the matrix, thus attaining load carrying capacity. This tensile strength is added to that contributed by the reinforcing bars to obtain the ultimate capacity of the beam.

University of Oklahoma

4.2.2. Beam shear test specimens

Structural performance testing of the bridge mixture designs involved shear and bond testing of full scale, reinforced concrete beam specimens. The following section discusses the design, fabrication, instrumentation, test procedure, and results for the shear testing phase. The experimental program consisted of nine identical beam specimens, three for each concrete type – Class A, Eco-Bridge-Crete 1, and Eco-Bridge-Crete 2. The beam span, cross section, and loading arrangement were chosen to maintain a slender beam with a shear span-to-depth ratio larger than 3.0, avoiding any deep beam effects. The beams measured 4267.2 mm (14 ft.) in length with a cross section of 304.8 x 5486.4 mm (12 x 18 in). The reinforcement was designed in accordance with *ACI 318-14 Building Code Requirements for Structural Concrete*. The longitudinal reinforcement consisted of 6 ASTM A615-09, Grade 60, deformed #7 bars. This amount of steel

was selected to provide a typical flexural reinforcement ratio as well as ensure a shear failure of the specimens. Each #7 bar contained a standard 90° hook at each end to prevent pullout in the event of longitudinal splitting cracks near the beam ends, which are common in beams that fail due to shear. Transverse reinforcement consisted of 15, ASTM A615-09, Grade 60, #3 U-shaped stirrups with standard 180° hooks. Stirrups were spaced 2 in. on center at the ends of the beam and 7 in. on center within the center portion of the beam. This reinforcement layout provided two shear test regions, with each region measuring approximately 1219.2 (4 ft.) in length and reinforced for flexure only (*i.e.*, no stirrups). Two ASTM A615-09, Grade 60, deformed #4 straight bars were placed at the top to anchor the stirrups and help stabilize the reinforcing cage. The strain gauges were installed to verify that a shear failure occurred prior to a flexural failure. Each gauge was attached to the reinforcing steel using cyanoacrylate adhesive and then wrapped in a butyl rubber tape and aluminum foil for protection during the concrete placement. The lead wires for the strain gauges were fed to the top of each cage and secured to the reinforcing steel with plastic ties. A data acquisition system monitored the strains in the reinforcing steel during the load test.

The Eco-Bridge-Crete mixtures were delivered by Dolese Bros. and placed into the beam forms using a concrete bucket, as shown in Figure C.26 in Appendix C. The beams were filled in two layers. After the first layer was poured, the concrete was vibrated to reduce air pockets and ensure proper consolidation. Once the last layer was poured and vibrated, the top was screeded and smoothed with finishing trowels, as shown in Figure C.27 in Appendix C. During the finishing process, steel hooks were vibrated into the top of the beams for transporting the specimens. The beams and companion small scale specimens were moist cured for 7 days.

A schematic of the test setup is shown in Figure C.28 in Appendix C. This third point loading arrangement results in two shear test zones that experience a constant shear force during loading. A photograph of a test specimen within the test fixture is shown in Figure C.29 in Appendix C. A 100-kip load cell was placed on top of the spreader beam to monitor the load being applied during the testing process. String pots were attached to metal angles adhered near midspan to monitor the beam's deflection. The load cell, two string pots, and two internal strain gauges were connected to a data acquisition system to monitor the test during loading.

The specimen test procedure involved applying load in increments of 44.48 kN (10 kips) up to a total load of 222.41 kN (50 kips). The load was then increased in increments of 22.24 kN (5 kips) until failure. After each load step, crack propagation patterns were traced and the end of each crack was labeled with the current load amount. Beam failure was determined when there was a significant drop in load, a loud audible crack, and visual observation of a failure mode. At this point, the data acquisition system was stopped, photographs were taken of the failure region, and the beam was removed from the test setup. A summary of the beam shear specimen test results is shown in Table C.3 in Appendix C, and a representative load-deflection plot is shown in Figure 4.1. All nine specimens displayed a large angled crack within the shear test regions, as shown in Figure 4.2, often accompanied by noticeable faulting at the crack location. This type of behavior is indicative of a shear failure, which was also confirmed by the load-deflection plots, which were always linear, and the strains in the longitudinal steel, which were always below the yield strain.

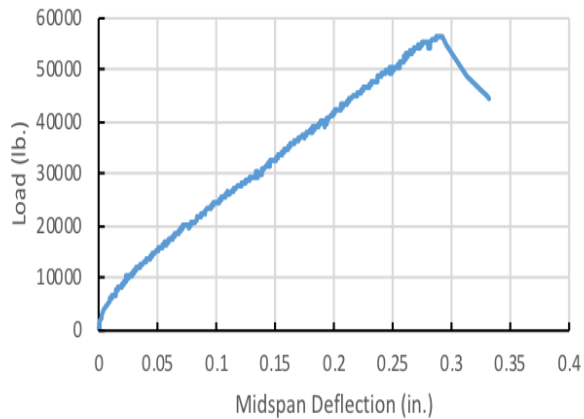


Figure 4.1. Typical beam shear test specimen load-deflection response



Figure 4.2. Typical beam shear test specimen failures

Table C.4 in Appendix C compares the failure loads from the tests with the shear capacities predicted by *ACI 318-14 Building Code Requirements for Structural Concrete*. Comparing the failure loads to the code values provides a normalization based on compressive strength, allowing a direct comparison between the three sets of specimens. The results indicate an increased capacity for the Eco-Bridge-Crete mixtures compared to the Class AA mixture, with the mixture containing both micro- and macro-fibers, Eco-Bridge-Crete Mixture No. 2, showing the greatest increase. However, both Kolmogorov-Smirnov and Anderson-Darling analyses showed that the differences between the results for the three mixtures were not statistically significantly different. In other words, the normalized shear capacities are essentially equal. Even with equivalent beam shear capacities, this result is still very positive in that the Eco-Bridge-Crete mixtures used 40% less cement and 12% less total cementitious material, yet still attained equivalent shear strengths.

4.2.3. Beam bond test specimens

Structural performance testing of the bridge mixture designs involved shear and bond testing of full scale, reinforced concrete beam specimens. The following section discusses the design, fabrication, instrumentation, test procedure, and results for the bond testing phase. The experimental program consisted of nine identical beam specimens, three for each concrete type – Class A, Eco-Bridge-Crete 1, and Eco-Bridge-Crete 2. The beam span, cross section, and loading arrangement were chosen to provide a realistic stress state within the splice test region of each specimen. The beams measured 3352.8 mm (11 ft.) in length with a cross section of 304.8 × 457.2 mm (12 × 18 in.). The reinforcement was designed in accordance with *ACI 318-14 Building Code Requirements for Structural Concrete*. The longitudinal reinforcement consisted of 3 ASTM A615-09, Grade 60, deformed #6 bars lap spliced at midspan of the beam. The length of the lap splice, set at 70% of the required development length, ensured a bond failure prior to yielding of the steel. Each #6 bar included a standard 90° hook at each end to prevent pullout. Transverse reinforcement consisted of 20, ASTM A615-09, Grade 60, #3 U-shaped stirrups with standard 180° hooks. Stirrups were spaced 2 in. on center at the ends of the beam and 7 in. on center within the remainder of the beam except within the splice test region. This reinforcement layout provided an unconfined splice test region at midspan. Two ASTM A615-09, Grade 60, deformed #4 straight bars were placed at the top to anchor the stirrups and help stabilize the reinforcing cage.

Prior to assembling the reinforcing cages, the bars within the splice test region were thoroughly cleaned of any rust and mill scale, as shown in Figure C.29 in Appendix C. After assembly of each cage, strain gauges were installed adjacent to the lap splice region. The strain gauges were installed to verify that a bond failure occurred prior to a flexural failure. Each gauge was attached to the reinforcing steel using cyanoacrylate adhesive and then wrapped in a butyl rubber tape and aluminum foil for protection during the concrete placement. The lead wires for the strain gauges were fed to the top of each cage and secured to the reinforcing steel with plastic ties. A data acquisition system monitored the strains in the reinforcing steel during the load test.

The Eco-Bridge-Crete mixtures were delivered by Dolese Bros. and placed into the beam forms using a concrete bucket, as shown in Figure C.30 in Appendix C. The beams were filled in two layers. After the first layer was poured, the concrete was vibrated to reduce air pockets and ensure proper consolidation. Once the last layer was poured and vibrated, the top was screeded and smoothed with finishing trowels. During the finishing process, pre-made steel hooks were vibrated into the top of the beams for transporting the specimens. The beams and companion small scale specimens were moist cured for 7 days.

A schematic of the test setup is shown in Figure C.31 in Appendix C. This third point loading arrangement results in two shear test zones that experience a constant shear force during loading. A photograph of a test specimen within the test fixture is shown in Figure C.32 in Appendix C. A 100-kip load cell was placed on top of the spreader beam to monitor the load being applied during the testing process. String pots were attached to metal angles adhered near midspan to monitor the beam's deflection. The load cell, two string pots, and two internal strain gauges were connected to a data acquisition system to monitor the test during loading.

The specimen test procedure involved applying load in increments of 4535.92 kg (10 kips) up to a total load of 13607.77 kg (30 kips). The load was then increased in increments of 2267.96 (5 kips) until failure. After each load step, crack propagation patterns were traced and the end of each crack was labeled with the current load amount. Beam failure was determined when there was a significant drop in load, a loud audible crack, and visual observation of a failure mode. At this point, the data acquisition system was stopped, photographs were taken of the failure region, and the beam was removed from the test setup. A summary of the beam splice specimen test results is shown in Table C.5 in Appendix C, and a representative load-deflection plot is shown in Figure C.33 in Appendix C. All nine specimens displayed a splitting failure within the lap splice region, as shown in Figure C.34 in Appendix C, often accompanied by debonding of the concrete immediately below the lap splice location. This type of behavior is indicative of a splitting bond failure, which was also confirmed by the load-deflection plots, which were always linear, and the strains in the longitudinal steel, which were always below the yield strain.

Table C.6 in Appendix C compares the normalized bond stresses from each of the nine splice test specimens. The normalizations are used to directly compare specimens with different compressive strengths. A normalization based on square root of the compressive strength is based on the development length equations from ACI 318-14. A normalization based on fourth root of the compressive strength is based on recommendations from ACI Committee 408. Both methods indicate that the Eco-Bridge-Crete Mixture No. 1 has an increased bond strength compared to the Class AA mixture. However, statistical analyses indicate that the increase is not statistically significant. However, the results also indicate that the Eco-Bridge-Crete Mixture No. 2 suffered a noticeable decrease in bond strength compared to the Class AA mixture, which was found to be statistically significant. Forensic examinations of the specimens showed areas where the macro-fibers caused internal honeycombing around the splice region, which decreased the bonded portion within the splice zone.

5. LIFE CYCLE COST ANALYSIS

5.1. Introduction

Thousands of existing structures in the U.S. are in need of condition assessment and renovation. In the 2013 Report Card for American's Infrastructure published by the American Society of Civil Engineering (ASCE), majority of the groups of infrastructure systems (bridges, rail, roads, etc.) fell below a C grade (Herrmann 2013). An estimated investment of 3.6 trillion dollars is estimated to be needed by 2020 to bring the nation's infrastructure to a grade of C or better based on the same report. Aging facilities, growing technical and environmental requirements of the transportation infrastructure, and increasing costs associated with maintenance and repair has led agencies to seek development of innovative materials for construction and maintenance, as well as reliable decision-making tools for cost-effective transportation management and investments.

The sustainability of our urban transportation infrastructure depends on the adoption of new construction materials and technologies with great promise for improved performance and productivity. However, most of the agencies would like to know life cycle costs of these new construction materials and technologies before they can replace the traditional ones. Life Cycle Cost Analysis (LCCA) is an effective tool that can assist decision-makers in the development of optimum investment strategies by accurately assessing internal and external costs of transportation projects while satisfying agency budget constraints. The RE-CAST research team aims to provide multi-scale and multi-disciplinary studies to fast-track the acceptance of the new generation of cement-based materials to achieve a more sustainable transportation infrastructure. Such new generation innovative materials will have several advantages over conventional materials such as more cost-effective and longer service life, more efficient use of resources and in construction operations, and minimizing construction duration and traffic delays using certain construction methodologies. But it remains a challenge to reliably estimate their costs and life time performance due to very limited "*field implementation*" data. In light of all these complications, this section presents the research effort of conducting life cycle cost analysis for both conventional and new-technology materials to support decision making, considering agency, user, as well as society costs. The proposed approach will specifically try to link the new construction materials and technologies' laboratory-measured data with actual field performance data to overcome the challenges of limited data.

Two different approaches are proposed: 1) Apply a hypothesized improvement rate to the deterioration functions of existing and well-known materials to represent the expected improved performance of a new material compared with a conventional material with relatively similar characteristics; 2) Utilize a correlation function between the results of laboratory tests and field performance of known materials to predict the expected performance of a new material based only on the data from its laboratory tests. Both methods are treated probabilistically to be able to deal with the high level of uncertainty due to the length of analysis period, as well as the lack of real-world performance data, especially in the case of novel materials. In addition, a web-based user-friendly LCCA software tool developed to make use of the existing network-wide data and deterioration models is also briefly discussed. This new software tool will allow prospective

users to perform this novel LCCA methodology for more effective decision making and resource allocation. This section is concluded with an LCCA example for one of the new materials developed in this project, which was conducted by New York University.

5.2. Literature review

In 1998, an interim Federal Highway Administration (FHWA) technical bulletin (FHWA 1998), "Life-Cycle Cost Analysis in Pavement Design," was developed under FHWA Demonstration Project 115. This report recommends step-by-step procedures for conducting life cycle cost analysis at the project level and has become the agency's guidance document for LCCA. It is still one of the most referenced documents in the LCCA literature. One of its most important contributions was the user cost calculations and the introduction of reliability concepts for LCCA via the use of Monte Carlo simulation. In August 2002, FHWA published another important document, "Life-Cycle Cost Analysis Primer" (FHWA 2002) followed by the development of RealCost software (FHWA 2004). Both of them are intended to provide sufficient background and training for transportation officials to properly use LCCA for evaluating transportation project alternatives.

FHWA and State Highway Agencies (SHAs) recommend LCCA as an important technique for supporting transportation investment decisions. LCCA can be used to evaluate design, maintenance, and preservation strategies for all types of assets, such as pavement or bridges. Guided by FHWA, SHAs along with MAP-21 (USDOT 2012), many state departments of transportation (DOTs) incorporated life cycle cost consideration in their decision making process and transportation asset management.

Table 5.1 shows a brief summary from seven states in terms of the analysis period used for pavement or bridges, discount rate, evaluation methods, consideration of probabilistic approach and user cost (VDOT 2011, Caltrans 2013, Ozbay et al. 2002, FDOT 2013, Luhr 2015, ODOT 2014, CDOT 2015).

Table 5.1. Summary of seven state DOTs LCCA practices

State DOT	Analysis period (years)	Discount rate	Evaluation methods	Probabilistic approach	User cost
VDOT	Pavement: 50	4%	PV/EUAC	No	No
CalTrans	Pavement: 20, 35, 55	4%	PV/EUAC	No	Yes
NJDOT	Pavement: 35-40	Probability distribution	NPV/EUAC/B/C/IRR	No	Yes
	Bridges: >=75			Yes	Optional
FDOT	Pavement: 40	3.5%	PV	No	Yes
WSDOT	Pavement: 50	4%	NPV/EUAC	No	No
ODOT	Pavement: 35	OMB discount rate	PV	No	Yes
CDOT	Pavement: 40	2.6%	PV	No	Yes

Note: PV = Present Value, EUAC = Equivalent Uniform Annual Costs, NPV = Net Present Value, B/C = Benefit/Cost, IRR = Internal Rate of Return

Numerous studies have applied LCCA to roads and bridge structures in terms of maintenance and replacement strategies or management tools in the last two decades, however, not much work has been conducted dealing with new construction material/technology and conventional materials/technology. Table 5.2 lists six studies involving new technology or materials (Ehlen 1997, Horvath 2004, Keoleian et al. 2005, Cusson, Lounis, and Daigle 2010, Eamon et al. 2012, Soliman and Frangopol 2014). Clearly, there are not many studies that have applied probabilistic approach to deal with the high uncertainty that new materials or construction technologies carry.

Table 5.2. Literature review on new construction materials and technologies

Study	New material/design	Applications	Agency cost	User cost	Social cost	Probabilistic	New material future performance
Ehlen, 1997	Fiber-reinforced polymer composites	Bridge deck	Yes	Yes	No	No	State DOT Estimates and Research Model
Horvath, 2004	Recycled materials	Pavement	Yes	Yes	Yes	No	Model
Keoleian et. al, 2005	Engineered cementitious composite	Bridge link slab	Yes	Yes	Yes	No	State DOT Estimates
Cusson et al., 2010	High-performance concrete	Bridge deck	Yes	No	No	No	Model
Eamon et. al, 2012	Carbon fiber reinforced polymer	Bridge superstructure	Yes	Yes	No	Yes	State DOT practices
Soliman and Frangopol 2014	Corrosion-resistant steel	Steel bridge	Yes	Yes	Yes	Yes	Assumption

In addition, various LCCA tools have been developed to help decision makers to perform LCCA easier and to make more informed decisions by better understanding each project's future maintenance and replacement requirements. Most of the current LCCA tools are spreadsheet based. Although most of the potential users are familiar with spreadsheet calculations, spreadsheet-based LCCA software programs can be quite limited due to the following reasons: 1) Inputting data for each individual scenario can be very labor intensive, 2) No online resources or databases will be available when using off-line spreadsheet based models, 3) Usually not capable for performing complicated and computationally demanding calculations involving stochastic user or society costs. In order to overcome these limitations, NYU team developed a highly interactive web-based tool.

5.3. LCCA general cost function and implementation procedure

Project-level LCCA is performed by summing up the monetary equivalent of all benefits and costs at their respective time of occurrence and are converted into a common time dimension so that different alternatives can be compared correctly. A general expected life-cycle cost up to time, T , of known conventional material, $LCC(T)$, can be expressed as below:

$$LCC(T) = C_C + C_M(T) + C_R(T) + C_U(T) + C_S(T) + SV \quad (5.1)$$

where LCC is the Life-Cycle Cost (dollars), C_C is the Construction Cost (dollars), C_M is the Maintenance and repair Cost (dollars), C_R is the Rehabilitation Cost (dollars), C_U is the User Cost (dollars), C_S is the Socio-economic Cost (dollars), SV is the Salvage Value (dollars), T is the Time (year).

Figure 5.1 illustrates the objective function of LCCA and its general input parameters, as well output cost components at the project level.

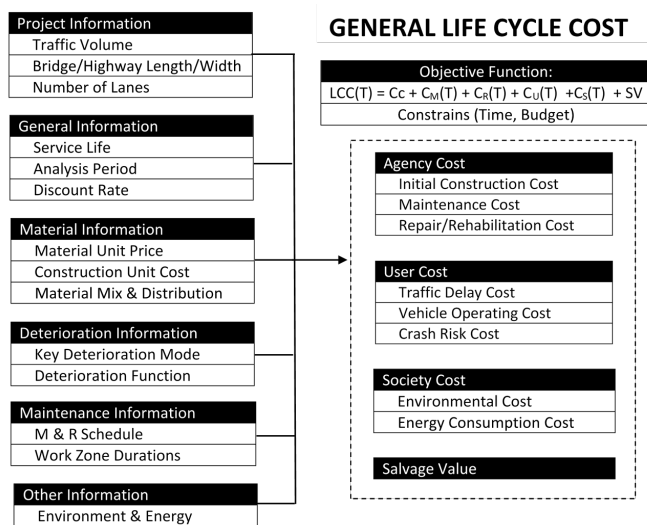


Figure 5.1. General LCCA inputs and outputs (Ozbay and Gao, 2016)

Life-cycle and expenditure stream diagrams shown below (Figure 5.2) illustrate the cost timeline of two alternatives. For the transportation infrastructure, this usually includes the initial construction cost, the maintenance and rehabilitation costs, the costs encountered by the user and the society, and the salvage value.

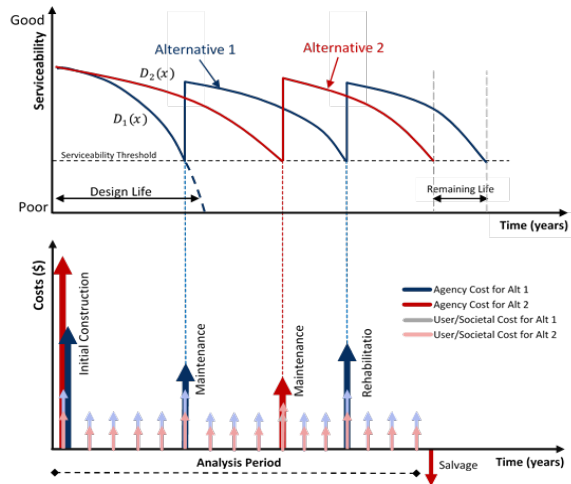


Figure 5.2. Life-cycle of two alternatives and corresponding expenditure stream diagram (Jawad 2003)

After constructing the expenditure stream, computing the life-cycle cost (i.e., using Net Present Value (NPV) method) of each alternative becomes a straightforward calculation. It is advisable to compute agency, user, and society costs in a separate manner, before computing the total life cycle cost, to better understand the exact contribution of each cost category to the total final worth (Jawad 2003). Generally, an alternative is preferred if its NPV is less a minimum of 10% than the NPV of other competing alternatives (Jawad 2003). If the NPV difference between two alternatives is less than 10%, then such alternatives are considered similar or equivalent.

As most of the LCCA parameters, such as discount rate, traffic growth rate, and material unit cost, are uncertain, these uncertainties demand the use of a probabilistic approach to accurately quantify LCCA. By identifying and addressing those uncertainties, a reliable probabilistic life-cycle cost analysis can thus be performed. The probabilistic approach is strongly recommended in the case tackled by this project because the cost and technical performance of new-technology and/or materials are highly uncertain.

5.4. Deterioration models

Deterioration models are used to predict future conditions and to trigger preservation work based on the conditions. In order to perform a LCCA, one needs data and models about the deterioration process. One of the major factors in a reliable LCCA is the availability of accurate predictive models that describe the future deterioration rate of the transportation infrastructure. In brief, deterioration is a function of environmental effects and structural loading, and involves various factors in LCCA. It is usually influenced by:

- Material type
- Construction techniques
- A mixture of material type and construction techniques

- External factors such as number of freeze/thaw cycles, amount of salt used, traffic demand and loads and etc.
- Maintenance factors such as type and frequency of maintenance treatments

Generally, the rate of deterioration is expected to gradually increase with time. That is to say, the operating condition is expected to decrease with time. The condition of the infrastructure is restored after maintenance and repair activities and then starts to deteriorate again, though it may be at a different deterioration rate, based on the material type and construction technology used in the maintenance and repair stages. A typical deterioration curve is shown at the upper portion of Figure 5.2. By monitoring the specific infrastructure element's condition, the expected service life, defined as the number of years when its condition reaches a predefined threshold such as minimum acceptable operating condition, can be estimated. The shape of the deterioration curve relies on various condition states. Once the deterioration model is fed into the life cycle cost expenditure stream diagram (Figure 5.3), it determines when to perform maintenance and repair activities. Then, their associated costs can be computed accordingly.

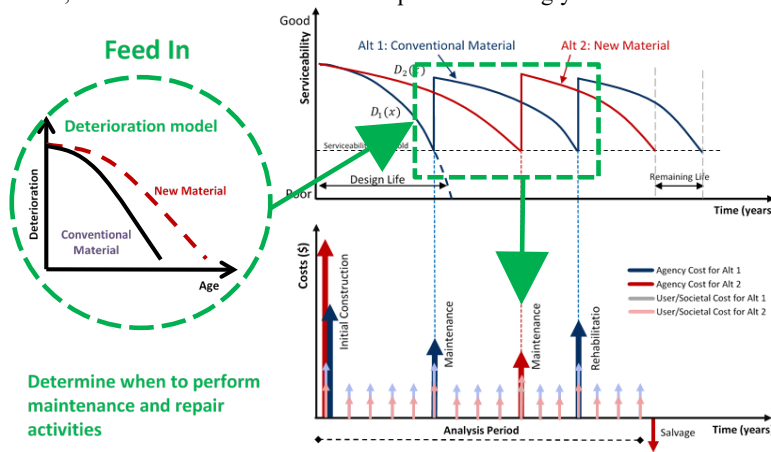


Figure 5.3. Deterioration model and life cycle cost expenditures

5.5. Proposed methodology

Clearly, it is not a trivial task to predict the actual field performance of a new construction material or technology that has either been tested in a laboratory environment or undergone a very limited field deployment only. Its performance prediction must thus rely on these limited laboratory tests or deployment results combined with expert opinion for the most likely values of its behavior under real-world conditions. This approach increases the uncertainty of such predictions. As a result, these uncertainties demand the use of a probabilistic approach to appropriately apply LCCA. Furthermore, the fact that these uncertainties can also vary in time creates the need for a robust stochastic treatment of the individual scenarios that will be evaluated as part of the proposed LCCA methodology.

It is not easy to predict the field performance of such materials due to lack of minimum amount of data. As more information and field data becomes available, the proposed approach should be re-evaluated and improved.

In light of all these complications, two different approaches are proposed: 1) Apply a hypothesized improvement rate to the deterioration functions of existing and well-known materials to represent the expected enhanced performance of a new material compared with a conventional material with relatively similar characteristics; 2) Utilize the correlation function between the results of laboratory tests and field performance of known materials to predict the expected performance of a new material based only on its laboratory tests. Figure 5.4 shows the flowchart of these two proposed approaches.

5.5.1. Approach I – Improvement rate

Novel construction materials or technologies are expected to offer improvements, such as extended service life, compared with conventional materials or technologies. This approach is proposed to estimate the expected improvement rate of new materials or technologies by comparing them to conventional materials or technologies via laboratory tests.

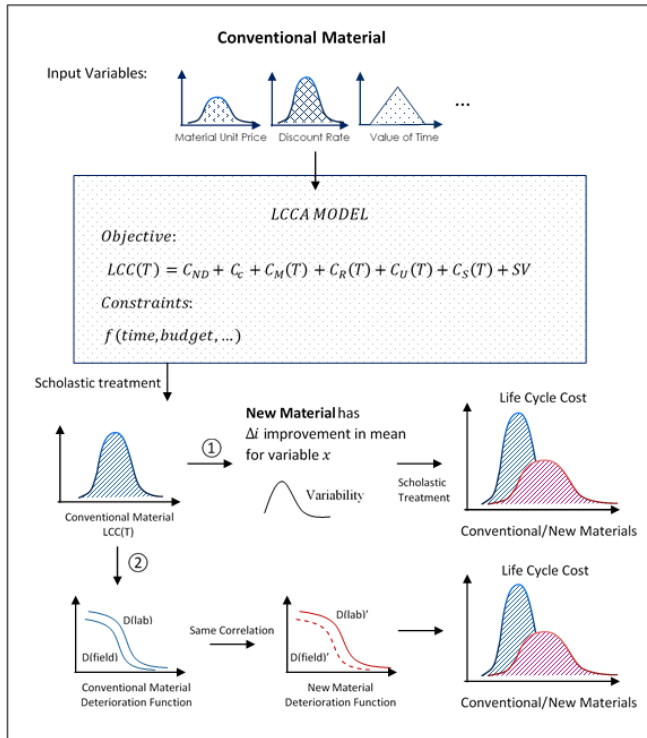


Figure 5.4. Two proposed approaches for estimating predicted deterioration functions of a new material or a novel construction technology

Deterministic Approach

Estimated values or models based on historical data are often used as input to life-cycle analysis when quantifying costs. However, for a new material or construction technology, there may not be adequate data to accurately describe its real-world performance. An interim solution is to define metrics for the new material or technology as a percent improvement rate with respect to a current conventional material or technology with a known performance function. Then, this percent improvement rate is applied deterministically (or probabilistically) to this known performance function.

A new material is herein taken as an example. The relationship between this new material’s deterioration function and conventional deterioration function is expressed using the equation below. It is assumed that the deterioration function of the new material will follow the same “shape” as that of the well-known conventional material. However, this shape will be shifted to represent the enhanced performance of the new material. Figure 5.5 shows an example that turns results from laboratory tests into the improvement rate by employing this approach. The laboratory improvement rate, which is denoted by β , can be a single fixed value that is most

likely to occur when using the deterministic approach. The correction factor, k , is applied to generate estimates when applying laboratory improvement rate to field.

$$F(x) = k \cdot f(\beta x) \quad (5.2)$$

where $F(x)$ is the new material deterioration function, $f(x)$ is the conventional material deterioration function, β is the laboratory improvement rate, k is the correlation factor.

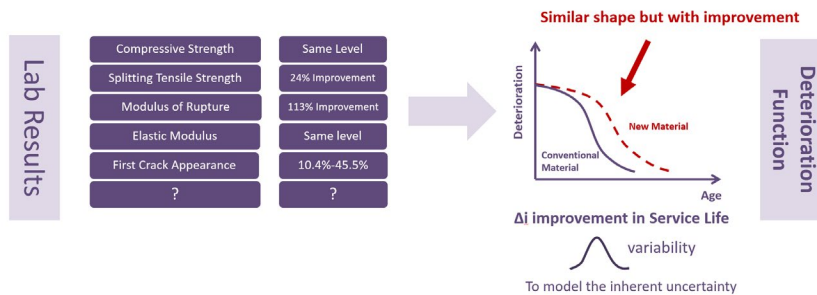


Figure 5.5. Using laboratory results to update a deterministic deterioration function

Probabilistic Approach

LCCA has many variables in its objective function that might be difficult to predict with certainty even in the case of the well-known materials/situations. Usually, time sensitive variables such as “discount rate” or “loads” are treated as random variables. However, in the cases of new materials and /or innovative construction technologies that have never been field tested or that have been recently deployed, the need for capturing uncertainties can be even more important. The goal is to determine how this stochasticity affects the sensitivity or prediction reliability of the total life cycle cost of each alternative. Many techniques, such as Monte Carlo simulation and Latin Hypercube method, can be applied to quantify the effect of uncertainty propagating from non-deterministic variables. The aim of such treatment is to repeatedly generate random samples from one or more given probability distribution(s), each representing a specific variable, and to estimate the expectation of the total life cycle cost for these specific distribution(s). Probabilistic LCCA can be performed according to the following steps:

- (1) Decide on the operation level: Network level or Project level?
- (2) Determine LCCA objective and alternatives.
- (3) Identify general project information, construction type and road type.
- (4) Determine timing of required activities.
- (5) Determine the input parameters that carry inherent variability in their values that will be treated probabilistically in the study.
- (6) Identify or develop a probability distribution that most closely matches the available data, or best represents current state of knowledge.
- (7) Perform scholastic treatment (e.g. Monte Carlo simulations) to assign random values to the input parameters from a selected probability density function.
- (8) Decide the number of iterations and convergence tolerance. Each iteration will result in a value for the life-cycle cost, and these values will be used to construct the probability

distribution of the final outcome. Enough iterations should be performed until the simulation converges and any additional iteration has little effect on the final distribution.
 (9) Evaluate and interpret the outcome - the probabilistic distribution of total life-cycle cost.

After implementing the stochastic treatment described above, the final outcome will be a probability distribution or a cumulative probability distribution of the life-cycle costs for each alternative (Figure 5.4). Generally, wide distributions indicate high uncertainty in the parameter values while narrower distributions indicate less uncertainty.

5.5.2. Approach II – Correlation method

There has been some recent research efforts conducted to develop “performance tests” that can link performance of parameters measured in the laboratory to actual field pavement or bridge performance (Dave 2011). This proposed approach is focused on such a correlation methodology between the laboratory test results and the available correlation values from published data, based on the actual field performance. If a correlation function between laboratory and field performance of a well-known material exists, one can assume that this relationship will remain the same for the new material as well. This same correlation function can be used to estimate the field performance of new material. This correlation function may include coefficient of thermal contraction, Poisson’s ratio, complex modulus, resilient modulus, relaxation modulus and so on. The functional specifications of the known deterioration function of conventional material and estimated deterioration function of new material are depicted using the following equations:

$$D(f_c) = D(l_c) \times f_{corr} \tag{5.3}$$

$$D(f_n) = D(l_n) \times f_{corr} \tag{5.4}$$

where $D(f_c)$ is the field deterioration of conventional material, $D(l_c)$ is the laboratory deterioration function of conventional material, $D(f_n)$ is the field deterioration of new material, $D(l_n)$ is the laboratory deterioration function of new material, f_{corr} is the correlation function of model

Suppose the comparison of a known conventional material M_1 that has some similar characteristics with the proposed new high-performance material M_2 . If the laboratory deterioration function $D(l_n)$ is known for the proposed new material, M_2 , a field deterioration function $D(f_n)$ from the correlation function f_{corr} can be inferred (Figure 5.6).

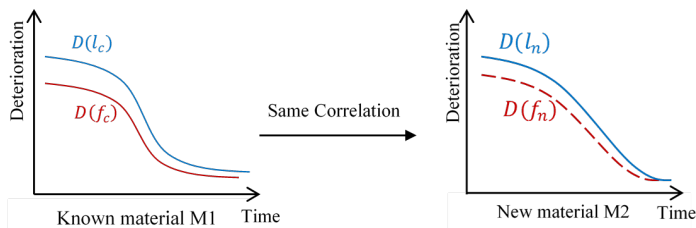


Figure 5.6. Illustration of the proposed correlation method to quantify time-dependent deterioration behavior of new and known materials

5.6. LCCA example: economical and crack-free high performance concrete (Eco-HPC)

The following section illustrates the application of the LCCA approach to this project, the Economical and Crack-free High Performance Concrete with Adapted Rheology developed by Missouri University of Science and Technology (Missouri S&T)¹. Eco-HPC concrete can be applied to pavement, bridges, and other infrastructures with relatively high resistance to early-age shrinkage cracking. Two classes of Eco-HPC are designed for the following applications: HPC for pavement construction (Eco-Pave-Crete) and HPC for bridge deck and transportation infrastructure construction (Eco-Bridge-Crete). Both HPC mixtures should develop high resistance to early-age cracking to limit the crack width to hairline cracks as 0.1 mm (0.004 in.). The rheological properties of these advanced materials will be designed to facilitate construction operations and reduce labor and cost. Both Eco-HPC types will also be designed to ensure high durability. The following highlights potential improvements of the Eco-HPC concrete compared with typical MoDOT mixture (1).

- Decrease of construction time, labor, and equipment needed on construction sites
- Extend the time of crack initiation, crack propagation, and better durability aspects
- Significant noise reduction: Little or no vibration required
- Improved health and safety
- CO₂ emission reduction from 745 kg/ton to 540 kg/ton
- 50% lower embodied energy consumption and 50% lower global warming potential

Hypothetical LCCA examples for bridge deck and pavement are built, based on this information using the improvement rate approach introduced in the previous sections.

5.6.1. User & societal costs

In this example, only the differential user and societal costs that are expected to occur during work zone periods are computed. Note that although including user costs is noted as a best-practice by the FHWA, it could greatly dominate total life-cycle costs, especially in the case of urban projects. It is suggested by the Illinois Department of Transportation (IDOT) (Holland 2012) to use a weighted factor (0.3 in this example) for the user cost when calculating the total life cycle cost.

5.6.2. Energy consumption and global warming potentials (GWPs)

The incorporation of high volume supplementary cementitious materials (SCMs) can contribute to significant reductions in CO₂ emissions and embodied energy. The optimal concrete mixtures develop 40% lower embodied energy consumption and GWPs for the pavement application and

¹ Email correspondence with Missouri S&T: 7/24/2016-Received Project Survey; 7/30/2016-Received additional Information about performance measures; 11/4/2016-Received information about shrinkage and structural performance of large elements; 11/22/2016-Received service life information of current Missouri bridge decks; 2/21/2017-Received supplemental information about Missouri pavement and bridge; 3/6/2017-Received energy consumption and global warming potential information.

Commented [OHC(1): why early age? shouldn't the cracks be limited in width during the service life?

55% lower embodied energy consumption and GWPs associated with material manufacturing, transportation, and concrete production with respect to the MoDOT reference mixture (Mehdipour 2016). Using recycled steel wires that are recovered from scrap tires can also be effective in reducing pollution resulting from the manufacturing of brand new steel fibers. As one type of economic evaluations that can be carried out as part of conducting LCCA, cost-effectiveness analysis (CEA) can be a useful concept to evaluate energy consumption or emission reduction strategies, not only based on their reduction potential, but also based on the relative cost of that reduction. The following equation provides the basic relationship between costs, emissions, and cost-effectiveness (CE) (Santero, Loijos, and Ochsendorf 2013). The same method can be applied to energy consumption as well. The “new” and “con” subscripts refer to the new technology/material alternative and conventional technology/material case, respectively.

$$CE_{new} = \frac{\text{cost}_{new} - \text{cost}_{con}}{\text{emissions}_{new} - \text{emissions}_{con}} = \frac{\Delta \text{cost}_{new-con}}{\Delta \text{emission}_{new-con}} \quad (5.5)$$

Figure 5.7 shows the variation in primary energy consumption (PEC) and global warming potential (GWP) with different mixtures (Mehdipour 2016). By applying equation (5) for GWP reduction strategies, the cost effectiveness of alternative A2, the optimized mixture for bridge, is 0.11 (\$/lb CO₂-eq reduced), meaning that the new alternative A2 would cost \$0.11 for every pound of carbon dioxide equivalent reduced. For the alternative B2, the optimized mixture for pavement, the cost effectiveness is estimated as 0.23 (\$/lb CO₂-eq reduced). Similarly, for energy consumption reduction strategies, the cost effectiveness values for alternatives A2 and B2 are estimated as 21.40 (\$/GJ reduced) and 63.64 (\$/GJ reduced), respectively.

Table 5.3 presents the input information. The traffic data is obtained from one of the I-80 highway section in New Jersey, 0.7 mile east of Passaic River, for demonstration purposes only. For bridge deck, the estimated improvement rate of the Eco-Bridge-Crete service life is based on a combination of compressive strength, modulus of elasticity, shrinkage, durability factor, and cracking resistance laboratory improvement and large-scale structural performance. It is applied to Stage 1 (conditional rating 9-6) of deck deterioration as the Eco-Bridge-Crete mixtures will significantly increase the crack and propagation resistance, toughness, and long-term durability. For the pavement, the estimated improvement rate is based on a combination of compressive strength, modulus of elasticity, bulk resistivity, shrinkage, durability factor, and cracking resistance laboratory improvement. It is applied to both service life and rehabilitation extended service life. A 20% saving in labor cost is assumed when estimating the construction unit Cost of the new material in both cases. These values will be further evaluated once field implementation data becomes available. The deterministic LCCA output is shown in Table 5.4. Besides agency cost, traffic delay, vehicle operating, crash risk, and air pollution costs are included in this example as well. Please refer to the full report for the description of detailed methodology of user and societal costs.

5.6.3. Agency costs

In this example, agency costs include initial construction, maintenance, and rehabilitation costs as well as the salvage value. For the bridge deck, the rehabilitation cost can be broken down into four categories (NJDOT 2015): a) the cost of replacing the structure (include demolition and

traffic control), b) approach roadway work, c) traffic staging and d) preliminary engineering. Rehabilitation cost is assumed to be 1.8 times the new bridge initial construction cost. Maintenance cost is assumed to be 5% of the initial construction cost. For pavement, miscellaneous mobilization, and preliminary engineering costs are assumed to be 20%, 5%, 9.5% for initial construction and 9.5%, 1.9%, 9.5% for rehabilitation (Missouri Department of Transportation 2004), respectively. Maintenance costs for both alternatives are assumed to be the same over the entire design lives so they are not input into the LCCA for the pavement example. Salvage value is the value of an investment alternative at the end of the analysis period. This is usually included as a benefit or negative cost in agency cost.

Table 5.3. LCCA example work flow – inputs

I. Analysis options	Alt A1: Conventional Concrete Bridge	Alt A2: Eco-Bridge-Crete	Alt B1: Conventional concrete pavement	Alt B2: Eco-Pave-Crete
1. Service life (years)	45	60	25	33
2. Analysis period (years)	75	75	45	45
3. Discount rate (%)	3.0%	3.0%	3.0%	3.0%
4. Material unit price (\$/CY)	72*	94*	45*	66*
5. Construction unit cost (bridge feck: \$/SF, pavement: \$/SY)	114.17*	128.00	53.00*	69.56
II. Traffic data				
Average daily traffic (veh/day):	114,739		114,739	
Trucks as percentage of ADT (%):	1.55%		1.55%	
Annual growth rate of traffic (%):	0.5%		0.5%	
Lanes opened under normal condition:	Inbound (4), outbound (5)		Inbound (4), outbound (5)	
Value of time (\$/hr):	11.58 (Passenger car), 20.43 (Truck)		11.58 (Passenger car), 20.43 (Truck)	
III. Work zone input				
Maintenance schedule:	Every 5 years	Every 5 years	Maintenance schedule/cost are assumed to be the same for both alternatives and are neglected in this study	
Rehabilitation/replacement schedule:	Every 45 years	Every 60 years	Time to first rehabilitation: 25 years (rehabilitation extended service life: 20 years)	Time to first rehabilitation: 33 years (rehabilitation extended service life: 26 years)
Maintenance duration (days):	10	10	N/A	N/A
Rehabilitation duration (days):	120	108	30	27
# lanes opened during maintenance/rehab:	2 lanes/1 lane	2 lanes/1 lane	2 lanes	2 lanes
Free flow speed (mph):	70	70	70	70
Work zone speed-maintenance (mph):	50	50	50	50
Work zone speed-rehabilitation (mph):	30	30	30	30
III. Estimated improvement rate nased on naboratory results				
Bridge deck: Since the Eco-Bridge-Crete mixtures will significantly increase the crack and propagation resistance, higher toughness, and long-term durability, the research team applied the estimated improvment rate 50% to Stage 1 (rating 9-6) of deck deterioration.				
Pavement: The research team applied the estimated improvment rate 30% to both service life and rehabilitation extended service life.				

*Price reference: (FHWA 2011, Mehdipour 2016)

Table 5.4. LCCA example work flow – deterministic outputs

I. Agency cost (\$)	Alt A1: Conventional Concrete Bridge	Alt A2: Eco-Bridge-Crete	I. Agency cost (\$)	Alt B1: conventional concrete pavement	Alt B2: Eco-Pave-Crete
Initial construction cost (\$):	3,108,020	3,484,505	Initial construction cost (\$):	322,748	355,396
Maintenance cost (\$):	852,457	955,718	Maintenance cost (\$):	Maintenance cost are assumed to be the same for both alternatives and are neglected in this study	
Rehabilitation cost:			Rehabilitation cost:		
(A) Replace the structure (\$):	1,083,799	779,915	(A) Slab replacement (1.5%) (\$):	7,430	5,958
(B) Approach roadway work (\$):	68,520	38,996	(B) Treatment -diamond grinding (\$)	6,896	5,444
(C) Traffic staging (\$):	287,783	163,782	(c) miscellaneous & mobilization (\$)	2,067	1,645
(D) Preliminary engineering (\$):	143,892	81,891	(d) preliminary engineering(\$)	1,723	1,371
Total rehabilitation cost (s):	1,479,385	1,064,585	Total rehabilitation cost (s):	18,116	14,419
Salvage value (\$):	-203,162	-512,487	Salvage value (\$):	0	-39,871
Total agency cost (\$):	\$5,236,700	\$4,992,321	Total agency cost (\$):	\$340,864	\$329,945
ii. User cost (\$)			ii. User cost (\$)		
Traffic delay cost (\$):	\$25,732,076	\$19,216,750	Traffic delay cost (\$):	\$1,387,082	\$1,281,998
Vehicle operation cost (\$):	\$1,727,985	\$1,280,384	Vehicle operation cost (\$):	\$117,318	\$100,305
Crash risk cost (\$):	\$25,153	\$15,659	Crash risk cost (\$):	\$10,279	\$7,600
Total user cost (\$):	\$25,161,738	\$20,512,793	Total user cost (\$):	\$1,514,679	\$1,389,903
iii. Social cost (\$)			iii. Social cost (\$)		
Air pollution cost (\$):	\$7,307	\$4,549	Air pollution cost (\$):	\$2,986	\$2208
Total social cost (\$):	\$7,307	\$4,549	Total social cost (\$):	\$2,986	\$2,208
Iv. Total life cycle cost	\$13,489,571	\$11,256,927	Iv. Total life cycle cost	\$798,254	\$749,123
Alt a2: eco-bridge-crete benefit:	Total life cycle cost: -17.34% Agency cost: -4.67%, user cost: -25.37%, social cost: -37.74% (user cost factor: 0.3, social cost factor: 1.0)		Alt b2: Eco-Pave-Crete benefit:	Total life cycle cost: -6.15% Agency cost: -3.20%, user cost: -8.24%, social cost: -26.06% (user cost factor: 0.3, social cost factor: 1.0)	

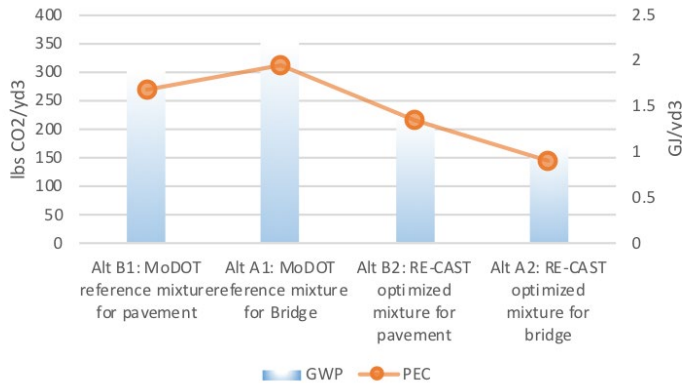


Figure 5.7. Variation in embodied energy and GWP with different mixtures (Mehdipour 2016)

The final deterministic LCCA results, given in Table 5.4, show that the application of the new material will save 4.67% of agency costs and 17.34% of total life cycle cost for the bridge deck, and will save 3.20% of agency cost and 6.15% of total life cycle cost for the pavement. If only agency costs are evaluated, alternatives can be considered similar or equivalent because the difference between agency costs of alternatives is less than 10%. However, the benefit in user costs especially in the case of the the bridge deck rehabilitation / replacement and potential energy consumption and GWP savings play an important role and should not be ignored. On the other hand, sensitivity analysis should be conducted if the deterministic approach is adopted in conducting LCCA. The sensitivity analysis will be able to examine the effect of the variability in the main input parameters and can be accomplished by performing the analysis over a range of possible values of the same input parameter being tested while holding all other parameters constant (Jawad 2003). Figure 5.8 shows the results of the sensitivity analysis of applying different user cost weights in the bridge deck example.

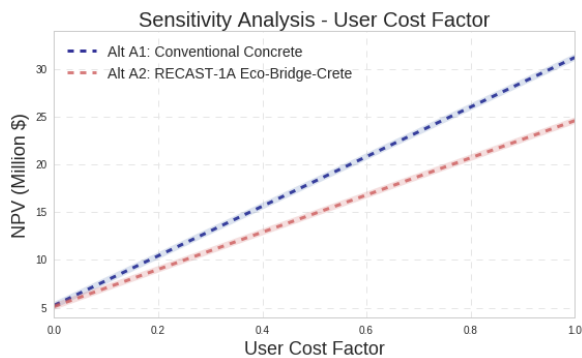


Figure 5.8. Sensitivity analysis example (Estimated weight of user cost)

In contrast to the deterministic approach, probabilistic approach (Figure 5.9) provides additional capabilities that allows the analyst to quantify parametric variation and uncertainty. Moreover, instead of fixed LCC values, the output can be represented as probabilistic distributions. The following figure shows the total life cycle cost of two alternatives for the bridge deck application. Let's assume that the construction cost for the alternative A1 conventional material follows a normal distribution $N(114.17, 5)$ and the construction cost for the alternative A2 follows a normal distribution $N(128.00, 30)$. After randomly sampling from these probability distributions using Monte Carlo simulation, the final life cycle cost analysis results indicate that the Alternative A2, namely Eco-Bridge-Crete is less expensive (10.21 million dollars) compared with the Alternative A1, namely, conventional concrete (12.63 million dollars) in terms of their mean values. However, Alternative A2 has also more uncertainty due to a standard deviation of \$0.93 million compared to that of the conventional material which is \$0.19 million. One can determine, the likelihood of the Alternative A2's average life cycle cost being more than that of the Alternative A1 and decide which alternative to use based on these probabilities. Moreover, different probability functions can be used to study the sensitivity of LCC's uncertainty. Clearly, probabilistic LCCA provides us with an approach that is more versatile and comprehensive than the deterministic LCCA when it comes to making long-term decisions in the presence of a number of uncertainties that cannot be easily ignored. Please refer to project "Fiber-Reinforced Self-Consolidating Concrete (FR-SCC) for the repair of bridge sub-structures and Fiber-Reinforced Super-Workable Concrete (FR-SWC) for the infrastructure construction" for more detailed discussion of the technical aspects of the probabilistic approach for new materials or construction technologies.

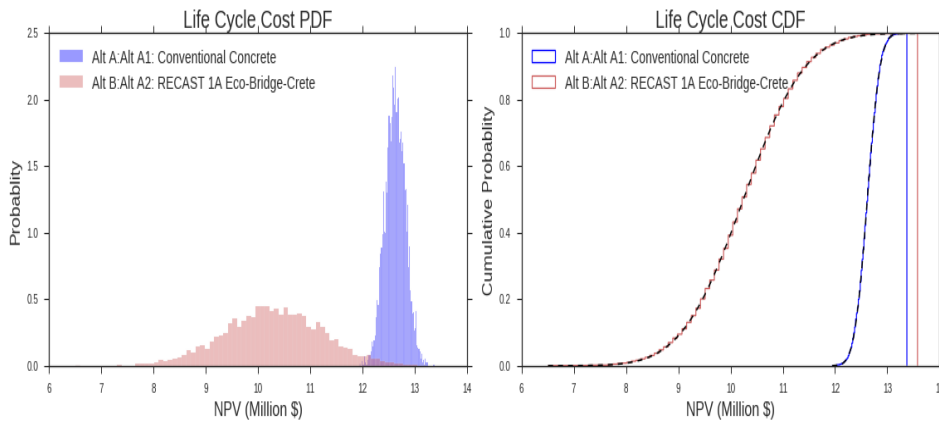


Figure 5.9. Bridge LCCA example – probabilistic approach

6. SUMMARY AND CONCLUSIONS

The research presented in this project was developed in several directions to design and formulate a new class of environmentally friendly, cost-effective, and crack-free high-performance concrete (HPC) for the use in pavement (Eco-Pave-Crete) and bridge infrastructure (Eco-Bridge-Crete) applications. The binder content of these novel materials were limited to 320 kg/m³ and 350 kg/m³, respectively, in order to reduce paste content, cost, CO₂ emissions, and shrinkage cracking. Both Eco-HPC types were optimized to develop high resistance to restrained shrinkage cracking as well as to secure high durability. A number of parameters contributing towards the formulation of such advanced concrete mixtures were investigated, including binder type and content, aggregate proportions, fiber type, and shrinkage mitigating materials. Based on the test results from this research, the following conclusions can be drawn:

6.1. Optimization of binder composition

The particle-size distribution (PSD) and specific surface area (SSA) of binders significantly affect the fresh and hardened characteristics of cement-based materials. An experimental investigation was undertaken to evaluate the influence of PSD and calculated SSA of various binary and ternary binder systems on flow characteristics, packing density, and compressive strength development of cement paste. The influence of dispersion state of the binder on packing density was evaluated using the wet packing density approach to determine the optimum water demand (OWD) needed to achieve maximum wet density. The modified Andreasen and Andersen (A&A), Rosin-Rammler (RR), and power law grading models were employed to optimize the PSD of binder system to achieve maximum packing density, while maintaining relatively low water demand.

- The packing density of colloidal particles is significantly related to the degree of dispersion of particles. In order to elicit the full benefit of the higher SSA for particle packing improvement, it is crucial to incorporate dispersing admixtures at the optimum dosage rate. The effectiveness of incorporating high volume of SCM to enhance packing density is shown to increase with the increase of HRWR dosage resulting from greater degree of dispersion of the binder. The incorporation of sufficient dosage of HRWR led to lower OWD needed to achieve maximum density and higher packing density. The coupled effect of these changes results in higher compressive strength. Compared to the packing density of 0.58 for binder with 100% cement, the use of SCMs in a well-dispersed system is shown to secure packing density of 0.60 to 0.73. The ternary binders containing 40% or 50% slag and 5% or 10% silica fume, by volume of total binder, can ensure lower water demand, greater packing density, lower CO₂ emission, and higher compressive strength. Such binder systems can be adopted for use in sustainable cement-based materials.
- The SSA of binder system was found to have considerable influence on flow characteristics and packing density of binders. Blended cements with higher SSA values developed greater RWD, thus reflecting higher robustness compared to the control mixture with 100% OPC. The modified A&A model can be used to optimize the PSD of

binder system to achieve maximum packing density, while maintaining relatively low water demand. Binder systems with the A&A distribution modulus (q) between 0.21 and 0.235 were shown to have 20% to 40% lower MWD to initiate flow, 8% to 35% lower OWD to reach maximum wet density, and 15% to 25% higher packing density compared to the binder with 100% OPC. Good correlations were established between the A&A distribution modulus, SSA, Rosin–Rammler (R–R) spread factor, and power law distribution exponent grading models.

- Regardless of the binder content, all mixtures made with binary and ternary blends of SCMs (targeted for Eco-Pave-Crete and Eco-bridge-Crete) resulted in lower drying shrinkage compared to that of the control mixture made with 100% OPC. As expected, the increase in the binder content resulted in higher drying shrinkage, regardless of the binder compositions. The control OPC mixtures with binder contents of 320 kg/m³ and 350 kg/m³ and w/c of 0.40 exhibited the highest drying shrinkage of 840 and 940 μ strain, respectively, after 150 days of drying among the investigated binder compositions.
- Hydration kinetics is found to correlate well with rheological properties and compressive strength development of OPC and PLC systems containing high volume of SCM replacements that are provisioned with PCE. Such correlations provide a reliable basis for a priori estimation of key engineering properties, both in the fresh and hardened state, and thus enable the optimization of binder formulation to provide more sustainable solution for concrete construction applications.

6.2. Optimization of aggregate skeleton

In total, 17 different aggregate samples with different shapes, textures, and PSDs from various aggregate quarries were evaluated to study the effect of aggregate characteristics on packing density of aggregate skeleton.

- The packing densities of aggregates are shown to vary with size, shape, surface texture, and angularity of aggregate. The packing densities of the investigated fine, intermediate, and coarse aggregates varied between 0.58-0.73, 0.6-0.73, and 0.57-0.61, respectively.
- The proportion of blended aggregate has substantial influence on the packing density of concrete. Based on the obtained results, the packing density of various aggregate proportions varied from 0.65 to 0.815 and 0.65 to 0.80 for rounded and crushed aggregates, respectively. The difference between the packing density of poorly-graded aggregate and well-graded aggregate was about 0.15, which significantly affects the required paste volume to fill the voids between solid particles. This can have considerable effect of material cost, CO₂ emission, and shrinkage.
- The selected aggregate blend for the investigated concrete mixtures had a packing density of 0.81. The PSD of such aggregate was close to the modified Andreasen and Andersen model with a q value of 0.275.
- Multiple criteria such as theoretical packing and grading models should be applied to select the optimum aggregate combination. A proposed statistical mixture design method was shown to be an effective in optimizing the proportioning of the blended aggregate to achieve the maximum possible packing density as well as to predict the packing density of the blended aggregates.

6.3. Comparison of shrinkage mitigating strategies

An experimental investigation was undertaken to evaluate the effect of initial moist curing period (IMCP), internal curing of lightweight sand (LWS), and shrinkage reducing admixture (SRA) on performance of calcium sulfoaluminate-based (CSA-based) and calcium oxide-based (CaO-based) and MgO-based EXs. The hydration reaction, autogenous and drying shrinkage, internal relative humidity (RH), thermogravimetry, and SEM were studied to examine the expansion potential of EXs. Statistical factorial design was conducted to assess the level of significance of the investigated materials and their interaction on autogenous and drying shrinkage as well as compressive strength of mixtures.

- The magnitude, rate, and duration of expansion provided by the EX was significantly influenced by the initial moist curing duration. Prolonged wet curing extends the duration of expansion caused by a given dosage of EX.
- The presence of moist curing is shown to be more crucial for mixture containing CSA-based EX system given relatively higher water consumption compared to the CaO-based EX system. In the absence of IMCP, similar drying shrinkage spread was found between control mixture made with 100% cement and mixture containing 15% CSA-based EX, by mass. The incorporation of SRA and LWS was shown to delay the drop in internal RH and facilitate the hydration reaction, thus promoting expansion potential of EX systems.
- The internal curing provided by LWS is substantially beneficial at elevating the compressive strength of mixture containing EXs when no IMCP is applied. The microstructural observation verified higher density and homogeneity of ITZ compared to similar mixture with only EX system.
- In the case of inadequate moist curing, the presence of LWS or SRA was found to be effective in enhancing the performance of OPC-CSA system.
- For a given moist curing duration and CSA-based EX content, the incorporation of 10% LWS or 1% SRA in OPC-CSA system was found to enhance the overall desirability function (in relation to shrinkage, material cost, and compressive strength) from 0.53 to 0.65 and 0.70, respectively. Therefore, the combined use of either LWS or SRA in OPC-CSA system can reduce the required period of moist curing and enhance the desirability value, thus indicating a greater overall performance.
- The synergistic effect between EX with LWS resulted in lower autogenous shrinkage or higher expansion magnitudes for a longer duration. This is attributed to the coupled effect of lower self-desiccation and larger expansion resulting from the use of LWS along with EX systems.

6.4. Development of Eco and crack-free HPC

Based on the obtained results from previous phases, the effect of different binder compositions, aggregate characteristics, and shrinkage mitigating materials were evaluated and the results were analyzed to design Eco- and crack-free HPC for different targeted applications (Eco-Pave-Crete and Eco-Bridge-Crete). The influence of composition and resultant reaction of blended binders proportioned with high volume of SCMs on shrinkage and restrained shrinkage cracking of Eco-concrete was investigated.

- Mixtures provisioned with SCMs exhibited up to 60% longer time-to-cracking and developed 2.4 to 4.4 times larger tensile creep coefficient at the time of crack initiation

compared to the control mixture without any SCM. Such spread can be attributed to: (i) resultant reaction and pozzolanic activity; and (ii) improved capillary porosity induced by SCMs, which can control the rate of elastic properties evolution and shrinkage at early- and later-age.

- The synergistic effect provided by the ternary combination of CFA and SL developed considerably higher tensile creep behavior and greater shrinkage cracking resistance compared to the binary blends of CFA or SL. Opposite trend was observed when SF incorporated in conjunction with CFA, reflecting lower tensile creep coefficient and increased shrinkage cracking potential compared to the binary blend of CFA.
- Hydration kinetics of binder systems can be correlated with shrinkage cracking resistance and tensile creep behavior of the Eco-concrete. Binders with greater early-age hydration reaction tend to exhibit lower tensile creep behavior and larger rate of shrinkage-induced tensile stress, thus increasing the risk of shrinkage cracking potential. Such composition-reaction property correlations can provide insights into proportioning sustainable binders with the aim of high resistance to shrinkage cracking.
- The synergetic effect of the combination of shrinkage reducing materials, including LWS and EX coupled with fibers (synthetic fibers or recycled steel fibers) is quite effective to design low cracking potential concrete. The internal curing provided by the LWS can reduce the shrinkage and risk of early-age shrinkage cracking, especially for mixtures subjected to air drying without using any initial moist curing.
- The incorporation of fibers (synthetic fibers and recycled steel fibers) in concrete containing a high volume of SCMs was shown to have 0 to 35% higher splitting tensile and flexural strengths than the control mixture made with 100% cement. The highest splitting tensile and flexural strengths were obtained for the mixture made with 35% recycled steel fibers containing 20% SL and 35% FA. This mixture also exhibited similar compressive strength to that of the control mixture.
- For a given fiber content, the use of steel fibers recovered from waste tires had two times higher flexural toughness compared to the similar mixture made with synthetic fibers. The reference mixture (100% OPC) made without any fibers developed the lowest ductility behavior and residual strength among all mixtures.
- The optimized Eco-HPC mixtures had lower drying shrinkage of 300 μ strain after 250 days of drying compared to 550 μ strain for the control mixture with 100% OPC. The incorporation of 7.5% CaO-based EX resulted in a significant early-age expansion of 100 μ strain followed by shrinkage of 200 μ strain after 250 days of drying.
- Eco-HPC mixtures made with proper combination of SCMs coupled with shrinkage mitigating materials can lead to crack-free properties with high resistance to shrinkage cracking. Based on the obtained results from this study, the use of 25% LWS or 7.5% CaO-based EX is quite effective in developing Eco-HPC with low risk of cracking.

6.5. Performance validation of Eco and crack-free HPC

Large-scale concrete slabs were constructed to evaluate the variations in relative humidity shrinkage of different optimized concrete mixtures and compare their performance with respect to the MoDOT reference mixture targeted for bridges. In addition, reinforced concrete beams were cast to evaluate the flexural strength of reinforced concrete made with optimized Eco-Bridge-Crete mixtures. Such concrete can be employed for the construction of bridge decks,

beams, piers, and other elements. The investigated mixture parameters include the incorporation of fibers, lightweight sand, expansive agent, and high volume of SCMs.

- The MoDOT control slab made with 25% FA replacement exhibited higher magnitude and rate of shrinkage compared to the optimized Eco-Bridge-Crete mixtures. This difference became more dominant for the top surface of concrete slab.
- The incorporation of 25% LWS was shown to be fully effective at reducing shrinkage rate and magnitude. The lowest relative humidity values observed for the FA25, SL20FA35-25LWS, and SL20FA35-7.5EX-0.35FRW mixtures were 82%, 96%, and 90%, respectively. This confirms that the combined use of SCM replacement and LWS can be fully beneficial at reducing shrinkage rate and magnitude.
- The shrinkage deformation values corresponding to such RH sensors were 80 μ strain shrinkage, 40 μ strain expansion, and 400 μ strain expansion for the FA25, SL20FA35-25LWS, and SL20FA35-7.5EX-0.35FRW mixtures, respectively, after 30 days of drying.
- All beams made with optimized concrete mixtures containing more than 50% SCM replacements exhibited equivalent or even higher ultimate flexural load than of the control beam made with MoDOT reference mixture containing 25% Class C FA.
- The inclusion of either structural synthetic fibers or recycled steel fibers was shown to substantially enhance the toughness of beam. The SL20FA35-7.5EX-0.35FT, SL60SF5-7.5EX-0.35FRW, and SL20FA35-7.5EX-0.35FRW concrete beams developed 120%, 135%, and 130% higher flexural toughness, respectively, compared to the control beam prepared with MoDOT reference mixture. The highest load carrying capacity was obtained for concrete beam made with 60% slag and 5% SF replacements having 0.35% recycled steel fibers.
- Furthermore, Life Cycle Cost Analysis was applied as an engineering-economic tool to evaluate both conventional concrete and Economical and Crack-free High Performance Concrete with Adapted Rheology. Hypothetical LCCA examples for a bridge deck and a pavement section were built based on the laboratory information provided by Missouri S&T. Compared with conventional concrete, the final deterministic LCCA results show that the application of the Eco-Bridge-Crete/Eco-Pave-Crete is less expensive in terms of total life cycle cost including weighted user cost and social cost. However, alternatives can be considered similar or equivalent if only agency costs were evaluated because the difference between alternatives is found to be less than 10% for the hypothetical scenarios considered in this report. Whereas, the benefit in user costs especially in the case of the bridge deck rehabilitation/replacement and potential energy consumption and GWP savings are found to play an important role and should not be ignored. When it comes to making long-term decisions in the presence of a number of uncertainties that the new material brings, probabilistic LCCA approach is found to be more versatile and comprehensive than the deterministic LCCA. The probabilistic LCCA results indicate that the Eco-Bridge-Crete is less expensive over its lifetime compared with the conventional concrete. However, the Eco-Bridge-Crete scenario is found to have a slightly higher uncertainty in comparison with the conventional concrete. It is thus important for the decision makers to weigh lower life time costs against higher uncertainty when making their selection of the material they will use in building a certain element of the transportation infrastructure.

REFERENCES

- Andreasen, A.H.M., Anderson, J. The Relation of Grading to Interstitial Voids in Loosely Granular Products (With Some Experiments). *Kolloid-Z.*, 49, 1929, 217-228.
- ASCE, 2017. 2017 infrastructure report card. Reston, VA: ASCE.
- Aslani, F. and Samali, B. High Strength Polypropylene Fibre Reinforcement Concrete at High Temperature, *Fire Technology* 50, 2014, 1229-47.
- Assaad, J., & Khayat, K. H. Assessment of Thixotropy of Self-Consolidating Concrete and Concrete-Equivalent-Mortar? Effect of Binder Composition and Content. *ACI Materials Journal*, 2004, 101(5), 400-408.
- Banthia, N. and Gupta, R. Influence of Polypropylene Fiber Geometry on Plastic Shrinkage Cracking in Concrete, *Cement and Concrete Research*, 36, 2006, 1263-67.
- Barrett, T.J., Sun, H., Weiss, W.J. Performance of Portland Limestone Cements: Cements Designed to be More Sustainable That Include up to 15% Limestone Addition. PhD dissertation, Purdue University, 2013.
- Bentz, D.P., Lura, P., Roberts, J.W. Mixture Proportioning for Internal Curing. *Concrete International*, 27(2), 2005, 35-40.
- Brooks, J.J., Megat, Johari, M.A., Mazloom, M. Effect of Admixtures on the Setting Times of High-Strength Concrete. *Cement and Concrete Composites*, 22, 2000, 293-301.
- Brouwers, H.J.H., Radix, H.J. Self-Compacting Concrete: Theoretical and Experimental Study, *Cement and Concrete Research*, 35, 2005, 2116-2136.
- Brown, M., Sellers, G., Folliard, K., Fowler, D., Restrained Shrinkage Cracking of Concrete Bridge Decks: State-of-the-art Review. Texas Department of Transportation, 2001.
- Brown, M.C., Ozyildirim, C. and Duke, W. Investigation of Fiber-Reinforced Self-Consolidating Concrete. Charlottesville, VA: Virginia Transportation Research Council, 2010.
- Caltrans. Life-Cycle Cost Analysis Procedures Manual. State of California Department of Transportation. 2013.
- CDOT, Colorado Department of Transportation. Pavement Design Manual, 2015.
- Chini, A.R., Muszynski, L.C., Hicks, J. Determination of Acceptance Permeability Characteristics for Performance-Related Specifications for Portland Cement Concrete, final report submitted to Florida Department of Transportation, 2003, 116-118.
- Courard, L., Darimont, A., Schouterden, M., Ferauche, F., Willem, X., Degeimbre, R. Durability of Mortars Modified with Metakaolin, *Cement and Concrete Research*, 33, 2003.
- Crowl, D., M. Sutak. A Survey of High Performance Concrete Bridge Decks. IV. Ohio Department of Transportation, District, 12, 2002.
- Cusson, D, Z Lounis, L Daigle. Benefits of Internal Curing on Service Life and Life-Cycle Cost of High-Performance Concrete Bridge Decks - A Case Study. *Cement and Concrete Composites*, 32(5), 2010, 339-350.

Dave, Eshan, V. Final Report - Synthesis of Performance Testing of Asphalt Concrete. Minnesota Department of Transportation. 2011.

De Larrard, F., Buil, M. Particle Size and Compactness in Civil Engineering Materials. *Materials and Structures*, 20, 1987: 117-126.

Eamon, C.D., Jensen, E.A., Grace, N.F., Shi, X. Life-Cycle Cost Analysis of Alternative Reinforcement Materials for Bridge Superstructures Considering Cost and Maintenance Uncertainties. *Journal of Materials in Civil Engineering*, 24(4), 2012, 373-380.

Ehlen, Mark, A. Life-Cycle Costs of New Construction Materials. *Journal of Infrastructure Systems*. 1997, 129-133.

FDOT, Florida Department of Transportation. 2013. Pavement Type Selection Manual.

FHWA. Life-Cycle Cost Analysis Technical Bulletin, 1998.

FHWA. Life-Cycle Cost Analysis Primer, 2002.

FHWA. FHWA's RealCost User Manual, 2004.

FHWA. Bridgew and Structures Unit Cost. accessed Feb. 25th. https://www.fhwa.dot.gov/bridge/nbi/unit_cost.cfm. 2011.

Folliard, K., C. Smith, G. Sellers, M. Brown, and J. E. Breen. Evaluation of Alternative Materials to Control Drying-Shrinkage Cracking in Concrete Bridge Decks. Texas DOT Report No. FHWA/TX-04/04098-4. 2003.

Gencel, O., Ozel, C., Brostow, W., Martinez-Barrera, G. *Materials Research Innovations* 15 (2011), 216-225.

Habert, G., Roussel, N. Study of Two Concrete Mix-Design Strategies to Reach Carbon Mitigation Objectives. *Cement and Concrete Composites*, 31, 2009, 397-402.

Herrmann, Andrew, W. ASCE. Report Card for America's Infrastructure. IABSE Symposium Report, 2013.

Holland, W.G. Illinois Department of Transportation's Life-Cycle Cost Analysis for Road Construction Contracts. State of Illinois, Office of the Auditor General, Springfield, IL, 2012.

Hooton, R.D., Nokken, M., and Thomas, M.D.A.T. Portland-Limestone Cement: State-of-the-Art Report and Gap Analysis for CSA A 3000, SN3053, Cement Association of Canada, Toronto, Ontario, Canada, 2007.

Horvath, Arpad. 2004. A Life-Cycle Analysis Model and Decision-Support Tool for Selecting Recycled Versus Virgin Materials for Highway Applications. University of California at Berkeley.

Hossain, A. Weiss, J. Assessing Residual Stress Development and Stress Relaxation in Restrained Concrete Ring Specimens, *Cement and Concrete Composites* 26, 2004, 531-40.

Hunger, M. An Integral Design Concept for Ecological Self-Compacting Concrete. PhD thesis, Eindhoven University of Technology, Eindhoven, the Netherlands, 2010.

Hüsken, G. Amultifunctional Design Approach for Sustainable Concrete with Application to Concrete Mass Products. PhD thesis Eindhoven University of Technology, Eindhoven, the Netherlands, 2010.

Hwang, S.D., Khayat, K.H. Effect of Mix Design on Restrained Shrinkage of Self-Consolidating Concrete. *Materials and structures*, 43(3), 2010, 367-380.

Hwang, S.D., Khayat, K.H. Effect of Mixture Composition on Restrained Shrinkage Cracking of Self-Consolidating Concrete Used In Repair. *ACI Materials journal*, 105(5), 2008, 499.

Imbabi, M.S., Carrigan, C., McKenna, S. Trends and Developments in Green Cement and Concrete Technology. *International Journal of Sustainable Built Environment*, 1(2), 2012, 194-216.

Jawad, Dima J. Life Cycle Cost Optimization for Infrastructure Facilities. Doctoral Thesis, Rutgers University, 2003.

Kassimi, F., Khayat, K.H. Effect of Fiber and Admixture Types on Restrained Shrinkage Cracking of Self Consolidating Concrete. Fifth North American Conference on the Design and Use of Self-Consolidating Concrete, Chicago, Illinois, USA, 2013.

Keoleian, G.A., Kendall, A., Dettling, J.E., Smith, V.M., Chandler, R.F., Lepech, M.D., Li V.C. Life-Cycle Cost Model for Evaluating The Sustainability of Bridge Decks. 2005.

Khayat, K.H., Libre, N.A. Roller Compacted Concrete: Field Evaluation and Mixture Optimization. No. NUTC R363, 2014.

Khayat, K.H., Mehdipour, I. Design and Performance of Crack-Free Environmentally Friendly Concrete "Crack-Free Eco-Crete. No. NUTC R322, 2014.

Khayat, K.H., Mehdipour, I., Optimization of Binder Compositions to Design Ecological Concrete; Wet Packing Density Approach. ECO-CRETE, International Symposium on Sustainability, Icelend, 2014.

Luhr, David, R. Economic Evaluation of Pavement Management Decisions. 9th International Conference on Managing Pavement Assets. 2015.

Lura, P., Pease, B., Mazzotta, G., Rajabipour, F., Weiss, J. Influence of Shrinkage Reducing Admixtures on the Development of Plastic Shrinkage Cracks. *ACI Materials Journal*. 104(2), 2007, 187-194.

Mehdipour, I., Khayat, K.H. Effect of Supplementary Cementitious Material Content and Binder Dispersion on Packing Density and Compressive Strength of Sustainable Cement Paste. *ACI Materials Journal*, 113(3), 2016, 361-372.

Mehdipour, I. and Khayat, K.H. Effect of Shrinkage Reducing Admixture on Early Expansion and Strength Evolution of Calcium Sulfoaluminate Blended Cement. *Cement and Concrete Composites*, 92, 2018, 82-91.

Mehdipour, I. and Khayat, K.H. Enhancing the performance of Calcium Sulfoaluminate Blended Cements with Shrinkage Reducing Admixture or Lightweight Sand. *Cement and Concrete Composites*, 87, 2018, 29-43.

Mehdipour, I. and Khayat, K.H., Understanding the Role of Particle Packing Characteristics in Rheo-Physical Properties of Cementitious Suspensions: A Literature Review. *Construction and Building Materials*, 161, 2018, 340-353.

Mehdipour, I. and Khayat, K.H. Elucidating the Role of Supplementary Cementitious Materials on Shrinkage and Restrained-Shrinkage Cracking of Flowable Eco-Concrete. *Journal of Materials in Civil Engineering*, 30(3), 2017, 04017308.

Mehdipour, I., Kumar, A. and Khayat, K.H. Rheology, Hydration, and Strength Evolution of Interground Limestone Cement Containing PCE Dispersant and High Volume Supplementary Cementitious Materials. *Materials & Design*, 127, 2017, 54-66.

Mehdipour, I. and Khayat, K.H. Effect of Particle-Size Distribution and Specific Surface Area of Different Binder Systems on Packing Density and Flow Characteristics of Cement Paste. *Cement and Concrete Composites*, 78, 2017, 120-131.

Mehdipour, I. Life Cycle Cost Survey and Personal Interview on RECAST Project 1-A. 2016.

Mehta, P.K., Greening of the Concrete Industry for Sustainable Development. *Concrete international*, 23, 2002.

Mehta, P.K., Monteiro, P.J.M., *Concrete: Microstructure, Properties, and Materials*. 3rd Ed. McGraw Hill, New York, 2006.

Missouri Department of Transportation. 2004. Pavement Design and Type Selection Process Phase I Report.

Mueller, F.V., Wallevik, O.H., Khayat, K.H., Linking Solid Particle Packing of Eco-SCC to Material Performance. *Cement and Concrete Composites*, 54, 2014, 117-125.

Na, C., Nassif, H., Jonhsen, W.S. Strength at Early Age and Shrinkage Behavior of High Performance Concrete (TRB13-4986). Paper presented at the Transportation Research Board Annual Meeting, Washington D.C., January, 2013

Nassif, H., Aktas, K., Najm, H. Self-Consolidating Concrete (Phase I & II). Trenton, NJ: New Jersey Department of Transportation FHWA-NJ-2007-021, 2008.

Nassif, H., Aktas, K., Najm, H. Concrete Shrinkage Analysis for Bridge Deck Concrete. Trenton, NJ: New Jersey Department of Transportation FHWA-NJ-2007-007, 2007.

Nassif, H., Aktas, K., Najm, H. Concrete Shrinkage Analysis for Bridge Deck Concrete. No. FHWA NJ-2007-007. New Jersey Department of Transportation, Trenton, NJ, 2007.

NJDOT. Internal Inspection Report, 2015.

ODOT, The Ohio Department of Transportation. 2014. Pavement Design Manual.

Okamura, H., Maekawa K., Ozawa, K. *High-Performance Concrete*. Tokyo, Japan: Gihido Publishing, 1993.

Ozbay, Kaan, Neville, A. Parker, Dima Jawad, and Sajjad Hussain. 2002. Guidelines for Life Cycle Cost Analysis Final Report. New Jersey.

Richardson, D.N. Aggregate Gradation Optimization – Literature Search, Report No. RDT 05-001, Missouri Department of Transportation, Jefferson City, MO, 2005.

Richardson, D.N. Aggregate Gradation Optimization – Literature Search, Report No. RDT 05-001, Missouri Department of Transportation, Jefferson City, MO, 2005.

- Romualdi, J., Mandel, J. Tensile Strength of Concrete Affected by Uniformly Distributed and Closely Spaced Short Lengths of Wire Reinforcement, *Journal of the American Concrete Institute* 61, 1964, 657-71.
- Saje, D., Bandeji, B., Sustersic, J., Lopatic, J., Saje, F. Shrinkage of Polypropylene Fiber-Reinforced High-Performance Concrete, *Journal of Materials in Civil Engineering* 23, 2011, 941-952
- Santero, N., Loijos, A. and Ochsendorf, J., Greenhouse Gas Emissions Reduction Opportunities for Concrete Pavements. *Journal of Industrial Ecology* 17(6), 2013, 859-868.
- Shah, S.P., Karaguler, M.E., Sarigaphuti, M., Effects of Shrinkage Reducing Admixtures on Restrained Shrinkage Cracking of Concrete. *ACI Materials Journal*, 89(3), 1992, 291-295.
- Soliman, M., Frangopol, D.M. Life-Cycle Cost Evaluation of Conventional and Corrosion-Resistant Steel for Bridges. *Journal of Bridge Engineering* 20(1), 2014, 06014005.
- Turner, L.K., Collins, F.G. Carbon Dioxide Equivalent (CO₂-E) Emissions: A Comparison Between Geopolymer and OPC Cement Concrete. *Construction and Building Materials*. 43, 2013, 125-130.
- USDOT. Moving Ahead for Progress in the 21st Century Act ("MAP-21"). US Department of Transportation, Federal Motor Carrier Safety Administration, 2012.
- VDOT, Virginia Department of Transportation. Life Cycle Cost Analysis, 2011.
- Wang, X. Proportioning and Performance Evaluation of Self-Consolidating Concrete (Doctoral dissertation, Iowa State University). 2014.
- Weiss, W.J., Berke, N.S. Admixtures for Reduction of Shrinkage and Cracking. Early Age Cracking In Cementitious Systems, Chapter 7.5, RILEM Report 25, A. Bentur, ed., Bagnaux, France, 2003, 323-338.
- Weiss, W.J., Shah, S.P. Restrained Shrinkage Cracking: The Role of Shrinkage Reducing Admixtures and Specimen Geometry. *Materials and Structures*, 35(246), 2012, 85-91.
- Yu, R., Spiesz, P., Brouwers, H.J.H. Development of an Eco-Friendly Ultra-High Performance Concrete (UHPC) with Efficient Cement and Mineral Admixtures Uses, *Cement and Concrete Composites*, 55, (2015), 383-394.

APPENDIX A MATERIAL PROPERTIES

Table A.1. Physical and chemical characteristics of cementitious materials and expansive agents

	OPC	Class C FA	SL	SF	Type K EX	Type G EX
SiO ₂ (%)	19.8	36.5	36.8	85	7.7	12.6
Al ₂ O ₃ (%)	4.5	24.8	9.2	0.4	7	5.7
Fe ₂ O ₃ (%)	3.2	5.2	0.8	0.5	1.2	1.9
CaO (%)	64.2	28.1	37.1	–	50.1	82.6
MgO (%)	2.7	5	9.5	–	0.1	0.1
SO ₃ (%)	3.4	2.5	0.1	–	26	
Na ₂ O eq. (%)	–	–	0.3	–	0.6	0.9
CaCO ₃ (%)	3.3	–	–	–	–	–
Blaine surface area (m ² /kg)	390	498	570	16500	–	–
Density (g/cm ³)	3.14	2.71	2.86	2.3	2.9	3.1
LOI (%)	1.5	0.5	–	2	2.1	–

Table A.2. Mixture proportions of the investigated CEM mixtures (volume-basis)

Type	Mixture no.	Codification	OPC	SL	CFA	SF
Eco-Pave-Crete	1-1	1-OPC	100	0	0	0
	1-2	1-FA55	45	0	55	0
	1-3	1-SL60	40	60	0	0
	1-4	1- SL20FA35	45	20	35	0
	1-5	1- SL20FA50	30	20	50	0
Eco-Bridge-Crete	2-1	2-OPC	100	0	0	0
	2-2	2-FA40	60	0	40	0
	2-3	2-SL60	40	60	0	0
	2-4	2-FA40SF5	55	0	40	5
	2-5	2-SL60SF5	35	60	0	5
	2-6	2- SL20FA35	45	20	35	0

Note: CFA: Class C fly ash, SL: slag, and SF: silica fume

Table A.3. Random proportions of aggregate blends used for SMD

Run	Fine aggregate (%)	Intermediate aggregate (%)	Coarse aggregate (%)
1	45	30	25
2	30	0	70
3	55	0	45
4	20	30	50
5	70	10	20
6	35	30	35
7	40	20	40
8	55	15	30
9	25	45	30
10	30	15	55
11	40	5	55
12	20	60	20
13	100	0	0
14	0	100	0
15	0	0	100

Table A.4. Testing parameters to evaluate various shrinkage mitigating materials

Series	Description	Binder type				Lightweight sand (LWS) 25% replacement	Expansive agent (EX)		No. of mixtures
		Ref	Pavement	Bridge deck			7.5% CaO-based system	5% MgO-based system	
		100% OPC	Selected binder 1	Selected binder 1	Selected binder 2				
1	Effect of binder type	x	x	x	x			4	
2	CaO-based EX	x	x	x	x		x	4	
3	MgO-based EX	x	x	x	x		x	4	
5	Effect of LWS 1 combined with EX	x	x	x	x	x	x	4	
6	Effect of LWS 2 combined with EX	x			x	x	x	2	
7	Crack-reducing admixture	x			x			2	

Table A.5. Experimental program used for phase 3

Property	Test
Flow characteristics	Admixture demand for a given fluidity
Kinetics of cement hydration	Calorimetry
Setting time	Penetration resistance for autogenous shrinkage measurement
Mechanical properties	Compressive strength at 7, 28, and 56 days for different curing regime
Durability	Surface resistivity (AASHTO T95) at 28, 56, and 91 days Bulk electrical conductivity (ASTM C1760) at 28, 56, and 91 days
Shrinkage properties	Autogenous shrinkage (ASTM C1698) Drying shrinkage (ASTM C157)

Table A.6. Proposed initial moist curing period

Moist curing duration	Detail
Air curing	1 day in mold, then air drying at 23 °C and 50% RH
Moist curing of 3 d	1 day in mold, then 2 days moist curing, then air drying at 23 °C and 50% RH
Moist curing of 7 d	1 day in mold, then 6 days moist curing, then air drying at 23 °C and 50% RH
Continuous moist curing	1 day in mold, then continuous moist curing until the age of testing

Table A.7. Mixture design parameters for design of Eco-HPC

Mix	Description	Binder content		Binder type			Fiber type and content			Shrinkage reducing/compensating materials	
		320 (kg/m ³)	350 (kg/m ³)	100% OPC	Selected binder 1	Selected binder 2	Selected binder 3	TUF strand fiber (0.35%)	STRUX® 90/40 synthetic fiber (0.35%)	Steel fiber from tire (0.35%)	25% LWS
R	Reference		x	x							
B1	Effect of binder type	x				x					
B2			x			x					
B3		x			x						
B4			x				x				
B1	Effect of LWS		x			x				x	
B2		x			x					x	
B3			x				x			x	
F1	Effect of fiber type		x			x		x			
F2			x			x			x		
F3			x				x			x	
E1	Effect of EX		x			x					x
EF1	Combined effect of fiber and EX		x			x		x			x
EF3			x			x			x		x

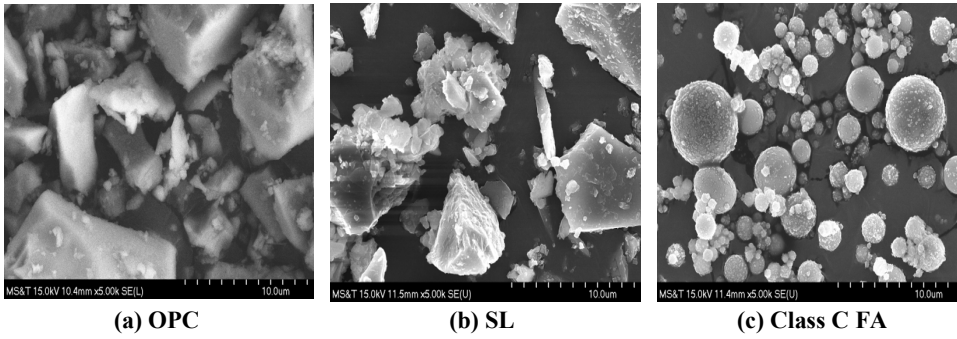


Figure A.1. SEM images of cementitious materials with magnification of 5000

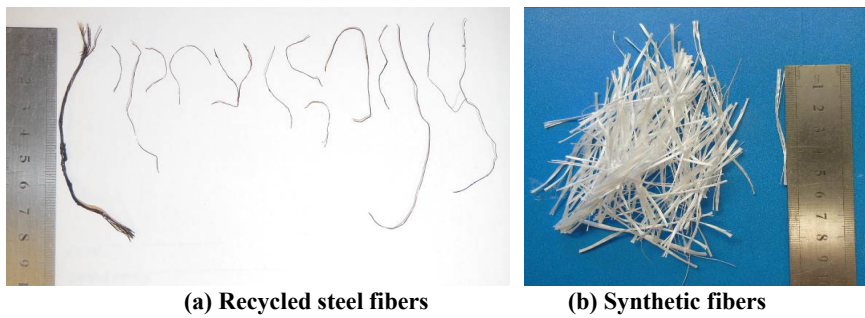


Figure A.2. Fiber types used in this study



Figure A.3. Location of aggregate quarries visited in this investigation

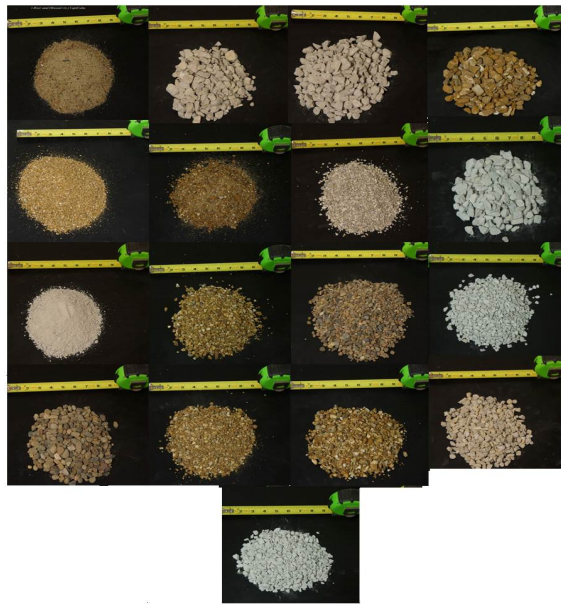
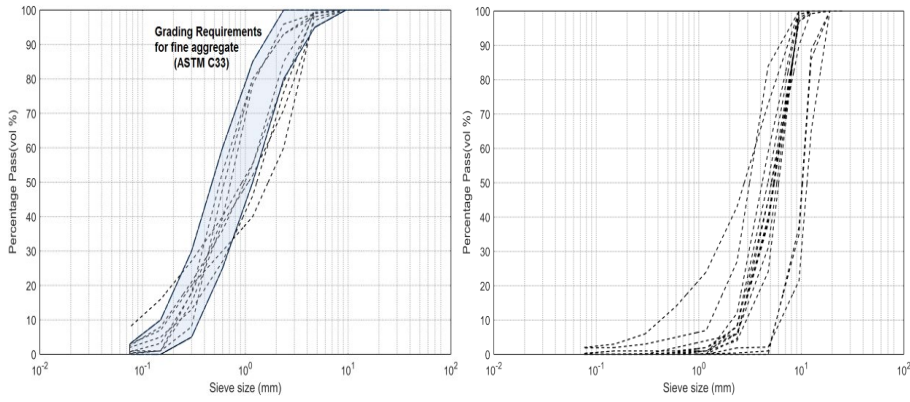
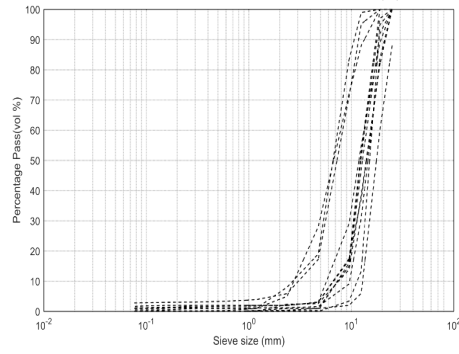


Figure A.4. Photo of sampled aggregates



(a) Fine aggregate

(b) Intermediate aggregate



(c) Coarse aggregate

**Figure A.5. PSDs of examined aggregates
(Hatched area refers to grading limits in accordance with ASTM C33)**

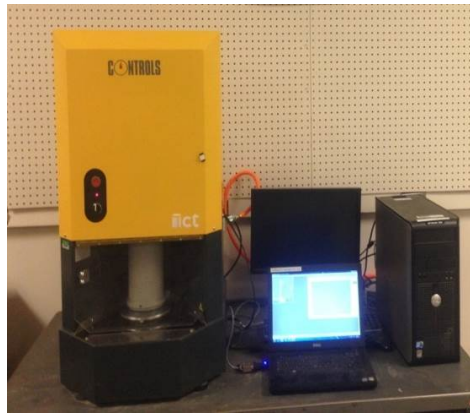


Figure A.6. Gyratory intensive compaction tester



Figure A.7. Dolese Bros. Co. Davis quarry



Figure A.8. Micro (l) and macro (r) synthetic fibers

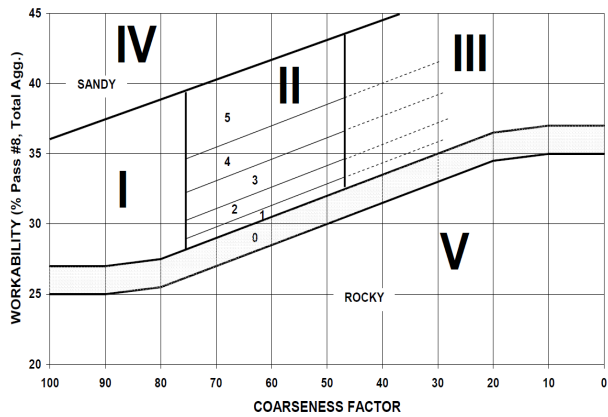


Figure A.9. Revised Shilstone coarseness factor chart (Richardson, 2005)

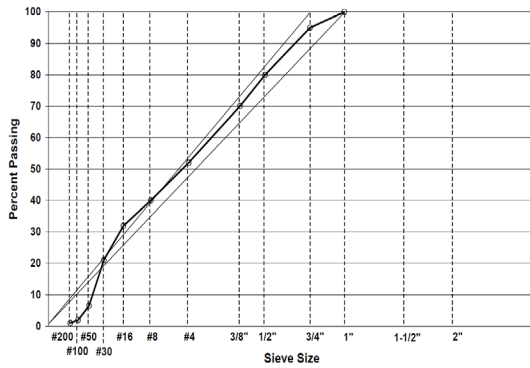


Figure A.10. 0.45 power chart (Richardson, 2005)

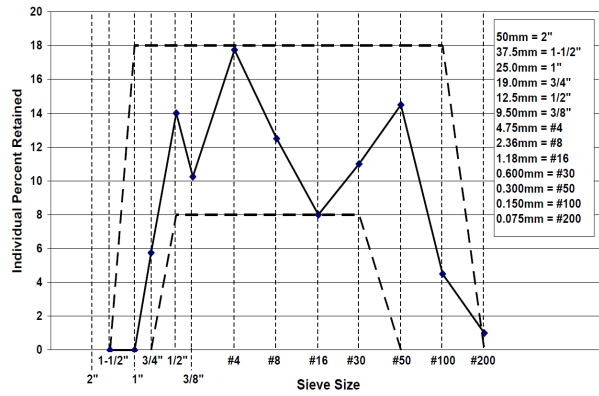


Figure A.11. Individual percent retained chart (Richardson, 2005)



Figure A.12. Isothermal calorimetry used for hydration kinetics of mortar



Figure A.13. Coaxial cylinders rheometer used to determine rheological properties of mortar



Figure A.14. Autogenous shrinkage measurement device

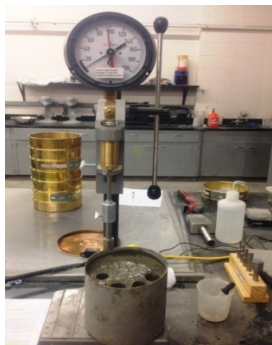


Figure A.15. Setting time test setup



Figure A.16. Drying shrinkage measurement of mortar



Figure A.17. Test setup for flexural toughness measurement of FRC beams



Figure A.18. Abrasion resistance test setup



Figure A.19. Freeze-thaw chamber (left) and ultrasonic velocity instrument (right)

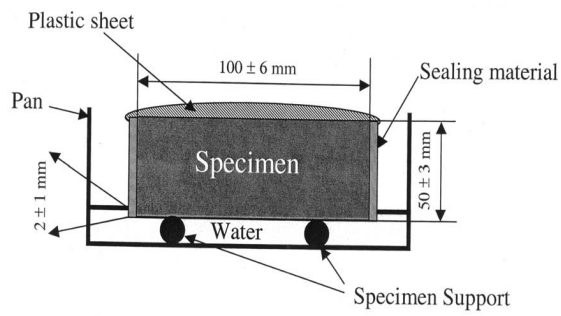


Figure A.20. Schematic illustration of sorptivity test



Figure A.21. Shrinkage measurement of unsealed (left) and sealed specimens (right)



Figure A.22. Restrained shrinkage ring test setup



(a) Slump flow test

(b) J-Ring test

Figure A.23. Slump flow and J-Ring test

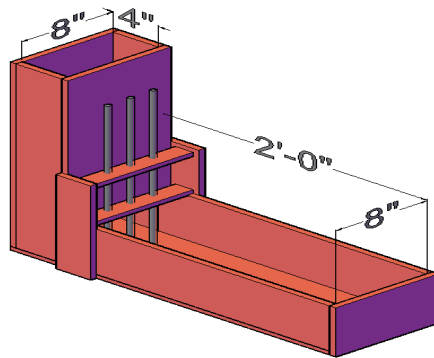


Figure A.24. L-Box setup

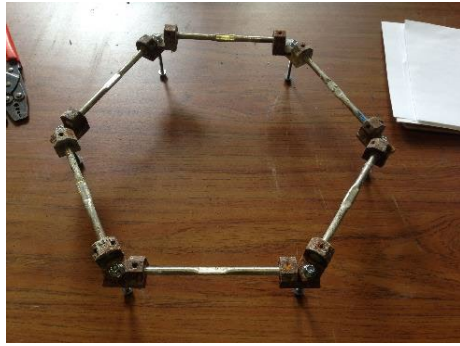


Figure A.25. Vibrating Wire Strain Gauge (VWSG), hexagon enclosed setup

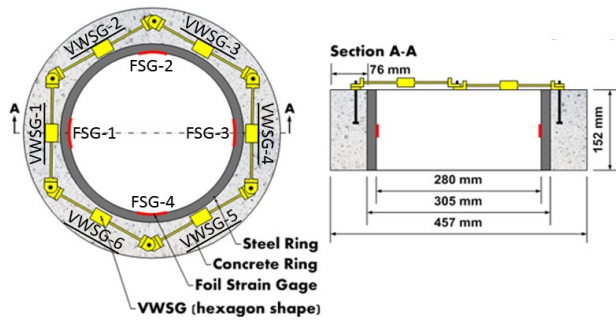


Figure A.26. Modified AASHTO ring with VWSGs and FSGs

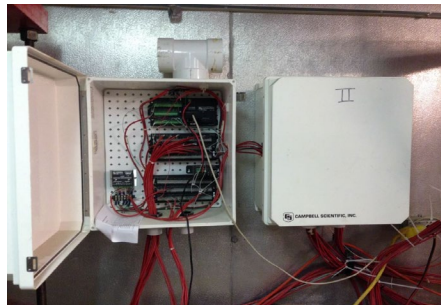


Figure A.27. Data acquisition system

APPENDIX B TEST RESULTS AND DISSCUSSION

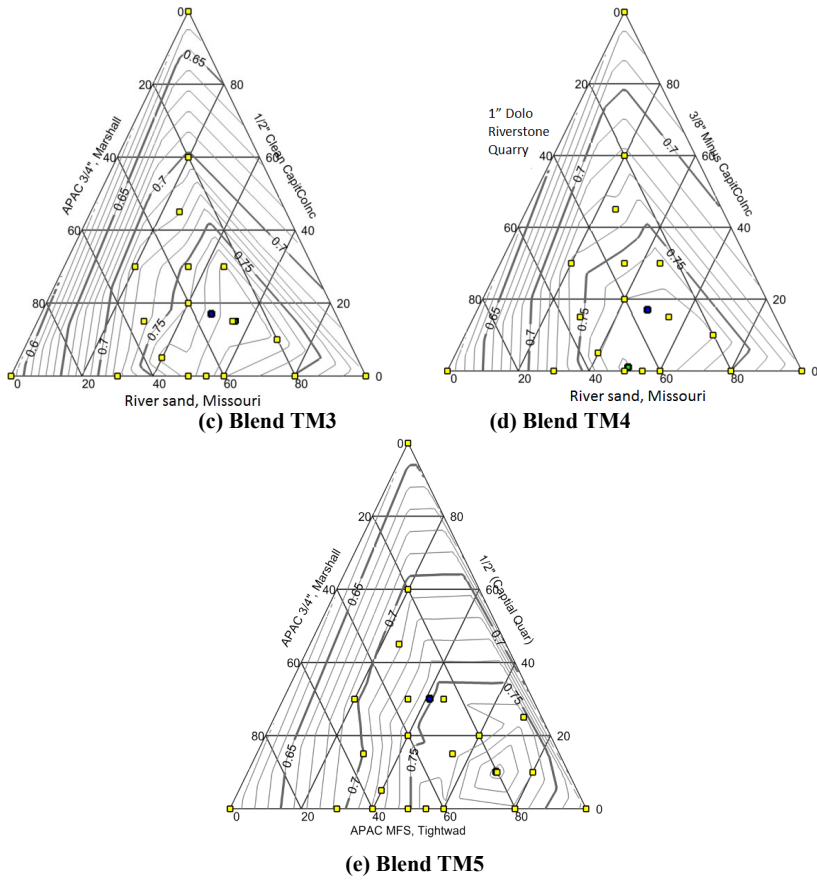


Figure B.1. Ternary Packing diagram of various aggregate blends measured by ICT

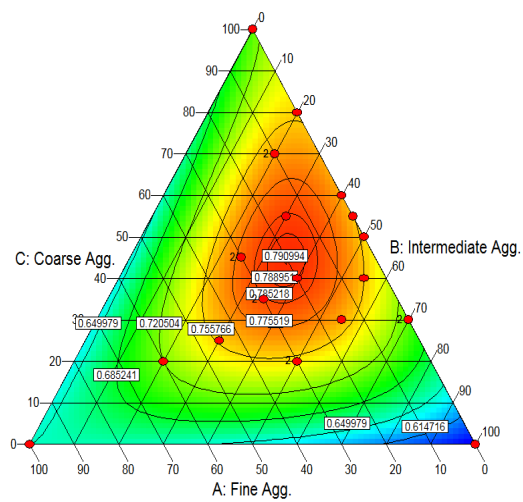


Figure B.2. Contour diagram of packing density for ternary aggregate blend

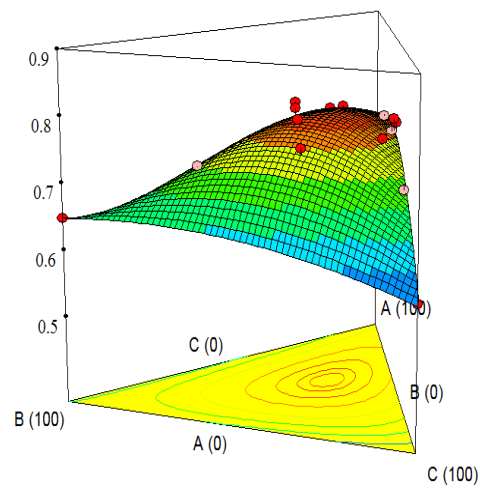


Figure B.3. Surface response of packing density for ternary aggregate blend

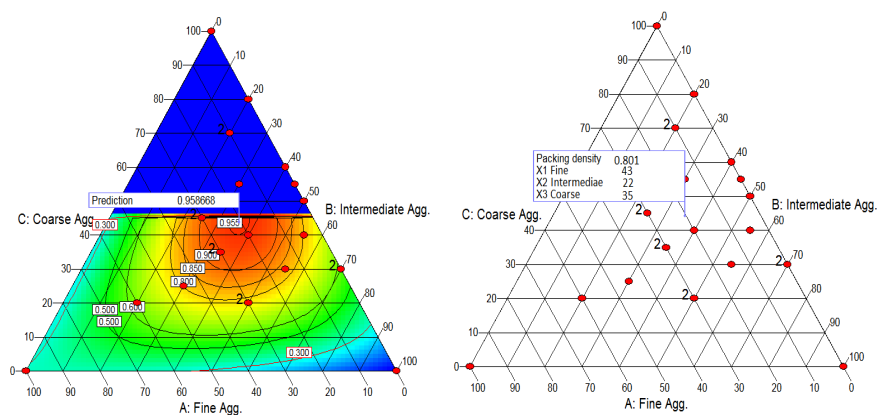


Figure B.4. Contour diagram of desirability to achieve maximum packing density

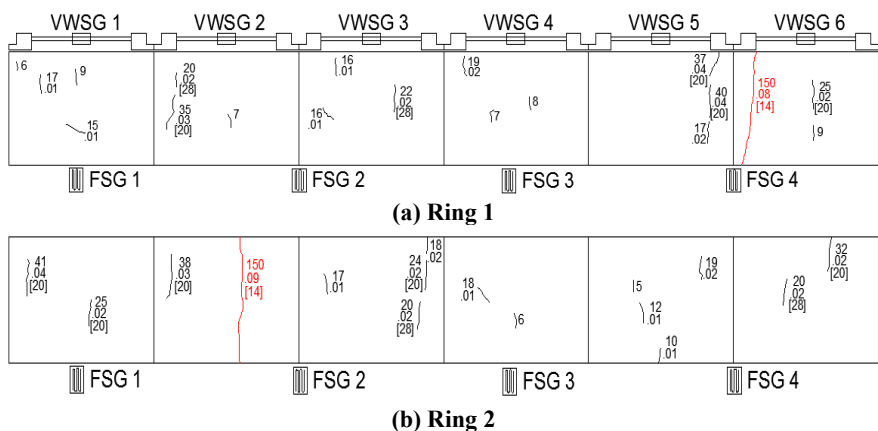


Figure B.5. Crack map of PPE 0.00 mixture



Figure B.6. Visible crack in PPE 0.00 mixture ring 2 from the side and above

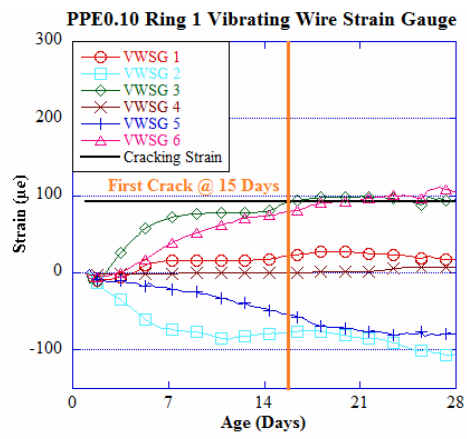


Figure B.7. Concrete strain (VWSG) of PPE 0.10 mixture ring

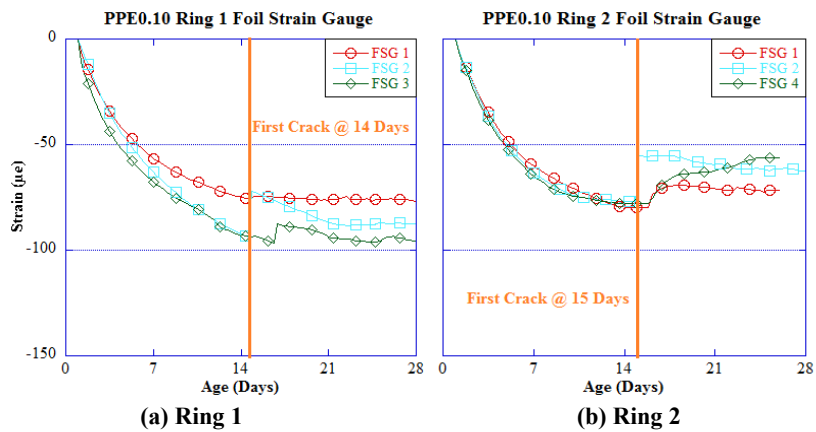


Figure B.8. Steel strain (FSG) of PPE 0.10 mixture

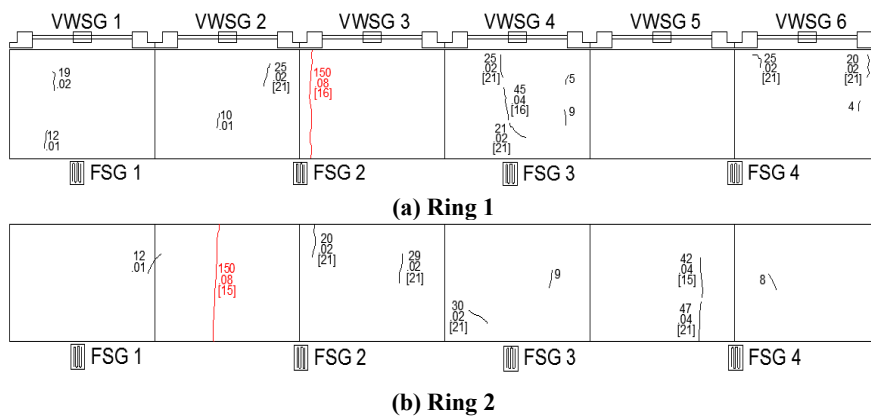


Figure B.9. Crack map of PPE 0.10 mixture

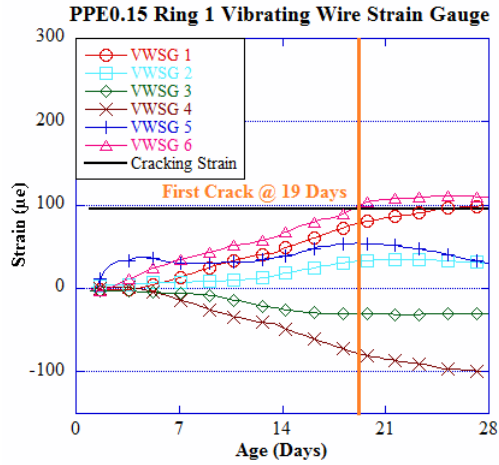
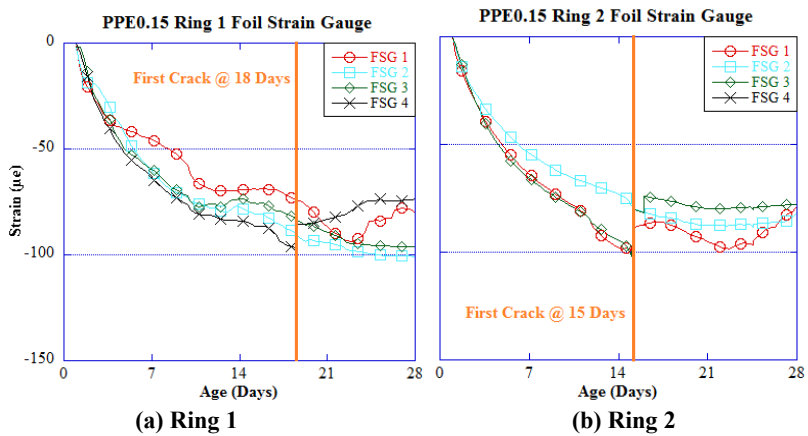


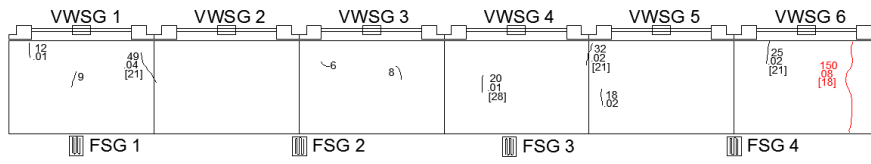
Figure B.10. Concrete strain (VWSG) of PPE 0.15 mixture ring 1



(a) Ring 1

(b) Ring 2

Figure B.11. Steel strain (FSG) of PPE 0.15 mixture



(a) Ring 1



(b) Ring 2

Figure B.12. Crack map of PPE 0.15 mixture

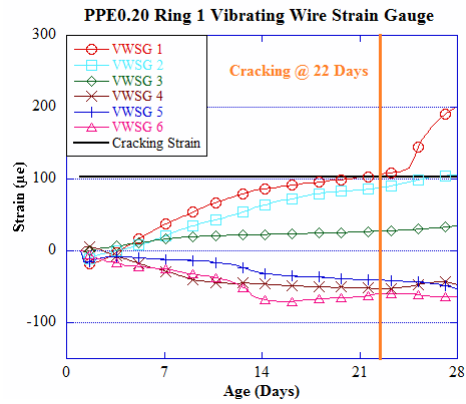


Figure B.13. Concrete strain (VWSG) of PPE 0.20 mixture ring 1

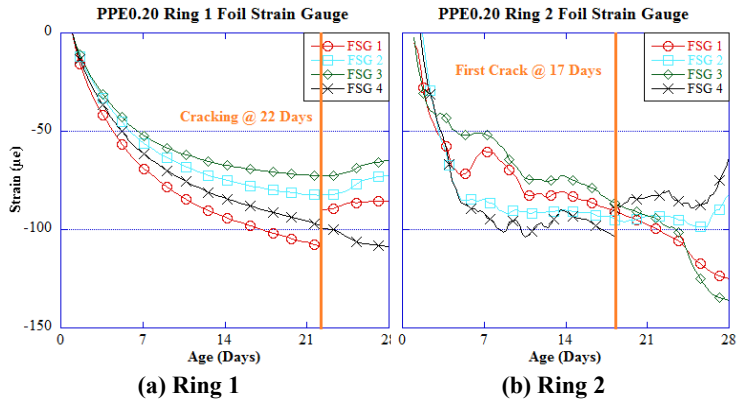


Figure B.14. Steel strain (FSG) of PPE 0.20 mixture

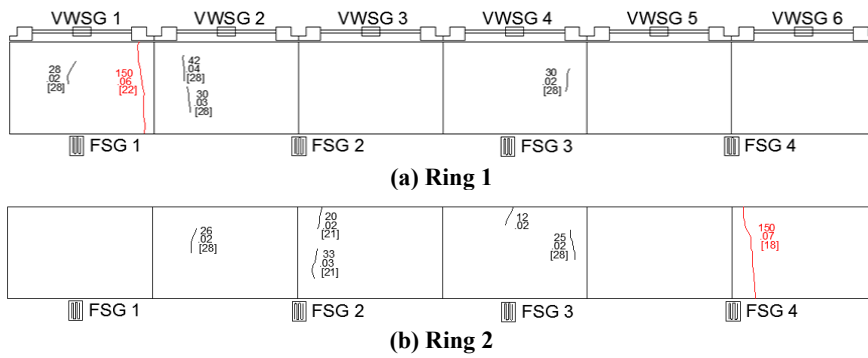


Figure B.15. Crack map of PPE 0.20 mixture

APPENDIX C VALIDATION OF ECO-HPC PERFORMANCE IN LARGE-SCALE ELEMENTS

Table C.1. Selected concrete mixtures for reinforced concrete beams

Concrete type	w/cm	Binder content		Binder type			Fiber type and content		Shrinkage reducing/compensating materials	
	0.40	350 kg/m ³	375 kg/m ³	75% OPC + 25% Class C FA	45% OPC + 20% SL + 35% Class C FA	35% OPC + 60% SL + 5% SF	TUF strand fibers (0.35%)	Steel fibers from tire (0.35%)	25% LWS	7.5% Type G EX
MoDOT reference mixture	x		x	x						
Eco-Bridge-Crete	x	x			x				x	
	x	x			x					
	x	x			x		x			x
	x	x			x			x		x
	x	x				x			x	
	x	x				x		x		x

Table C.2. Compressive strength results of concrete mixtures used for beams

Mixture no.	Codification	Testing age (day)	Compressive strength (MPa)
B1	SL20FA35	55	47
B2	SL20FA35-7.5EX-0.35FT	50	53
B3	SL60SF5-25LWS	45	55
B4	SL60SF5-7.5EX-0.35FRW	45	50
B5	FA25 (MoDOT reference mixture)	40	50
B6	SL20FA35-25LWS	40	47
B7	SL20FA35-7.5EX-0.35FRW	40	45

Table C.3. Beam shear specimen test results

Mixture	Specimen	Peak Load (kips)		Deflection at Failure (in.)	
		Test Value	Average	Test Value	Average
Class AA	K-C-1	65.0	60.1	0.35	0.30
	K-C-2	59.0		0.32	
	K-C-3	56.4		0.29	
Eco-Bridge-Crete Mixture No. 1	K-E1-1	69.8	62.1	0.40	0.36
	K-E1-2	65.2		0.35	
	K-E1-3	51.3		0.34	
Eco-Bridge-Crete Mixture No. 2	K-E2-1	60.1	66.4	0.34	0.40
	K-E2-2	71.0		0.50	
	K-E2-3	68.1		0.37	

Table C.4. Beam shear test results vs. code capacities

Mixture	Specimen	Test vs. code capacity	
		V_{Test}/V_{Code}	Avg. V_{Test}/V_{Code}
Class AA	K-C-1	1.30	1.20
	K-C-2	1.18	
	K-C-3	1.13	
Eco-Bridge-Crete Mixture No. 1	K-E1-1	1.44	1.28
	K-E1-2	1.35	
	K-E1-3	1.06	
Eco-Bridge-Crete Mixture No. 2	K-E2-1	1.19	1.32
	K-E2-2	1.41	
	K-E2-3	1.35	

Table C.5. Beam splice specimen test results

Mixture	Specimen	Peak load (kips)		Peak steel stress (ksi)	
		Test value	Average	Test value	Average
Class AA	D-C-1	52.6	53.0	69.6	66.4
	D-C-2	52.2		65.8	
	D-C-3	54.2		63.8	
Eco-Bridge-Crete Mixture No. 1	D-E1-1	45.1	45.4	62.5	67.9
	D-E1-2	47.5		73.4	
	D-E1-3	43.7		67.7	
Eco-Bridge-Crete Mixture No. 2	D-E2-1	49.5	46.6	56.8	52.0
	D-E2-2	40.9		43.5	
	D-E2-3	49.5		55.7	

Table C.6. Normalized beam splice test results

Mixture	Specimen	Normalized bond stress (ksi)			
		Square root	Average	Fourth root	Average
Class AA	D-C-1	74.5	71.1	72.0	68.7
	D-C-2	70.4		68.1	
	D-C-3	68.3		66.0	
Eco-Bridge-Crete Mixture No. 1	D-E1-1	71.3	77.4	66.7	72.4
	D-E1-2	83.7		78.4	
	D-E1-3	77.1		72.2	
Eco-Bridge-Crete Mixture No. 2	D-E2-1	59.3	54.3	58.0	53.1
	D-E2-2	45.5		44.5	
	D-E2-3	58.2		56.9	



Figure C.1. Slab section used for shrinkage deformation evaluation



Figure C.2. Embedded strain gauge for monitoring shrinkage deformation

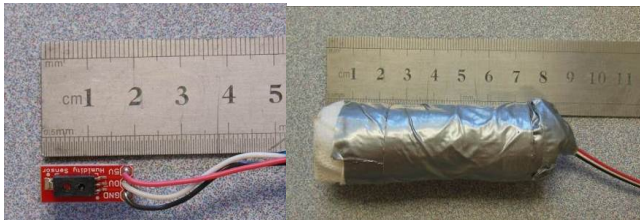
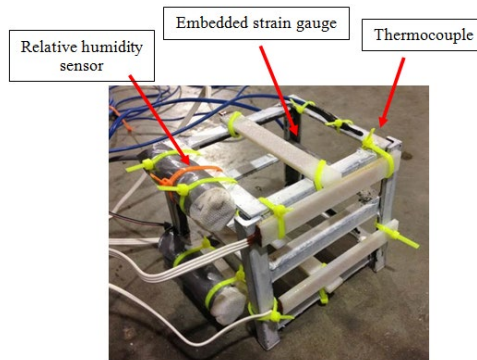


Figure C.3. Encapsulated relative humidity sensor before embedment in concrete



(a) Layout A: 3 embedded strain gauges in longitudinal direction, 3 thermocouples and 3 relative humidity sensors



(b) Layout B: 4 embedded strain gauges (two longitudinal and two transverse directions), 2 thermocouples and 2 relative humidity sensors

Figure C.4. Instrumentation layouts

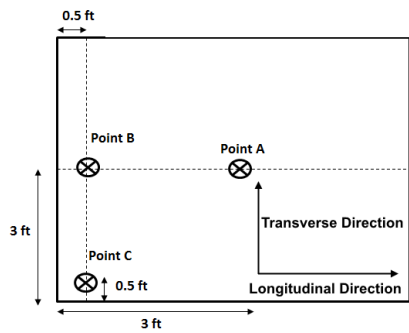


Figure C.5. Instrumentation location plan for each slab

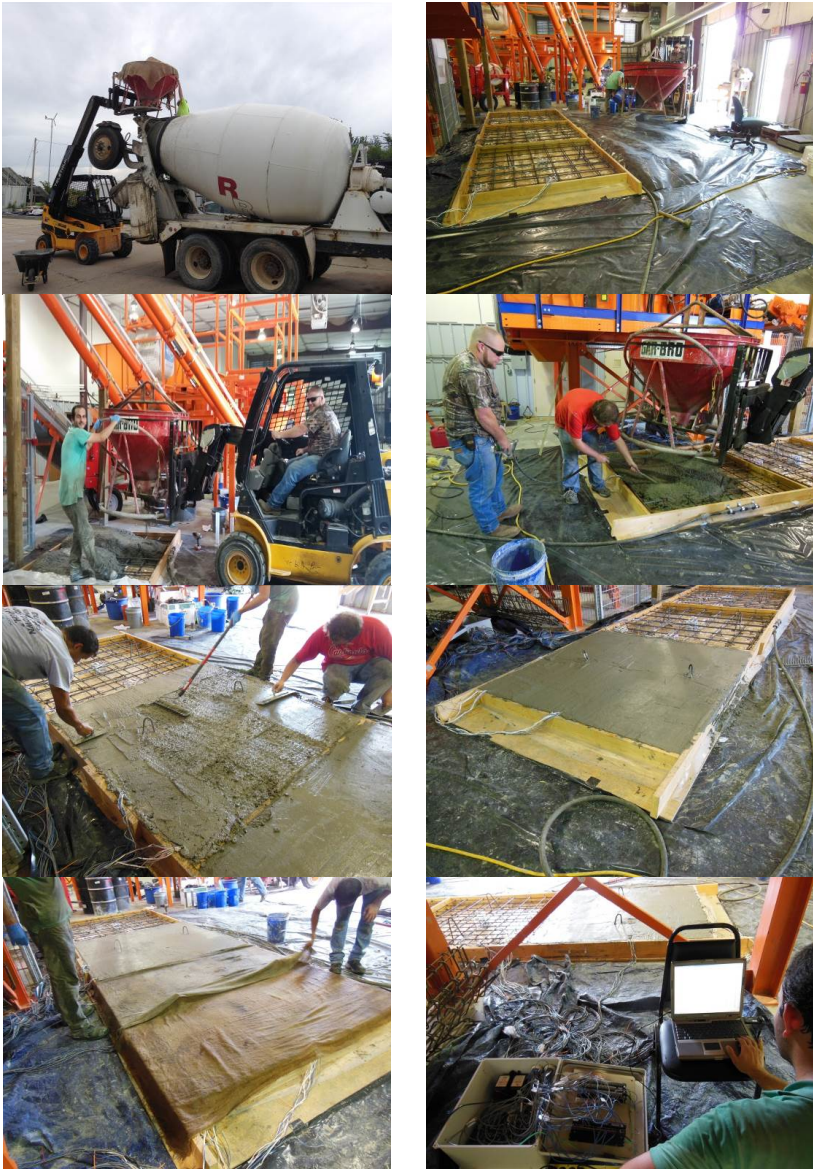


Figure C.6. Concrete slab construction procedures

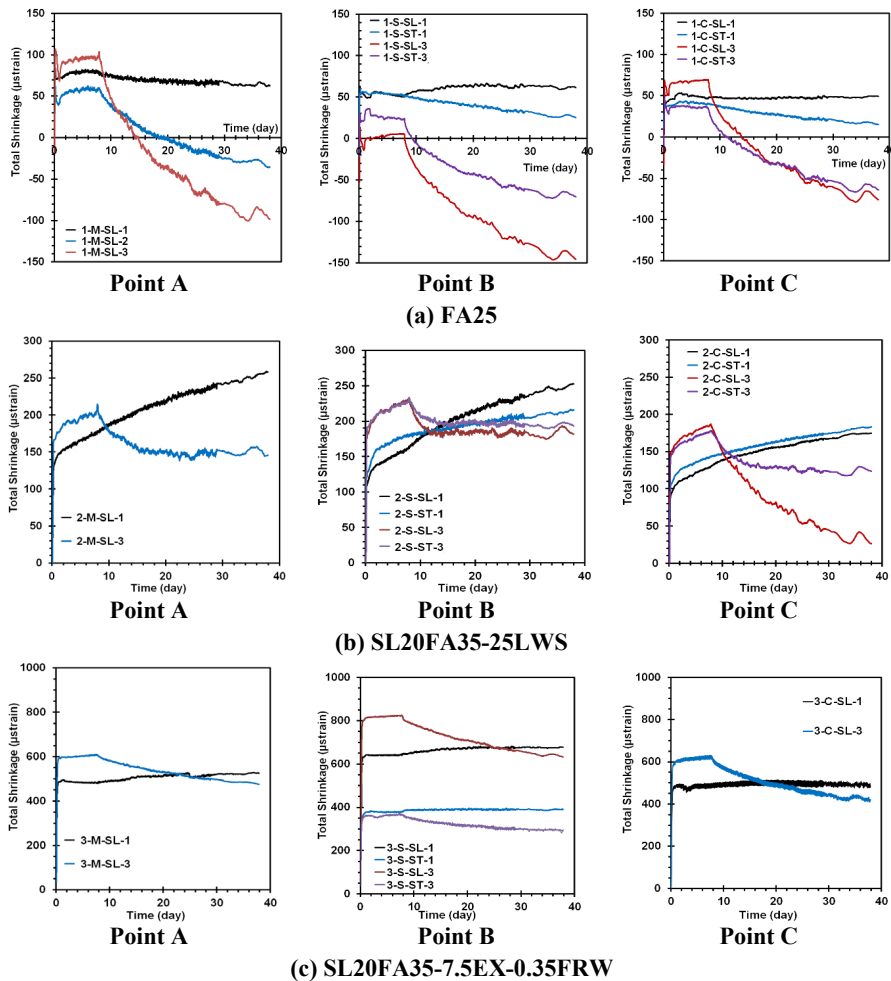


Figure C.7. Shrinkage deformation over height of slabs at different stations. All slabs were moist cured for seven days before exposure to air drying

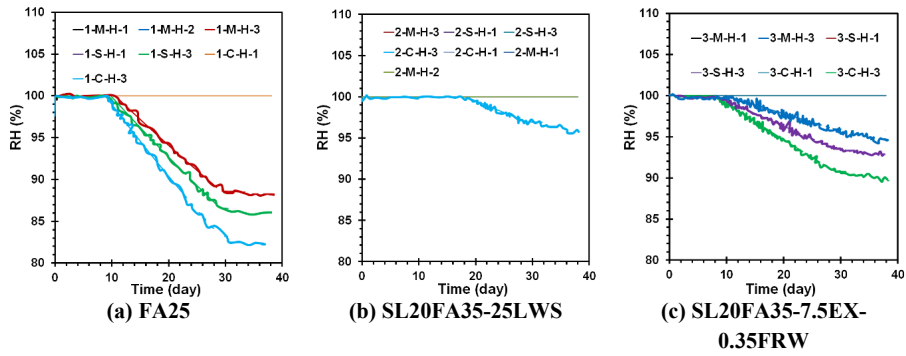


Figure C.8. Relative humidity variations along height of slabs at different stations. All slabs were moist cured for seven days before exposure to air drying

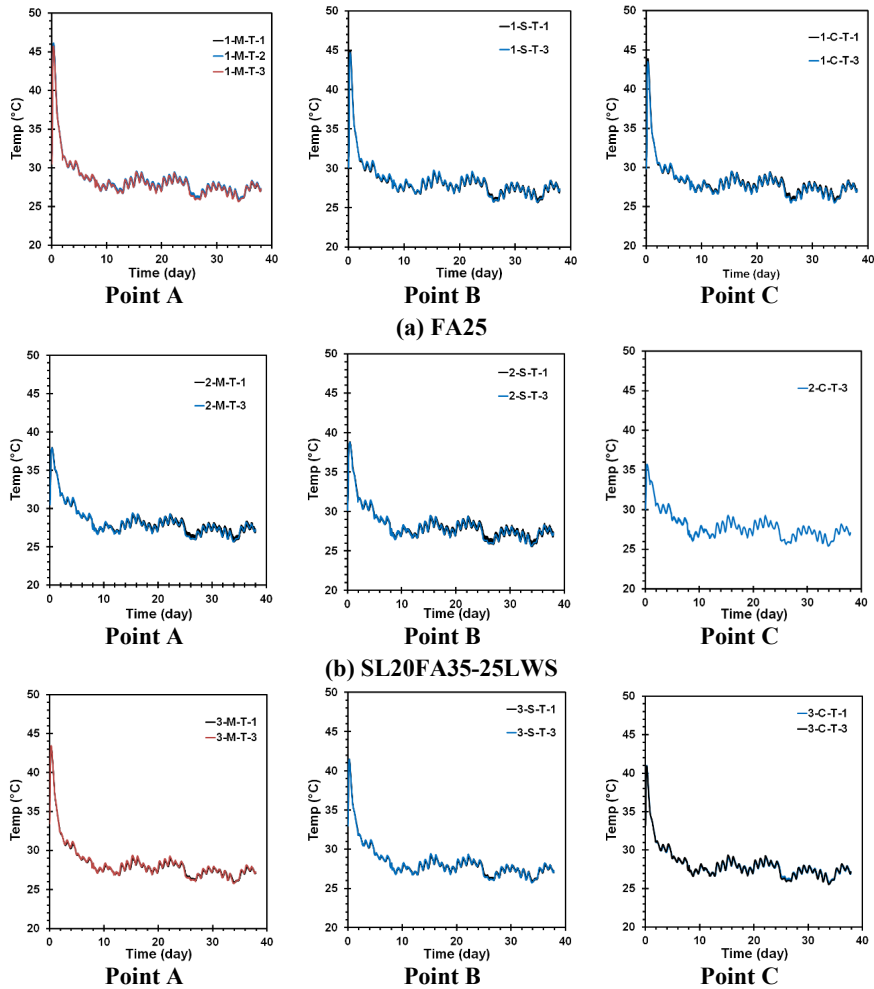


Figure C.9. Temperature variations along height of slabs at different stations. All slabs were moist cured for seven days before exposure to air drying

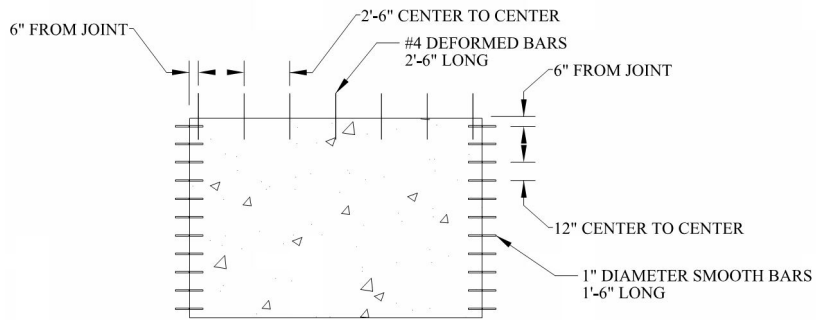


Figure C.10. Dowel bar placement in concrete pavement panels



Figure C.11. Excavation and preparation for concrete pavement



Figure C.12. Installation and compaction of aggregate base for concrete pavement

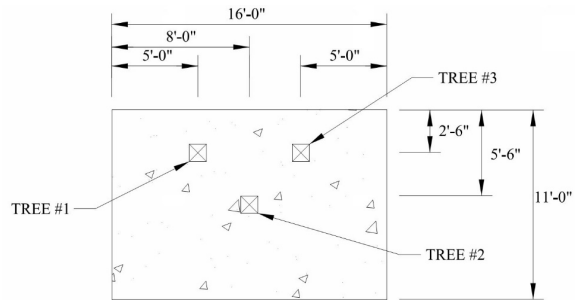


Figure C.13. Vibrating wire strain gauge placement within a pavement panel



Figure C.14. Vibrating wire strain gauge overall layout and close-up of tree No. 1



Figure C.15. Concrete placement and consolidation

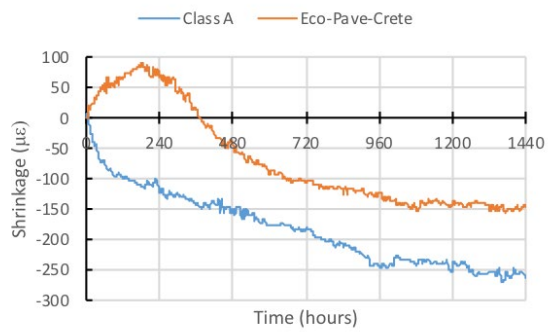


Figure C.16. Pavement panel shrinkage comparison of Class A and Eco-Pave-Crete Mixtures

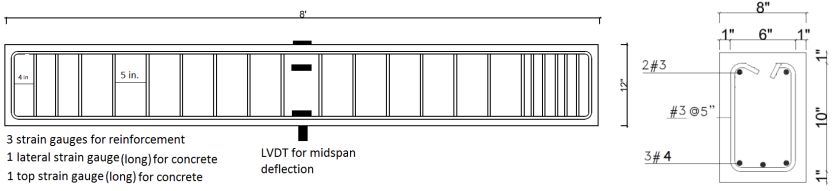


Figure C.17. Reinforcement layout and locations of strain gauges for test beams



Figure C.18. Beam flexural test setup

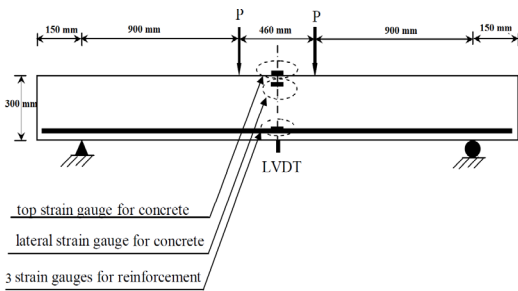


Figure C.19. Loading and strain-control systems

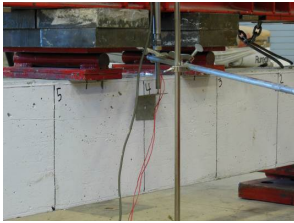


Figure C.20. Installation of LVDT (left) and strain gauges on surface of concrete beam (right)



Figure C.21. Concrete beam construction procedures

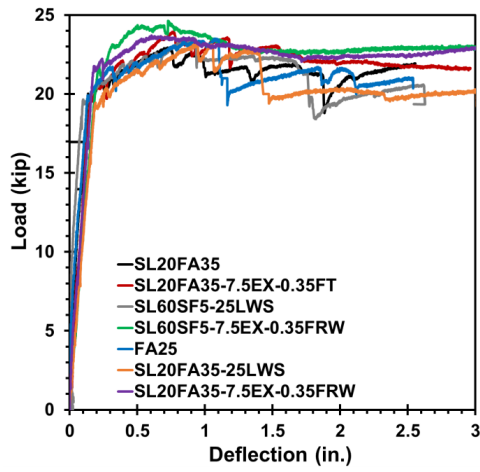


Figure C.22. Flexural load-deflection responses of tested beams

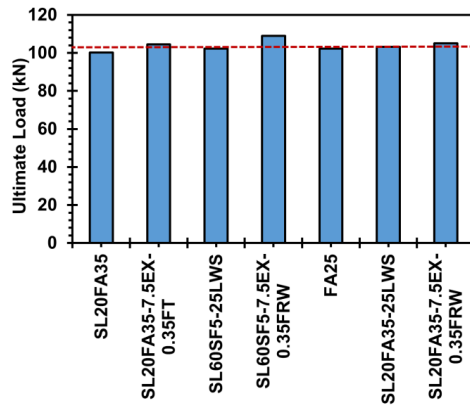


Figure C.23. Ultimate flexural load of tested beams

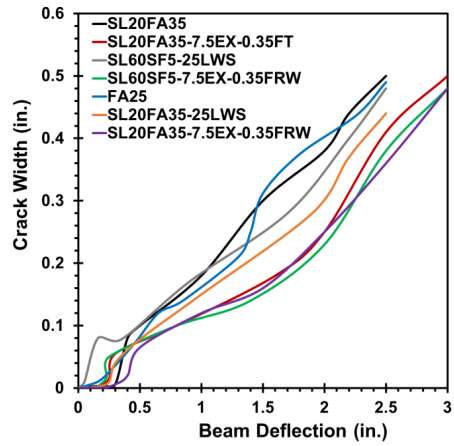


Figure C.24. Deflection-crack width relationship of tested beams

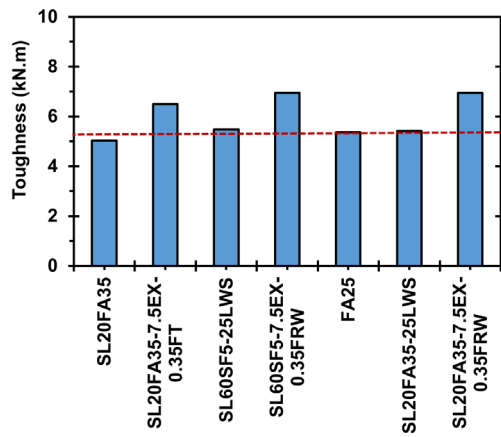


Figure C.25. Toughness of tested beams

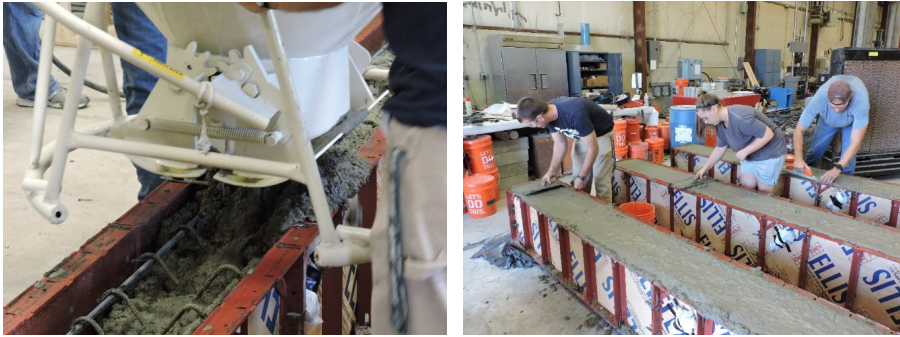


Figure C.26. Beam specimen concrete placement (l) and finishing (r)

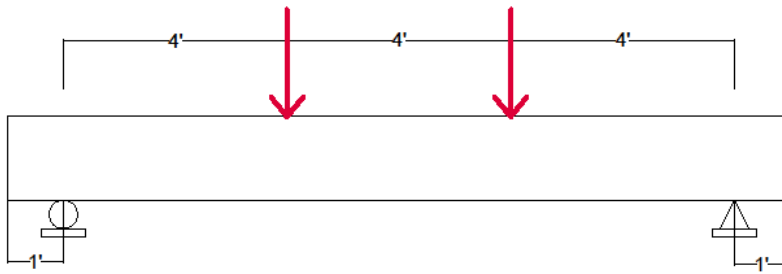


Figure C.27. Schematic of beam shear test setup



Figure C.28. Photograph of beam shear test setup

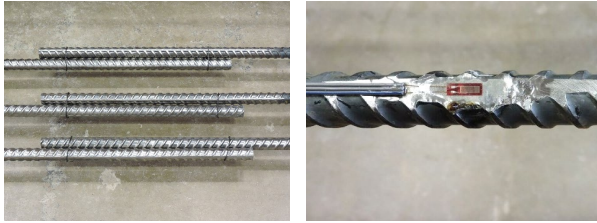


Figure C.29. Lap spliced reinforcing bars (l) and strain gauges adjacent to lap splice (r)

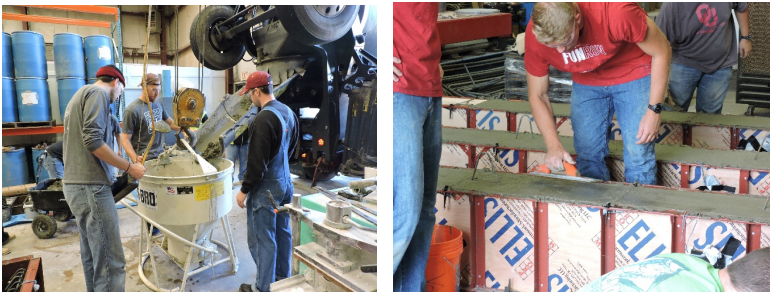


Figure C.30. Beam specimen concrete placement (l) and finishing (r)

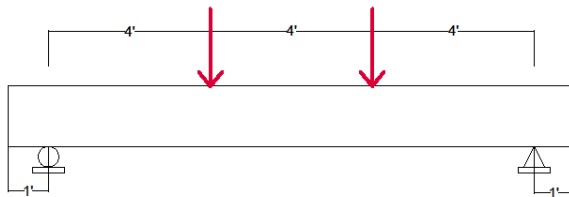


Figure C.31. Schematic of beam splice test setup



Figure C.32. Photograph of beam splice test setup

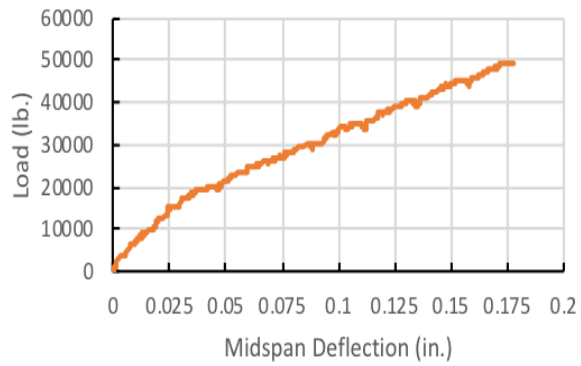


Figure C.33. Typical beam splice test specimen load-deflection response



Figure C.34. Typical beam splice test specimen failures